Dark-field Digital Holographic Microscopy for advanced semiconductor metrology

Christos Messinis

Cover: Artistic illustration of a popular culture theme presented after a 2D-Fourier Transform. This illustration resembles the ray tracing of the dark-field DHM from the object towards the microscope objective. The back cover shows a bright field image of an Overlay target, a μDBO-target that consists of four grating pairs. Concept and design by Ch. Messinis.
Printed by: ProefschriftMaken, Amsterdam, The Netherlands
ISBN: 978-94-6469-109-2
A digital version of this thesis is available at: https://research.vu.nl/

VRIJE UNIVERSITEIT

DARK-FIELD DIGITAL HOLOGRAPHIC MICROSCOPY FOR ADVANCED SEMICONDUCTOR METROLOGY

ACADEMISCH PROEFSCHRIFT

ter verkrijging van de graad Doctor of Philosophy aan
de Vrije Universiteit Amsterdam,
op gezag van de rector magnificus
prof.dr. J.J.G. Geurts,
in het openbaar te verdedigen
ten overstaan van de promotiecommissie
van de Faculteit der Bètawetenschappen
op dinsdag 29th november 2022 om 13.45 uur
in een bijeenkomst van de universiteit,
De Boelelaan 1105

door

Christos Messinis

geboren te Patras, Griekenland

promotor:	prof.dr. A.den Boef
copromotoren	prof.dr. J.F. de Boer
	dr. S. Witte
promotiecommissie:	dr. L. Amitonova dr.ir. S.M.B. Bäumer prof.dr. M. Kujawinska dr. G. Pedrini prof.dr. W.M.G. Ubachs prof.dr. H.P. Urbach

Dark-field Digital Holographic Microscopy for Advanced Semiconductor Metrology

DISSERTATION

To obtain
the degree of doctor of philosophy at the Vrije Universiteit,
on the authority of
the rector magnificus,
prof.dr. J.J.G. Geurts,
on account of the decision of the Doctorate Board,
to be publicly defended
on Tuesday the 29th of November 2022 at 13.45 hours

by

Christos Messinis

Born on the 26rd of March 1992
in Patras, Greece.

Graduation Committee:

Chair/secretary	prof.dr. W.M.G. Ubachs
Promotor	prof.dr. A.den Boef
Co-promotors	prof.dr. J.F. de Boer
	dr. S. Witte
Committee Members	dr. L. Amitonova
	dr.ir. S.M.B. Bäumer
	prof.dr. M. Kujawinska
	dr. G. Pedrini
	prof.dr. H.P. Urbach

The work described in this thesis was carried out at the Advanced Research Center for Nanolithography (ARCNL),a public-private partnership between the University of Amsterdam (UvA), Vrije Universiteit Amsterdam (VU Amsterdam), the Netherlands Organisation for Scientific Research (NWO), and the semiconductor equipment manufacturer ASML.

The work presented in chapter 3 was carried out at the LaserLab, Vrije Universiteit Amsterdam.

"And if you feel that you can't go on
And your will's sinkin' low
Just believe, and you can't go wrong
In the light you will find the road
Though the winds of change may blow around you
But that will always be so...
I will share your load."
Led Zeppelin, Physical Graffiti (Feb 24, 1975)

Contents

Chapter 1

Introduction

The goal of this thesis is to investigate the potential use of dark-field Digital Holographic Microscopy for advanced semiconductor overlay metrology. We will present first overlay metrology results using a novel off-axis dark-field digital holographic microscopy concept that acquires multiple holograms in parallel by angular frequency multiplexing. The presented results show potential for significant improvement and that digital holographic microscopy is a promising technique for future overlay metrology tools. Theoretical analysis and experimental investigations will be presented to validate this potential and quantify to which extent it can be considered the future overlay metrology tool. This chapter offers a brief introduction to semiconductor industry and the challenges of semiconductor metrology and clarifies the context of our research towards the use of holographic microscopy with an overview of holography and its application. The structure of the thesis is outlined at the end of this chapter.

1.1 Semiconductor Industry

In the era of the fourth industrial revolution, semiconductor industry has shown outstanding developments. Starting with a single transistor on a computer chip in the early 60s to fabricating billion transistors on a chip of roughly the size of a grain of sand [1]. This evolution has significantly impacted on our daily life, from electronic devices, such as computers and smartphones, to modern automobiles and medical equipment.

These rapid developments in the micro-electronics industry have been achieved by a continuous and aggressive reduction of the dimensions of semiconductor devices, a trend known as Moore's law [2]. Semiconductor devices like memory and logic CPU's are built 'layer-by-layer' in a sequence of repeating steps of lithography, etching, deposition etc. Smaller device features help to reduce power

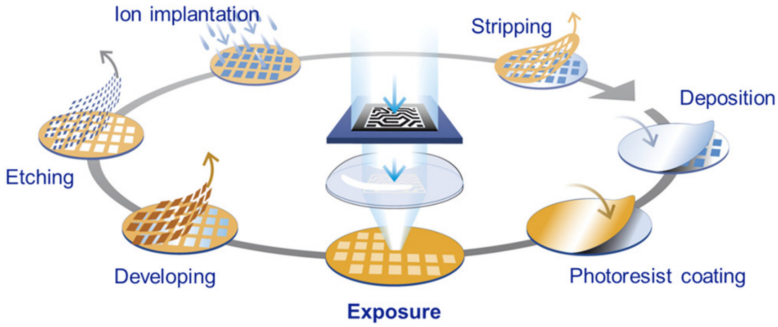

Figure 1.1: Simplified drawing of the repetitive fabrication process of a semiconductor device. The lithography step where the patterning of a new product layer start is marked with 'exposure'. The patterning of the device features takes place during optical lithography where a mask ('reticle') is imaged on a resist-coated wafer with a diameter of 300 mm. The field size of the image on the wafer is about 25×36 mm^2 and the lithography tool prints this field multiple times on the wafer in a step-and-scan fashion. After the lithography step the resist is developed and the wafer undergoes further processing steps like etching or ion implantation.

consumption, increase processing speed and allow more functionality in a smaller volume. Moreover, the high productivity of today's semiconductor industry helps to dramatically reduce the cost which makes semiconductor devices cost-effective for many applications. Figure 1.1 shows a simplified drawing of the various repetitive process steps that take place during semiconductor manufacturing [3].

A consequence of this progress is a rapidly increasing demand for chips that are being used in an increasing variety of applications. This has become particularly visible during the Covid-19 pandemic where the semiconductor industry has been struggling to keep up with the demand for chips. Almost every large industry is currently delaying their production because of that [4]. To deal with such an outbreak new technologies needs to be explored. Fabrication processes need to be faster and more efficient and every part of the current nano-lithography systems has to evolve to match the highly demanding requirements.

Manufacturing functioning chips with sufficient yield requires good control of the so called Critical Dimension (CD) of device features. Moreover, the patterns between different layers need to be properly connected and a good control of overlay (OV) between different layers is required. As a rule-of-thumb the maximum allowed CD variation is about 10 % of the nominal CD while the maximum allowed OV error is roughly 30 % of the nominal CD. Today, chips with a CD as small as several nanometers are being manufactured which requires CD and OV control that is roughly in the range of 0.5 and 1.5 nm respectively. However, in practice the required measurement precision must be better than 10 % of the maximum allowed process excursion. So today's CD metrology tools need < 0.1 nm precision and OV metrology tools need to be in the 0.1 - 0.2 nm regime [5].

These are challenging requirements since small process variations in the manufacturing environment can lead to CD and OV variations that exceed the tight

sub-nm control limits. As a result, various metrology techniques are used in production to measure these critical parameters. Metrology techniques can be applied during development, production and post-production. Scanning electron microscope (SEM) is one of the most versatile techniques used for in-line measurements followed by critical dimension small-angle X-ray scattering (CD-SAXS), where X-rays scattered from periodic nanostructures are analysed to non-destructively determine the pattern shape. In addition, Transmission electron microscopy (TEM) and 3D Atomic force microscopy (AFM) have traditionally been used for the needs of semiconductor industry. But for in-depth measurements of parameters like overlay non-destructive and penetrating techniques have to be used for determining any kind of displacement between subsequent patterned layers.

The work presented in this thesis will focus on potential improvements of optical overlay metrology so in the next section we will present a brief overview of the existing optical overlay metrology techniques that are being used today. Moreover, we will also discuss some of the (future) OV metrology challenges that these tools are facing.

1.1.1 Overlay Metrology

Overlay (also called registration error) refers to the lateral displacement of the lithographically exposed and developed pattern in one layer with respect to a previously created underlying structure in another layer. The measurement and control of the overlay between subsequent lithography steps is one of the critical steps in high volume semiconductor manufacturing. Currently the overlay accuracy in high-end manufacturing is of the order of 1-2 nm and the precision of overlay metrology is of the order of 0.1-0.2 nm [6].

We need to denote that there is a lot of confusion in the scientific community regarding these two terms and their meaning. Overlay accuracy is defined as how close a measurement is to its correct value. While overlay precision is defined as how close two or more measurements are to each other, regardless of whether those measurements are accurate or not. Both terms reflect on how close a measurement is to the true value, but they are not the same. And in fact, in an actual metrology tool what matters most is its precision for the obvious reason that if a fabrication process has a good overlay precision, in other words reproducible results per measurement, and the final product is yielding, the semiconductor manufactures will not complain about the overlay accuracy.

There are two kinds of optical overlay metrology in semiconductor industry. The most conventional image-based overlay (IBO) metrology and the diffraction-based overlay (DBO) metrology that is generally used on layers that have the most tight overlay control requirements. Many publications has shown that both the accuracy and total measurement uncertainty of DBO method are superior to the traditional IBO method, which made DBO the dominant way to measure OV. On the following subsections, an overview of the two techniques is presented for a better understanding of the importance of OV for the semiconductor industry.

1.1.2 Image-Based Overlay

As the name indicates the Image-Based-Overlay metrology (IBO) technique is an imaging method where a microscope is used to determine the pattern displacements based on the measured images. IBO uses specialized optical imaging tools and has traditionally been used in the industry, see Ref. [7, 8]. IBO has two basic measurement modes to perform OV metrology, Bright Field Microscopy (BFM) and Coherence Probe Microscopy (CPM) [9]. A schematic representation of the two modes is shown in Figure 1.2.

In Bright Field Microscopy, the tool uses the standard method of optical microscopy systems. The illumination in the Bright Field microscope is directed through a complex optical system and high precision optics are used to offer a high resolution imaging performance. Measurements are performed using white light while auto-focus is performed via the interferometer. OV is then measured on specially designed metrology marks.

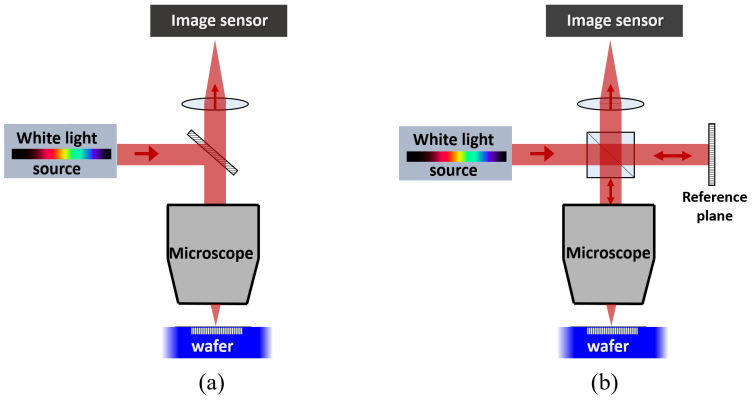

Figure 1.2: Schematic representation of two measuring modes of IBO. (a) a Bright field microscope where a collimated beam of a white light source is focused on the target which then is imaged on an image sensor.(b) a Coherence Probe Microscope based on a Linnin interferometer. A beam splitter and a reference mirror are added to allow measurements of the complex field.

The first metrology marks that were used in IBO metrology were the box-in-box (BiB) targets. A schematic drawing of such a BiB target is shown in Fig 1.3 (a). BiB targets consist of an inner-box (orange blocks) and an outer-box (blue blocks) in, respectively, the developed resist layer and a previously created lower layer [10]. The microscope creates an image of this BiB target and overlay is determined from this image by measuring the position of the inner box edges relative to the outer box edges.

Over time these BiB targets were replaced by gratings, that are called Advanced Imaging Metrology marks (AIM), since a grating image has more edges which improves overlay metrology precision. Figure 1.3. (d) presents an AIM mark where the inner and outer layers of the wafer are indicated with the blue and orange blocks respectively. AIM consists of inner and outer structures printed on

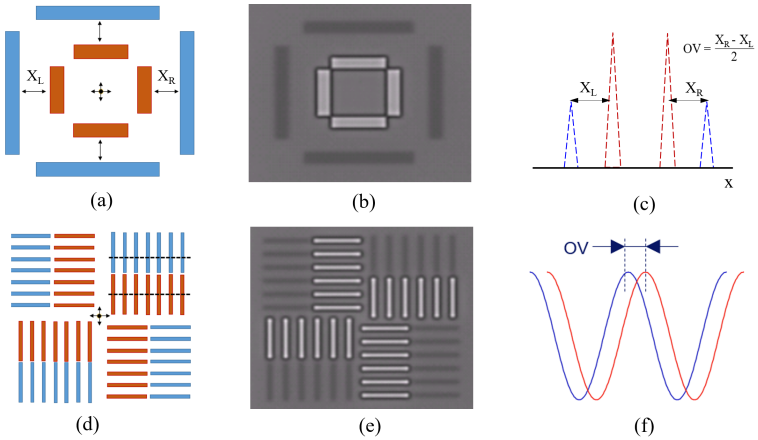

Figure 1.3: Intensity-based overlay marks. (a) Schematic drawing of a Box-in-box mark (BiB). Blue blocks indicate the bottom layer and orange blocks the top layer. (b) an actual BiB target and (c) how OV is determined. (d) Schematic drawing of an Advanced Imaging Metrology mark (AIM). (e) an actual AIM target and (f) how OV is determined. The optical images (b) and (c) were reproduced from [11].

two subsequent layers. Each of this structure is symmetric with respect to 90° rotation. This grating target is characterized by periodic series of lines and spaces. The center of inner and outer structures is found with kernel (black dotted lines) to check the grating profile. The overlay is then determined as the vector between the two centers. The algorithm checks the location of the symmetry point of pattern associated with current layer and repeats the process for a layer that is used as a reference. The difference of the two locations is the overlay error.

Coherence Probe Microscopy is an extension to regular microscopy, and was introduced as a method that enables 3-D measurement of pattern dimensions. CPM is based on a Linnik interferometer and measures both the amplitude and phase of an image. For more information about Linnik interferometer theory, see [12]. The output signal corresponds to the signal of coherent region, by making a focus scan; the tool gives a 'cross-section' image of the target, and then OV is deduced from this image. CPM is mainly used when process variations creates an effect that is visible to the BFM, but does not affect the target topography.

In IBO, lens aberrations and illumination imperfections introduce an offset called tool induced shift (TIS) that can be corrected by measuring the OV for 0° and 180° wafer orientation [13]. Unfortunately, TIS in IBO is sensitive to wafer processing variations. For example, film thickness variations will change the spectral shape and angular distribution of the light that is diffracted by the gratings which results in varying TIS errors. This variation can only be minimized by illuminating the target at a well-defined wavelength and a well-defined illumination angle which goes at the expense of signal level (resulting in long measurement times).

IBO techniques had already reached the maximum potential of their perfor-

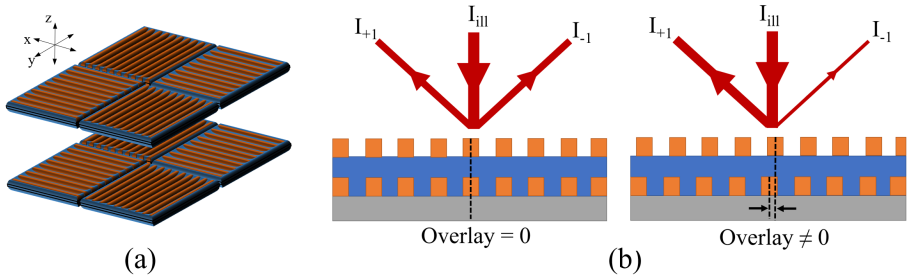

Figure 1.4: Diffraction-based overlay mark. (a) Top-view of the X and Y gratings of DBO mark (b) Stacked gratings alignments and how it corresponds to symmetric and asymmetric scattering of the diffracted light.

mance capability for OV metrology with many challenges that are impossible to overcome and keep up with the industrial requirements in terms of OV metrology precision and accuracy. This is the reason why semiconductor industry is focused on scatterometry based analysis to measure overlay with the so called Diffraction-based OVerlay that will be addressed in the following paragraph.

1.1.3 Diffraction-Based Overlay

In order to deal with the highly demanding overlay requirements of today's semiconductor devices, Diffraction-Based Overlay metrology (DBO) [9, 14, 15] was successfully introduced several years ago as an improved method to measure OV. For scatterometry-based 3D overlay, displacement between the layers is determined from intensity variations among the diffracted orders from stacked gratings (named DBO marks). A DBO mark consists of small overlapping gratings in the resist layer and an underlying layer. The periodicity of the grating lines or the grating pitches range from 400 to 1600 nm and the size of the DBO marks ranges from 58 × 58 to 5 × 5 µm^2.

If the gratings are perfectly aligned (=zero overlay error) they form a symmetric composite grating with symmetric scattering properties. However, a small misalignment (OV error ≠ 0) creates an asymmetric composite grating which changes the intensities of the +1st diffraction order (I_{+1}) and the -1st diffraction order (I_{-1}) as schematically shown in Figure 1.4.

The superiority of DBO with respect to IBO is in the fact that the OV information is encoded in an intensity difference instead of the location of edges in an image. This makes the measurement in DBO less sensitive to aberrations in the optics between the target and the detector. Moreover, in DBO the individual grating lines no longer need to be resolved which allows the use of smaller grating pitches which further improve metrology precision.

1.1.4 Signal formation in µDBO

In order to explain the signal formation in DBO we use a simple plane-wave propagation model. A schematic drawing of the signal formation is shown in Fig. 1.5 where the properties of the wafer can potentially affect the signal processing.

With the assumption of a plane wave propagation, the intensities I_{+1} and I_{-1} are given by:

$$I_{+1} = |Ae^{j\alpha} + Be^{j\beta}|^2 = A^2 + B^2 + 2ABcos(\beta - \alpha), \tag{1.1}$$

$$I_{-1} = |Ae^{-j\alpha} + Be^{j\beta}|^2 = A^2 + B^2 + 2ABcos(\beta + \alpha), \tag{1.2}$$

where A, B are the amplitudes of the waves diffracted for the top and bottom grating respectively.

Here α is a phase term introduced by a spatial translation of the top layer that is proportional to OV :

$$\alpha = 2\pi \frac{OV}{P}, \tag{1.3}$$

with P the grating pitch. β is a phase term for the bottom grating that depends on the thickness of the wafer :

$$\beta = 4\pi \frac{T}{\lambda}, \tag{1.4}$$

the bottom grating carries the phase depending on the extra distance traveled due to the height difference T.

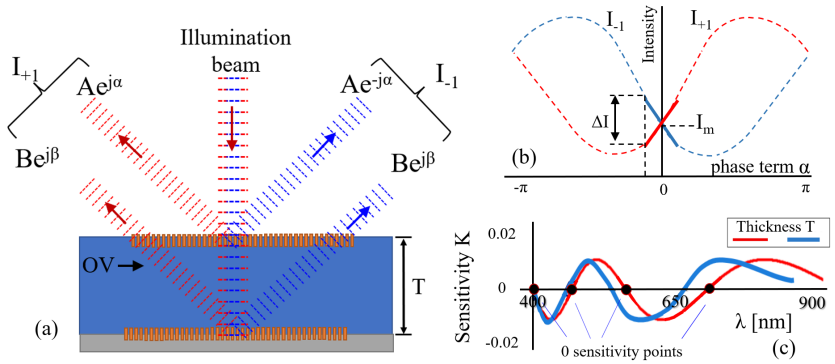

Figure 1.5: (a) Schematic of a plane wave hitting a top and bottom grating, with the first diffraction orders of both gratings. (b) Intensity versus phase term α. The expected swing curve which around the origin reveals a linear dependency between OV and ΔI (solid red and blue lines). (c) Sensitivity K for two wafers with different thicknesses T. Color indicates different T for a measured ΔI.

Normally, the OV is very small compared to the grating pitch, P so the angle α is close to 0 and we can use the approximation $sin(\alpha) = \alpha$ and $cos(\alpha) = 1$. Under those conditions the detected intensities are given by:

$$I_{+1} = A^2 + B^2 + 2ABcos(\beta) + 4\pi\frac{AB}{P}sin(\beta)OV \tag{1.5}$$

$$I_{-1} = A^2 + B^2 + 2ABcos(\beta) - 4\pi\frac{AB}{P}sin(\beta)OV \tag{1.6}$$

The intensity asymmetry between the two diffraction orders, $\Delta I = I_1 - I_{-1}$ is then:

$$\begin{aligned}\Delta I &= 4AB \times sin(\beta)sin(\alpha) \\ &\approx 8\pi\frac{AB}{P}sin\left(4\pi\frac{T}{\lambda}\right)OV.\end{aligned} \tag{1.7}$$

For the sake of simplicity we have excluded phenomena like bouncing waves between top and bottom layers or asymmetric grating lines. However, despite this rather extreme simplification it still serves as a useful expression that takes into account all the essentials in order to obtain overlay information from a grating. Equation (1.7) is the core of the DBO Model. However, on the OV measurements that we will present in Chapter 2, the expected OV errors are many times smaller than the grating pitch and we will approximate this equation with the following simplified expression:

$$\Delta I \equiv \frac{I_{+1} - I_{-1}}{I_{+1} + I_{-1}} \approx K(\lambda) \times OV, \tag{1.8}$$

for convenience, we have normalized the intensity difference to the total intensity. Here $K(\lambda)$ is a stack sensitivity parameter that depends on the geometry of the grating and the material properties of the thin film stack in which the gratings are embedded. This parameter is an unknown scale factor that can become as small as 10^{-2} nm^{-1} which results in the need for an accurate and robust measurement of the $+1^{st}$ and -1^{st} order intensities. K is essentially unknown since it depends on the grating properties and the optical properties of the materials between the top grating and bottom grating. In practice these properties are not known, making it impossible to accurately calculate the OV error without eliminating this factor.

Equations (1.7) and (1.8) show that the unknown overlay sensitivity K also depends strongly on wavelength. [16]. This behaviour is shown in Fig. 1.5(c). To obtain a robust measurement of overlay, attention should be paid to the measurement settings such as the selected wavelength for known thickness of the wafer. As shown in Fig. 1.5(c) a careful selection of wavelengths can eliminate the sensitivity factor. However, the results of [16] have shown that near-zero stack sensitivity corresponds to unstable overlay measurement conditions on the swing-curve and such regions must be avoided.

In Chapter 2, we will show that this term can be eliminated by measuring the intensity difference on two pairs of overlapping gratings where a small known shift ("bias") is added to the unknown OV error. This "bias" is a designed shift within the linear region of the swing curve. Then the intensity differences can be measured using, for example, a scatterometer [17] or a dark-field microscope

[18]. However, differential intensity noise between these two off-axis illumination beams must be low since overlay is encoded in an intensity difference between a $+1^{st}$ order and a -1^{st} order.

1.1.5 Challenges in Optical Overlay Metrology

Continuous improvements in optical overlay metrology are needed to keep up with shrinking device dimensions in modern chips. This generates new challenges that optical metrology faces which lead to demanding metrology sensor requirements. Most of these challenges are related to the dimensions or the materials that are used on today's wafers and how they are associated with the performance of metrology tools.

Starting with the size of the metrology targets, since the semiconductor industry is advancing to smaller and smaller dimensions in modern chips, it is essential to reduce the size of the metrology targets. This has a lot of benefits but also comes at a price. Smaller metrology targets have the advantage to be placed in-die (enabling intra-field corrections) instead of only in the scribe lanes of a wafer, allowing more freedom and flexibility in metrology target placement [19]. Multiple targets of different designs nearby ensures accurate overlay measurements during film stack changes, as it gives the freedom to choose an overlay target that matches the optical properties of the film stack. And finally smaller targets enable a throughput gain when more than one overlay targets are measured in a single acquisition, which might be beneficial for edge placement error control.

On the dark side of this development, smaller target size can affect the overlay error performance since the periodic gratings of an Overlay target cannot be considered as pure infinite gratings anymore [20]. When the size of an individual target becomes smaller than 5×5 µm^2 and the grating pitch is on a range of a few hundred nanometers, finite grating effects will emerge due to edge effects. For instance, the currently smaller OV mark (the C4) has a 2.2×1.5 µm^2 size and consists of only four grating lines. A consequence of diffraction of a smaller area is a decrease in the diffraction efficiency (fewer diffracted photons are captured by the optics). Later on we will show that this is also related to the thickness of the resist layer which also becomes thinner and thinner over time. Finally, the small targets introduce optical leakage and proximity effects from the surrounding structures and could degrade the accuracy of the measurement.

Figure 1.6.(a) summarizes the OV target size challenge. DBO marks with sizes that ranges from 8×8 down to 2.2×1.5 µm^2 were imaged with a dark-field microscope. All dark-field images were taken with the same camera integration time and have been rescaled with respect to the target size depicting. That explains why the smaller targets are more blurred. As shown, for smaller target size, there is a reduction of the diffraction efficiency with a 17 % reduction from C16 to C4. At the same time, the target-to-target standard variation (3 σ variance) for the 3 targets (within the drawn lines) shows that the reduction of the dimensions introduces light leakage from grating to grating that translates to OV errors. This data were reproduced from [19].

As it was already aforementioned another challenge that optical OV metrology

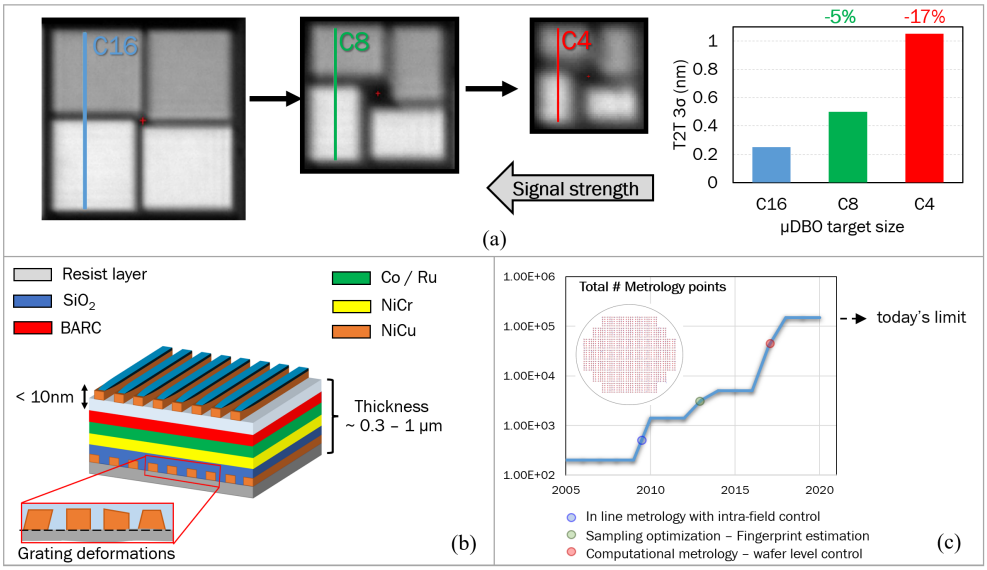

Figure 1.6: (a) Dark-field images of Diffraction-based overlay marks. The sizes of these OV marks are the following, C16 is 8 × 8 µm^2, C8 is 4 × 4 µm^2, and C4 is 2.2 × 1.5 µm^2. Signal stength is normalized to the larger target size. The estimated target-to-target standard variation (3 σ variance) for the 3 targets (within the drawn lines). This data was reproduced from [19]. (b) The film stack for a variety of materials. A close up of the bottom gratings reveals potential grating deformations that could occur during production. (c) A plot of the rapid increase in the total number of metrology points per wafer within the last 15 years [21]. A schematic drawing of the wafer with red dots that represent the metrology points is included.

encounters is the properties of the film stack. Fig. 1.6.(b) shows the complexity of the film stack and the consistency of multiple layers with different properties. The thickness of the wafers depends on the product and application and can potentially affect the measurement and nowadays varies from 0.3 up to 1 µm. A large variety of materials is regularly used in semiconductor device manufacturing, resulting in a strong wavelength dependency of the signal strength. For instance, the bottom grating in DBO is often covered by absorbing layers, like amorphous silicon, which are highly absorbing in the visible wavelength range and correspond to a decrease of the diffraction efficiency. Furthermore, the top grating is formed in a thin resist layer that tends to become thinner and thinner over the years. Currently thin resists are less than 10 nm thick and the diffraction efficiencies are less than 0.01 %, requiring long acquisition times and delays the metrology process.

Moreover, wafer-processing steps like etching (step 5 of Figure 1.1) can lead to an asymmetric deformation of a grating profile as well as grating imbalances which results in a wavelength-dependent measured overlay. This is schematically

shown on the close-up of the bottom grating lines in Fig. 1.6.(b). In order to adequately deal with this a DBO tool often measures at multiple wavelengths over a large wavelength range [22]. This also results in low diffraction efficiencies.

Finally, DBO measurements need to be performed on many points on a wafer for many wafers at high throughput to ensure the stability and robustness that is required. Fig. 1.6.(c) shows a plot of the rapid increase in the total number of metrology points per wafer within the last 15 years [21]. The introduction of µDBO targets allowed intra-field control (blue point in the plot), followed by additional sampling optimization with fingerprint estimation (green point). But the turning point was the inclusion of computational metrology that allowed a rapid increase of the number of metrology points above 10^5 measurements per wafer. Since the metrology marks become smaller and smaller the total number of metrology points also needs to keep up with this reduction. In practice this means that acquisition times for a DBO image must be in the order of a few milliseconds or parallel sensing needs to be enabled with the use of more compact metrology tools.

In the end it is clear that a combination of weak signals, small acquisition times and sub-nm precision requirements drives the need for high-brightness light sources. These are a few of the main challenges of optical metrology and in this thesis we will show that Digital holographic microscopy (DHM) can potentially address and solve these challenges with a cost-effective solution. Before diving into the details on how we propose to use DHM for advanced OVerlay metrology, from Chapter 2 and onwards, we start by briefly describing the method in section 1.2.

1.2 Digital Holographic Microscopy

Digital Holographic Microscopy (DHM) is a well established method that has already been described in detail in several books and review papers [23–29]. Here we just give a short overview of the developments of DHM, from the discovery of holography to the present day. Then we will present the general concepts of holography, recording and reconstructing a hologram with the scalar wave theory and the Fourier analysis.

1.2.1 Introduction to Holography

Holography dates from 1947, when Hungarian electrical engineer and physicist Dennis Gabor developed the theory of holography while working on resolution improvements in electron microscopy [30, 31]. The given name comes from the Greek word holos; whole, and graphe; writing, indicating that holography can reveal the entire message. The type of holography originally proposed by Gabor, utilizes an inline setup. This setup was an inline recording technique in which weakly scattered light from a transmissive object was made to interfere with the strong reference wave. The interference pattern contains both the amplitude and phase of the object. He was awarded the Nobel prize in physics in 1971 for this

invention. However, widespread application of this technique was impractical until the invention of the laser in 1960.

The reconstructed image from the in-line holography was noisy due to the presence of the twin image of the object. The twin-image was and still is a classical problem in holographic imaging and several methods were proposed to eliminate or suppress it in the reconstruction. In 1951, Bragg and Rogers developed a solution to subtract the twin image by recording a conjugated second hologram of the object at twice the distance from the first [32]. Ever since, various techniques have been developed regarding twin-image reduction in holography and a review is given by Hennelly *et al.* [33].

A breakthrough in holography came in the form of the off-axis holographic recording proposed by Leith and Upatnieks [34], and Lohmann [35] in 1960s. The off-axis holography led to the complete separation of the twin image and the object image in the reconstructions which later on led to developments in the field of color display holography through the works of Leith and Upatnieks [36], Mandel [37] and Pennington and Lin [38]. The development of powerful digital computers and high resolution printing led to the field of computer generated holograms and digital recording of holograms. Goodman and Lawrence [39], and Yaroslavskii and Merzlyakov [40] were among the first to propose the idea of recording and reconstructing holograms digitally.

With the development of high resolution CCD (charge coupled device) technology, and the subsequent cost reduction digital holography was further developed by Schnars and Juptner [41]. Today holography has become a wide-spread discipline of modern optics and finds many practical applications like holographic data storage [42, 43], non-destructive testing of materials [44, 45], 3D shape measurement and display [46–48], and phase contrast microscopy [49, 50] to name a few.

Significant developments in image enhancement had also emerged from DHM. Works with deep UV (193 nm) [51] DHM, x-ray imaging of crystallographic structure [52], electron microscopy [53] and gamma ray holography [54] had all been demonstrated to offer an increased resolution potential. At the same time, DHM is able to correct for image imperfections introduced by the lens by calibrating wavefront aberrations [50, 55–61].

This thesis focuses on microscopy applications of digital holography for semiconductor metrology, and therefore it is important to acknowledge some of them. Metrology of deformations and vibrations is a major topic of DHM [62–66]. For instance, Schulze *et al.* demonstrated the use of DHM for defect detection on semiconductor wafers, and compared their results with other wafer inspection technologies. In addition, the phase information allowed the visualization of the topology of defects of a wafer, with images comparable to scanning electron microscope (SEM) images. These developments created the idea of applying DHM for measuring OV based on DBO configurations. With the knowledge of the complex field combined with prior work on defect detection on semiconductor wafers we started our investigation aiming to develop a technology that can be used for advanced OV metrology.

After this brief outline of the origins and the applications of holography, it is

important to explain the basic principles of this technique and derive expressions that can offer a stepping stone towards the results that will be presented in the following chapters of the thesis.

1.2.2 Basic Principles of Holography

In holography, coherent interference of a reference and an object wave is recorded as an interference pattern. In Figure 1.7(a) we represent this interference of the two beams in an off-axis configuration for a monochromatic wave. For many practical applications of interest a scalar wave approximation is sufficient for describing the principle of holography. Let A, B, ϕ_o, and ϕ_r, be the amplitudes and phases of the object and the reference wavefronts, respectively. For simplicity, the reference beam is considered as a plane wave but in principle, any nonuniform wave may be used for recording the hologram. The complex amplitude of reference and object waves are given by:

$$E_o(x,y,z) = |E_o|\, e^{i\omega t} e^{-i\phi_o(x,y,z)}, \tag{1.9}$$

$$E_R(x,y,z) = |E_R|\, e^{i\omega t} e^{-i\phi_R(x,y,z)}, \tag{1.10}$$

In these equations, $e^{j\omega t}$ is a time-varying function where ω is the angular frequency and is equal to $\omega = \frac{f}{2\pi}$, with f the frequency. The angular frequency ω, the frequency f and the wavelength λ are related to the speed of light c as $c = \lambda f$.

For a monochromatic wave in the visible wavelength range the optical frequency f ranges from 3.8×10^{14} to 7.7×10^{14} Hz. These frequency variations of the electric field cannot be measured by any of the currently available light sensors. Only the intensity of light is detected and since in most applications, the spatial distribution of the electric field is of interest we can neglect the time varying part of eq. (1.9 and 1.10) and consider only the spatial part of the complex wave. The coherent addition of the object wave E_o and the reference wave E_R yields the following intensity distribution in the detection plane:

$$\begin{aligned} I(x,y,z) &= (E_o(x,y,z) + E_R(x,y,z))(E_o^*(x,y,z) + E_R^*(x,y,z)) \\ &= E_o E_o^* + E_R E_R^* + E_o E_R^* + E_R E_o^* \end{aligned} \tag{1.11}$$

where $*$ denotes a complex conjugation. This notation is further simplified by omitting the (x, y, z). $E_o E_o^* = |E_o|^2$ and $E_R E_R^* = |E_R|^2$ are the auto-correlation terms of the object and the reference wavefront and since they contain no phase terms, they are the DC components of the recorded intensity. On the other hand, the remaining terms are complex terms that include both amplitude and phase information for the two wavefronts. These terms are usually called cross-correlation terms for this reason. This interference can be written as

$$\begin{aligned} E_R^* E_o + E_o^* E_R &= |E_o|\,|E_R|\,[e^{-i\phi_R} e^{+i\phi_o} + e^{+i\phi_R} e^{-i\phi_o}] \\ &= 2\,|E_o|\,|E_R|\cos(\phi_R - \phi_o). \end{aligned} \tag{1.12}$$

It can be seen that the sum of the two cross-correlation terms depends on their relative phase. For this analysis we see that eq. (1.12) is the intensity of the recorded hologram with the complex field information hidden in the two of the four terms. By illuminating this hologram with a copy of the reference wave E_R, we get the transmitted field:

$$E_R I = E_R \left|E_o\right|^2 + E_R \left|E_R\right|^2 + E_R E_o E_R^* + E_R E_R E_o^*. \tag{1.13}$$

The first term $E_R \left|E_o\right|^2$ represents the complex field of the reference wave modulated by the intensity of the object wave $\left|E_o\right|^2$ (its intensity) and the second term represents the same complex field but now modulated by the intensity of the reference wave, $\left|E_R\right|^2$. With the same reasoning, now the third term $E_o \left|E_R\right|^2$, and forth term $E_o \left|E_R\right|^2$ represent the complex field of the object field and its conjugate multiplied by the reference field's intensity respectively.

We are interested in the reconstruction of the third term which has exactly the same properties as the original object wave. An observer perceives it as coming from a virtual image of the object located exactly at the original object location (Figure 1.7.(b)). In the in-line configuration proposed by Gabor [30], the four reconstructions of Figure 1.7.(b) are superimposed. The presented derivations explain the twin-image challenge of in-line holography that was mentioned in section 1.2.1, and helps to illustrate the off-axis configuration where the angle θ between reference and object wave allows an easy spatial separation of the wavefronts as depicted in the angular spectrum image.

1.2.3 General description of DHM

Standard digital holographic microscopy (DHM) setups consist of an illumination source, an interferometer, a detector, and a computer. For the illumination, a laser source with sufficient coherence is commonly used to produce interference between the two beams. For multi-wavelength techniques, a tunable laser or a mix of different lasers can be coupled into the interferometer. There are also low-coherence techniques for the purpose of reducing speckle and spurious interference noise (more on this in Ch. 6).

Two main types of interferometers are the Michelson interferometer for reflective objects and the Mach-Zehnder interferometer for transmissive objects. A schematic drawing for each configuration is shown in Fig. 1.8. In each diagram, the light green beam is the input from the laser, the light blue is the reference beam path, and the light red is the object beam paths. In both designs, the paths of the reference and object beam are matched in order to generate a fringe pattern. The object is illuminated with a plane wave using a 4F system. The reference arrives at the image plane with the same wavefront curvature as the object wave, with the use of the same optics. An offset in the angle of incidence of the reference beam is generated by rotating the M2 mirror for the off-axis configuration. The Mach-Zehnder types require more components but offer more flexibility in alignment, especially when microscopic imaging optics are used.

Nowadays, CCD, or CMOS cameras are used to capture and digitize a holo-

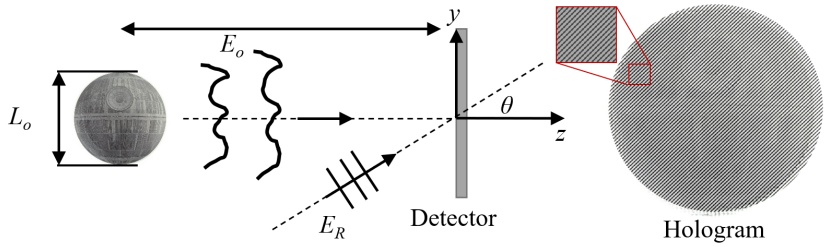

(a) Recording of a hologram

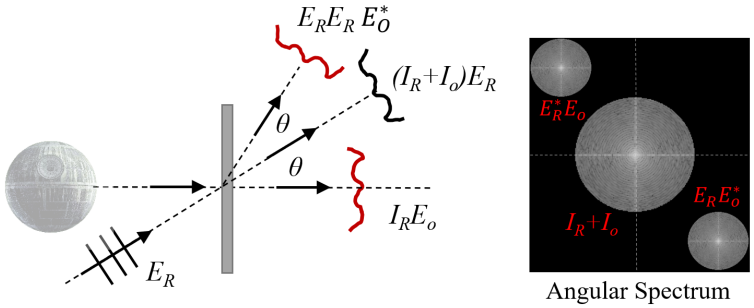

(b) Reconstruction of a hologram

Figure 1.7: (a) Schematic of the recording of a hologram. (b) Schematic of the reconstruction of the virtual image of the object. The angular spectrum represents the Fourier analysis of the hologram (details on Appendix 1.A.).

graphic interference pattern. The pixel size of these devices is several microns with thousands of pixel counts. 100+ megapixel cameras are readily available today, capable of recording hologram samples in more than a 10,000 by 10,000 array, an amazing improvement over the 256 by 256 vidicon-generated array. At the same time, Moore's law has improved the speed of computers allowing the processing of multiple holograms within a few minutes and at very low cost.

It is important to denote that while some display applications of holography are most effective when the hologram is recorded on photographic plates or photopolymers, the developments described above have led to the almost complete replacement of films by electronic detectors when holography is used in microscopy or other applications in which the hologram can be recorded in a small but high-resolution format. Once the hologram exists in electronic form, it is natural to reconstruct images digitally [28].

The holographic reconstruction process is quite straightforwards using either of the configurations depicted in Fig. 1.8. Fig. 1.8. (c) outlines the steps for the reconstruction of a reflective 1951 USAF Test Target. The measured hologram is digitized by the camera and input to the computer as a 2-D array of integers with 8-bit, 12-bit or 16-bit gray-scale resolution. Based on the principles described in 1.2.2, a 2D-Fourier Transform is applied to the complex 2-D array in order to

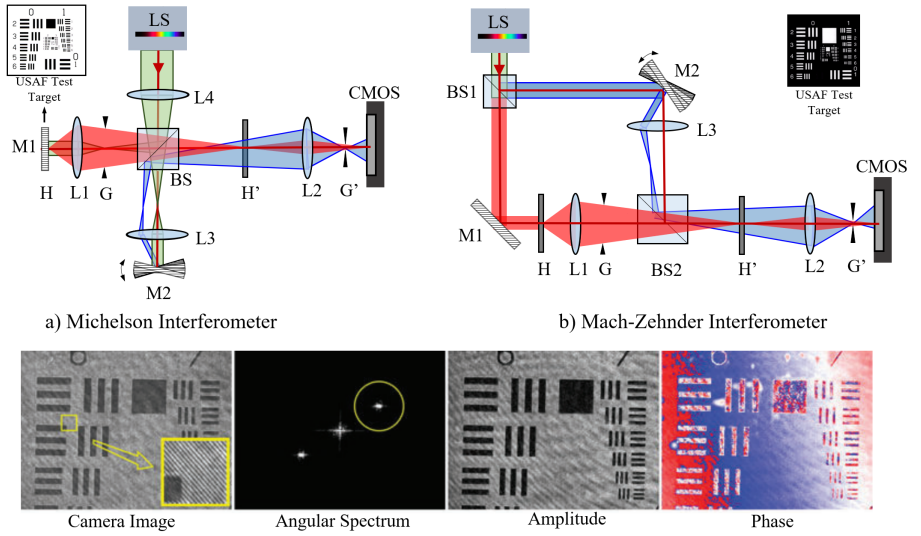

Figure 1.8: (a) Michelson interferometer for DHM of reflective sample. (b) Mach-Zehnder interferometer for DHM of transmissive sample. LS: Light source; BS: beam-splitters; L: lenses; H: Sample Position; G,G': Apertures; H': Fourier plane ; M: mirrors. (c) Off-axis DHM process. This data was reproduced from [26].

obtain the angular spectrum. From the angular spectrum the sideband that corresponds to the third term of eq. 1.13 (yellow circled area) is computationally filtered and shifted to the origin. An inverse Fourier transform is then performed to obtain the complex field of the object beam.

1.A Fourier analysis of the hologram

A Fourier transform (FT) is a mathematical transform that decomposes functions depending on space $\vec{r}$ or time t into functions depending on spatial frequency $\vec{k_r}$ or temporal frequency f. The Fourier transform is one of the most frequently used mathematical tools to describe optics phenomena such as wavefront propagation, filtering, image formation, and holographic reconstructions [23, 67].

For the Fourier analysis that we use for the holographic reconstructions of this thesis it is important to denote the fundamental mathematical expression that are regularly used. The Fourier transform of a 2D function $f(x, y)$ and the inverse Fourier transform of this function from the spatial frequency domain back to space domain $F(k_x, k_y)$ are

$$F(k_x, k_y) = \int_{-\infty}^{\infty}\int_{-\infty}^{\infty} f(x, y)\exp[i2\pi(xk_x + yk_y)]dxdy, \tag{1.14}$$

$$f(x, y) = \int_{-\infty}^{\infty}\int_{-\infty}^{\infty} F(k_x, k_y)f(x, y)\exp[-i2\pi(xk_x + yk_y)]dk_xdk_y. \tag{1.15}$$

In the following analysis we will use the notations $F(k_x, k_y) = \mathcal{F}\{f(x, y)\}$ and $f(x, y) = i\mathcal{F}\{F(k_x, k_y)\}$, where $\mathcal{F}$ and $i\mathcal{F}$ are the Fourier transform and its inverse transform, respectively. And an important mathematical tool that we will need for our analysis is also the convolution between two function $f(x, y)$ and $g(x, y)$ given by:

$$h(x^{'}, y^{'}) = f \otimes g = \int_{-\infty}^{\infty}\int_{-\infty}^{\infty} f(x, y)g(x^{'} - x, y^{'} - y)dxdy, \tag{1.16}$$

with $\otimes$ the symbol that denotes the convolution. The convolution theorem states that a multiplication in the spatial domain equals a convolution in the spatial frequency domain [23]. The Fourier transform of the holographically reconstructed wavefront is equal to the sum of the $\mathcal{F}$ of four individual terms of eq. (1.13):

$$\mathcal{F}\{E_R I\} = \mathcal{F}\{E_R \left|E_o\right|^2\} + \mathcal{F}\{E_R \left|E_R\right|^2\} + \mathcal{F}\{E_R E_o E_R^*\}\mathcal{F}\{E_R E_R E_o^*\}. \tag{1.17}$$

We consider a plane reference wave having constant amplitude B propagating in the direction (0, sin θ, cos θ):

$$E_R(x, y, z) = \left|E_R\right| e^{2\pi i(y \sin\theta + z\cos\theta)/\lambda}. \tag{1.18}$$

If we omit the z direction we end up with the angular spectrum that was represented in Fig. 1.7.(b). Since the reference is a plane wave, the Fourier transform of $E_R \left|E_R\right|^2$, (the second term of eq. (1.18)), is a delta function $\delta(k_x, k_y - k_r)$ centered at $k_x = 0$, $k_y = k_r$. Here k_x and k_y are the spatial frequencies and $k_r = \sin\theta/\lambda$, is considered a single point within the frequency domain. Applying

the convolution theorem for the first term of eq. (1.18) we obtain the following:

$$\mathcal{F}\{E_R E_o^* E_o\} = \tilde{E_R}(k_x, k_y) \otimes \tilde{E_o^*}(k_x, k_y) \otimes \tilde{E_o}(k_x, k_y). \tag{1.19}$$

If the object wave has frequency components lower than R, then the convolution term expressed by eq. (1.21) has an extension equal to $2R$ ending up at the center of the angular spectrum, like the second term. The third and the fourth terms in equation (1.18) are given by

$$\begin{aligned}\mathcal{F}\{E_R E_R^* E_o\} &= \tilde{E_R}((k_x, k_y) \otimes \tilde{E_R^*}(k_x, k_y) \otimes \tilde{E_o}((k_x, k_y) \\ &= \tilde{E_o}((k_x, k_y),\end{aligned} \tag{1.20}$$

$$\begin{aligned}\mathcal{F}\{E_R E_R E_o^*\} &= \tilde{E_R}((k_x, k_y) \otimes \tilde{E_R}((k_x, k_y) \otimes \tilde{E_o^*}((k_x, k_y) \\ &= \delta((k_x, k_y - 2k_x) \otimes \tilde{E_o^*}((k_x, k_y).\end{aligned} \tag{1.21}$$

For the complete separation of these two terms from the base-band (center of spatial frequency domain), $k_r \geq 3R$. At the same time the maximum angle in the off-axis configuration, θ_{max}, determines the maximum spatial frequency, k_{max}, in the hologram:

$$k_{max} = \frac{2}{\lambda} \sin \frac{\theta_{max}}{2}. \tag{1.22}$$

Eq. (1.23) sets the Nyquist sampling criterion, which is an upper limit on the maximum angle-of-incidence of the reference beam. This is a limiting factor of the resolution of the detector (or the pixel pitch) which translates to the required frequency in order to get a spatial separation of the reconstructed wavefronts. Or in other words, if the periodicity of the fringe pattern could be resolved by the detector.

1.B Scalar Diffraction Theory

We will use the scalar diffraction theory to describe the basic holographic image formation. We start with the Fresnel-Kirchoff diffraction formula for the general problem of diffraction from a 2-D aperture as depicted in Fig. 1.9.

There are different approximations for calculating the diffracted wavefront at Σ. Here we consider the Rayleigh-Sommerfeld diffraction integral, as depicted by Goodman [23], the wavefront at the plane $\Sigma(x, y)$ located at a distance z from the plane (x_0, y_0)) is given by:

$$E(x, y; z) = \frac{ik}{2\pi} \iint E_0(x_0, y_0) \frac{\exp(ik\vec{r})}{|r|} dx_0 dy_0, \tag{1.23}$$

where $E_0(x_0, y_0)$ is the object field over the input plan Σ_0 at $z = 0$, $E(x, y)$ is

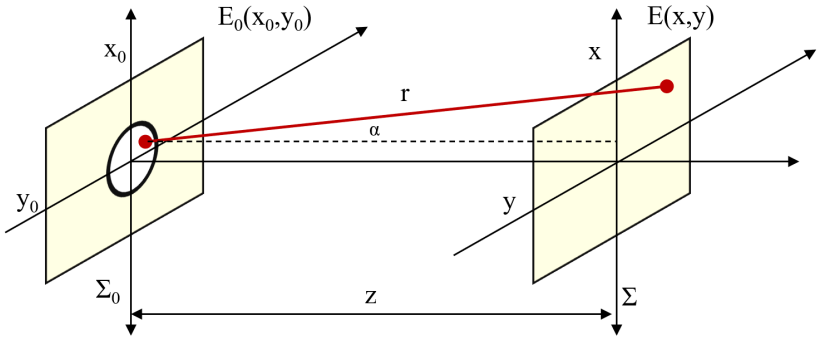

Figure 1.9: Geometry of diffraction. Σ_0 is the input plane and Σ is the output plane

the wavefront over the output plane Σ at z, and k is the wavenumber given by $k = 2\pi/\lambda$ with λ the wavelength. The propagation distance of every point source that is diffracted from within the aperture is:

$$\vec{r} = \sqrt{(x - x_0)^2 + (y - y_0)^2 + z^2}. \tag{1.24}$$

Eq. (1.23) represents the diffraction integral which can be written as a Huygens convolution integral between the object field E_o and the point spread function (PSF):

$$E(x, y; z) = E_0 \otimes S_H = \frac{i}{\lambda} \iint E_0(x_0, y_0) S_H(x - x_0, y - y_0) dx_0 dy_0, \tag{1.25}$$

where S_H is the impulse response of the propagation of a point spread function (PSF) that represents the Huygens spherical wavelet. When the paraxial approximation is valid, for $z^3 \gg \frac{k}{8}[(x - x_0)^2 + (y - y_0)^2]^2_{max}$, the Fresnel PSF is then :

$$S_H(x - x_0, y - y_0; z) = \frac{ik \exp[i\vec{k}\vec{r}]}{2\pi|r|}, \tag{1.26}$$

According to Fourier optics, the convolution integral can also be calculated by multiplying the individual Fourier transforms of E_o and S_H, followed by an inverse Fourier transform. Eq. (1.26) is then given by:

$$E(x, y; z) = i\mathcal{F}\{\mathcal{F}\{[E_o(x_0, y_0)]\}\mathcal{F}\{[S_F(x_0, y_0)]\}\}, \tag{1.27}$$

If the distance z is large compared to $(x - x_0)$ and $(y - y_0)$, the binominal expansion of the square root up to the third term yields

$$r \approx z \left[1 + \frac{(x - x_0)^2}{2z} + \frac{(y - y_0)^2}{2z}\right]. \tag{1.28}$$

By inserting eq.(1.28) to eq.(1.26), we get the Fresnel approximation of the

diffraction integral:

$$E(x,y;z) = \frac{\exp(ikz)\exp\left[ik\frac{x^2+y^2}{2z}\right]}{i\lambda z}\iint E_0(x_0,y_0)\exp\left[ik\frac{\left(x_0^2+y_0^2\right)}{2z}\right] \times \exp\left[-ik\frac{(x_0x+y_0y)}{z}\right]dx_0dy_0, \tag{1.29}$$

If the far-field condition is fulfilled meaning that the distance z is $z \gg k(x_0^2 + y_0^2)/2)$, the term $\exp\left[ik\frac{\left(x_0^2+y_0^2\right)}{2z}\right]$ can be dropped from eq. (1.29), as it is equal to unity. This gives us the following equation:

$$E(x,y;z) = \frac{1}{i\lambda z}\iint E_0(x_0,y_0)\exp\left[-ik\frac{(x_0x+y_0y)}{z}\right]dx_0dy_0. \tag{1.30}$$

Eq. (1.30) is the Fraunhofer diffraction equation which is commonly used to model the diffraction of waves when the diffraction pattern is viewed at a long distance from the diffracting object, but also when it is viewed at the focal plane of an imaging lens [68]. This equation was named in honour of Joseph von Fraunhofer although he was not actually involved in the development of the theory. Throughout the thesis we make use of this equation to explain the propagation of the holograms and to represent the angular spectrum as views in the back focal plane of an imaging lens.

Chapter 2

Diffraction-based overlay metrology using angular-multiplexed acquisition of dark-field digital holograms

In semiconductor device manufacturing optical overlay metrology measures pattern placement between two layers in a chip with sub-nm precision. Continuous improvements in overlay metrology are needed to keep up with shrinking device dimensions in modern chips. This chapter presents the first overlay metrology results using a novel off-axis dark-field digital holographic microscopy concept that acquires multiple holograms in parallel by angular multiplexing. We show that this concept reduces the impact of source intensity fluctuations on the noise in the measured overlay. With our setup we achieved an overlay reproducibility of 0.13 nm and measurements on overlay targets with known programmed overlay values showed good linearity of R= 0.9993. Our data show potential for significant improvement and that digital holographic microscopy is a promising technique for future overlay metrology tools.

The content of this chapter has been published in: Christos Messinis, Theodorus T. M. van Schaijk, Nitesh Pandey, Vasco T. Tenner, Stefan Witte, Johannes F. de Boer, and Arie den Boef, *Diffraction-based overlay metrology using angular-multiplexed acquisition of dark-field digital holograms,* Opt. Express **28**(25): 37419-37435 (24 Nov 2020).

2.1 Introduction

The rapid developments in the micro-electronics industry have been achieved by a continuous and aggressive reduction of the dimensions of semiconductor devices, a trend known as Moore's law [2]. Currently, semiconductor devices like memory and logic CPU's are built 'layer-by-layer' in a sequence of repeating steps of lithography, etching, deposition etc. In order to keep defects under control, metrology of the fabricated features is performed at various stages of the manufacturing process [5].

Multilayered devices with feature sizes of only a few nanometers are in production and require robust metrology of parameters like pattern placement (overlay / OV) and pattern shape (critical dimension / CD) with sub-nm precision (Figure 2.1). In addition, these parameters need to be measured at high throughput on many points on a wafer, requiring short measurement times in the milli-second range [69]. This chapter presents Digital Holographic Microscopy as a promising new technique for OV metrology. In order to clarify the context of our work we will first present a short summary of existing overlay metrology techniques.

2.1.1 Overlay Metrology

Overlay (also called registration error) refers to the lateral displacement of the lithographically exposed and developed pattern in one layer with respect to a previously created underlying structure in another layer. The measurement and control of the overlay between subsequent lithography steps is one of the critical steps in high volume semiconductor manufacturing. Currently the overlay in high-end manufacturing is of the order of 1-2 nm and the precision of overlay metrology is of the order of 0.1-0.2 nm [6].

For many years, Image-Based-Overlay metrology (IBO) was used to measure overlay on so-called box-in-box (BiB) targets. BiB targets consist of an inner-box and an outer-box in, respectively, the developed resist layer and a previously created lower layer [10]. IBO uses a bright-field microscope to create an image of this BiB target and overlay is determined from this image by measuring the position of the inner box edges relative to the outer box edges. Over time these BiB targets were replaced by gratings since a grating image has more edges which improves overlay metrology precision. In practice the optics in an IBO tool have very low aberrations that are well-below the level of what is needed for normal imaging since aberrations can introduce a pattern shift that leads to overlay metrology errors.

In order to deal with the highly demanding overlay requirements of todays semiconductor devices, Diffraction-Based Overlay metrology (DBO) [9, 14, 15] was successfully introduced a few years ago. An overlay target used in DBO consists of small (approximately 5x5 μm^2) overlapping gratings in the resist layer and an underlying layer.

An overlay error between these gratings changes the intensities of the $+1^{st}$ diffraction order (I_{+1}) and the -1^{st} diffraction order (I_{-1}). The intensities I_{+1} and I_{-1} as function of overlay are periodic with a period equal to the grating pitch.

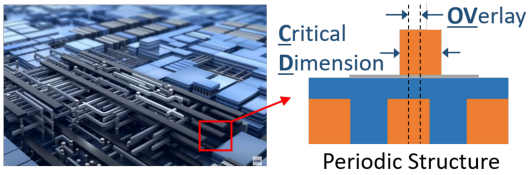

Figure 2.1: A close look at a modern CPU chip. The construction of this chip is simplified on the close look drawing. Silicon integrated circuit layers of various materials are printed on top of each other and the product quality is determined by parameters like OVerlay (OV) and Critical Dimension (CD), shown with black arrows.

In practice, the overlay is much smaller than the pitch so we can linearize the response of I_{+1} and I_{-1} to a small overlay:

$$I_{+1} = I_{ill} \times DE \times (1 + K \times OV), \quad I_{-1} = I_{ill} \times DE \times (1 - K \times OV) \tag{2.1}$$

Here I_{ill} is the intensity of the illumination beam, DE is the diffraction efficiency of the combined gratings at zero overlay and K is an overlay sensitivity term. Taking the difference between I_{+1} and I_{-1} yields:

$$\Delta I \equiv I_{+1} - I_{-1} = 2I_{ill} \times DE \times K \times OV. \tag{2.2}$$

In practice, DE and K are usually not known in advance since they depend on the stack of materials in which the top and bottom gratings are embedded. Moreover, the intensity of the illumination beam can also show some unknown variations. However, these terms can be eliminated by measuring the intensity difference on two pairs of overlapping gratings where a small known shift ("bias") of, respectively, $+d$ and $-d$ is added to the unknown overlay (Fig. 2.2). This results in two measured intensity differences:

$$\Delta I_{+d} = 2I_{ill} \times DE \times K(OV + d), \quad \Delta I_{-d} = 2I_{ill} \times DE \times K(OV - d), \tag{2.3}$$

We have now two measured intensity differences from which we can eliminate the unknown term $(I_{ill} \times DE \times K)$ and determine the overlay [3]:

$$d\frac{\Delta I_{+d} + \Delta I_{-d}}{\Delta I_{+d} - \Delta I_{-d}} = OV. \tag{2.4}$$

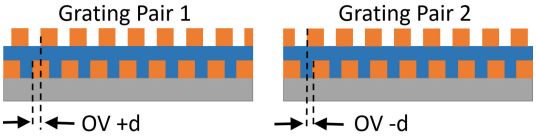

Figure 2.2: Schematic drawing of two pairs of overlapping gratings that have a small programmed shift of respectively $+d$ and $-d$ added to the unknown overlay OV.

The intensity differences ΔI_{+d} and ΔI_{-d} can be measured using, for example, a scatterometer [17] or a dark-field microscope [18]. The advantage of DBO with respect to IBO is that the overlay information is encoded in an intensity difference instead of location of edges in an image. This makes the measurement in DBO less sensitive to aberrations in the optics between the target and the detector. Moreover, in DBO the individual grating lines no longer need to be resolved which allows us to use smaller grating pitches which further improve metrology precision. By using two off-axis illumination beams and a large Numerical Aperture (NA) (≈ 0.8) of the collection optics, pitches as small as 400 nm can be used. However, differential intensity noise between these two off-axis illumination beams must be low since overlay is encoded in an intensity difference between a $+1^{st}$ order and a -1^{st} order.

In practice overlay metrology faces a few challenges that lead to demanding sensor requirements:

1. Targets are small (5x5 μm^2) and are surrounded by patterns that may impact the measured overlay. Therefore sufficient spatial resolution is needed to separate the target from its environment. For dark-field microscopy this means that we need a large NA for the image formation.

2. The bottom grating in DBO is often covered by absorbing layers like amorphous silicon and the top grating is formed in a thin resist layer. This results in low diffraction efficiencies of the $+1^{st}$ and -1^{st} diffraction orders that are used in DBO. In addition, overlay needs to be measured on many points on a wafer for many wafers at high throughput. In practice this means that acquisition times for a DBO image must be in the order of a few milliseconds. The combination of weak signals, small acquisition times and sub-nm precision requirements drives the need for high-brightness light sources.

3. The large variety of materials used in semiconductor devices leads to a strong wavelength-dependency of the signal strength. Moreover, wafer-processing steps like etching can lead to an asymmetric deformation of a grating profile which results in a wavelength-dependent measured overlay. In order to adequately deal with this a DBO tool often measures at multiple wavelengths over a large wavelength range [16, 70, 71].

Single mode lasers have sufficient brightness to deal with the second challenge but they dont have the wavelength flexibility to deal with the third challenge. Supercontinuum sources (SCS), in combination with an Acousto-Optic Tunable Filter (AOTF), are a very attractive alternative for lasers since they offer high brightness and fast and flexible wavelength tuning over a large range. SCS sources, however, tend to show high intensity noise levels [72, 73] that can potentially degrade a DBO-based overlay measurement.

Figure 2.3 shows two possible versions of a dark-field microscope for DBO that both use two oblique illumination beams to illuminate the overlapping grating pairs from opposite sides. In both methods the objective captures only the $+1^{st}$ and -1^{st} diffraction orders and discards specular reflections. These methods form

a $+1^{st}$ order image and a -1^{st} order image of the overlapping grating pairs on an image sensor from which the overlay of these pairs is derived.

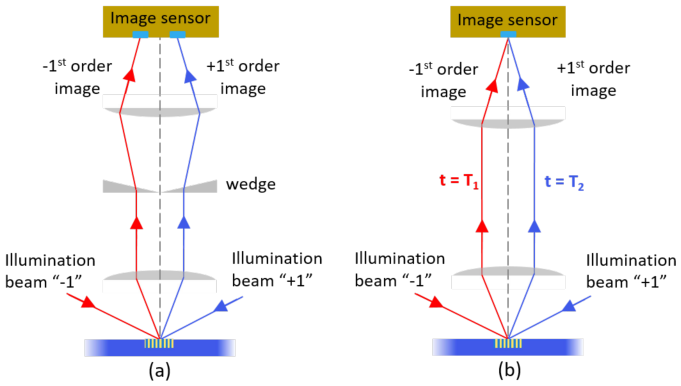

Figure 2.3: (a) Schematic drawing of a dark-field microscopy sensor that measures two diffraction orders simultaneously with the use of a wedge in the pupil plane. The wedge separates the two detected signals in the image plan (camera) offering parallel measurement. (b) Schematic drawing of a dark-field microscopy sensor that uses the full-NA to increase the resolution with sequential measurements of the -1^{st} and $+1^{st}$ diffraction orders at respectively $t=T_1$ and $t=T_2$.

The sensor shown in Fig. 2.3(a) uses a wedge in the pupil plane of the objective that separates the $+1^{st}$ and -1^{st} order images on a camera. This allows parallel measurement of the two images which makes it robust against intensity noise of the light source since this noise is common-mode for the $+1^{st}$ and -1^{st} order images. However, each image can use only half the NA of the objective which lowers the imaging resolution. This resolution loss is solved in the sensor shown in Fig. 2.3(b) where the $+1^{st}$ and -1^{st} order images are measured sequentially in time. In this method, the full NA is available for imaging but the sequential acquisition makes this sensor more susceptible to intensity fluctuations of the light source that can degrade the measurement precision. In the following section, we present in detail a method that enables the full NA for imaging and at the same time offers parallel acquisition of the two diffraction order images.

2.1.2 dark-field Digital Holographic Microscopy

In this chapter we present dark-field off-axis Digital Holographic Microscopy (df-DHM) [74–76] using a SCS plus AOTF as a novel solution for the challenges that we mentioned in the previous section. Our df-DHM achieves a high spatial resolution by using the full NA while at the same time is robust against intensity noise of the source since both -1^{st} and $+1^{st}$ order holograms are acquired in parallel.

Moreover, our df-DHM uses only a simple uncoated plano-asphere imaging lens which offers a high transmission over a large spectral range. Such a simple lens will introduce aberrations but that can be computationally corrected [49]

since DHM retrieves the complex field of an object image [26, 27, 77]. The large spectral range offered by this single imaging lens in combination with the SCS and AOTF also offers a path towards fast multi-wavelength imaging over a large wavelength range.

Another advantage of df-DHM over existing OV measurement techniques is the coherent amplification of the object image that is achieved by the coherent mixing with the reference beam. This coherent amplification lifts the image above the sensor read-out noise and allows quantum noise limited imaging of weakly diffracting overlay targets. This feature is especially of interest for OV metrology applications in the near-IR range where image sensors still tend to have relatively high detector noise levels.

In order to achieve sub-nm precision levels with df-DHM we need a good understanding of various challenges that come with the realization of such a tool. For example, in a previous paper [78], we have reported on the impact of the coherence length of the light source on the field of view (FoV). In this paper we extend our df-DHM investigation towards the parallel acquisition technique that makes the overlay metrology more robust against differential intensity noise in the two off-axis illumination beams.

Parallel acquisition of multiple holograms has already been demonstrated back in 1976 with a detailed review of two-reference-beam holographic interferometry by Dandliker *et al.* [79]. In this paper, it is shown that two-reference-beam holography can be used for quantitative measurements of surface displacements. Pedrini *et al.* [80] extended this approach for quantitative evaluations of image-plane holograms or digital Fresnel holograms to determine both in-plane and out-of-plane deformations at the same time.

Recently, D. Cohoe et al, have also reported a DHM technique that offers a parallel acquisition of three off-axis holograms at three wavelengths [81]. A three-wavelength beam illuminates a transparent sample inside a water-filled chamber and a relay lens is used to project the transmitted light on a camera. A color filter inside the chamber creates three separate reference beams per wavelength which results in three overlapping holograms that each have a different fringe orientation and fringe density. The authors used this method to improve the phase reconstruction of digital holograms of protozoa by reducing 2π phase ambiguities. Similarly, T. Tahara et al, presented a single-shot multi-wavelength off-axis DHM with a wide field-of-view using a large reference angle of more than 40 degrees [82]. This yields a very dense fringe pattern and the intentional aliasing that is introduced by this dense fringe pattern in combination with the relatively large pixel pitch results in a wide separation of the multi-colored signal in the spatial frequency domain.

In this chapter we report the use of this parallel image acquisition technique for overlay metrology using df-DHM. In contrast to the previous research on this topic we use this parallel imaging technique to measure small intensity differences between the two images. We present the first measured overlay data on a test sample that demonstrates that parallel imaging reduces the impact of intensity noise of the light source and thus improves the measurement reproducibility. In what follows, Section 2.2 provides a very brief review of DHM, followed by an

explanation of how we realize the parallel acquisition of multiple holograms. This is then followed by a detailed description of the novel off-axis dark-field DHM setup that we have built (Section 2.3). Section 2.4 presents the first experimental results that demonstrate the parallel acquisition (Section 2.4.1), the first overlay measurements with off-axis df-DHM (Section 2.4.2), and the verification of the noise correlation of the presented setup along with measured overlay reproducibility (Section 2.4.3). Section 2.5 concludes this chapter.

2.2 Off-Axis Dark-Field Digital Holographic Microscope

This section presents the details of how we realize the parallel acquisition of multiple holograms using off-axis df-DHM. We first briefly present some theoretical background of our technique. Then we describe the setup that we have built to demonstrate the capabilities of this technique for semiconductor overlay metrology.

2.2.1 Theoretical Analysis of Off-axis df-DHM

In df-DHM the object is usually illuminated at an oblique angle of incidence. The specular reflection is discarded and part of the diffracted light is captured by a lens with a numerical aperture (NA). The captured light creates a dark-field image on an image sensor with magnification M and an off-axis reference beam is coherently added to this dark-field image which results in an intensity pattern on the image sensor given by:

$$I(\vec{r}) = E_{obj}(\vec{r})E^*_{obj}(\vec{r}) + E_{ref}(\vec{r})E^*_{ref}(\vec{r}) + \gamma E_{ref}(\vec{r})E^*_{obj}(\vec{r}) + \gamma E_{obj}(\vec{r})E^*_{ref}(\vec{r}) \tag{2.5}$$

where $E_{\mathrm{obj}}(\vec{r})$ is the complex amplitude distribution of the object wave, $E_{\mathrm{ref}}(\vec{r})$ is the reference wave and γ is the degree of coherence between the object beam and the reference beam.

The last term of Eq.(2.5) is of interest as it contains the complex object field, $E_{\mathrm{obj}}(\vec{r})$, that we need to retrieve. It is however multiplied by the reference field. In off-axis DHM the reference beam is usually a plane wave with amplitude A that is incident on the image sensor at an angle of incidence of θ_{ref} and an azimuthal angle ϕ_{ref}. Applying a 2D-Fourier Transform (FT) to the detected image and assuming an infinite plane wave reference beam yields the spatial frequency spectrum in k-space:

$$\tilde{I}(\vec{k}) = E_{obj}(\vec{k}) \otimes E^*_{obj}(\vec{k}) + A^2\delta(\vec{k}) + \gamma A E^*_{obj}(\vec{k}+\vec{k}_{ref})) + \gamma A E_{obj}(\vec{k}-\vec{k}_{ref}) \tag{2.6}$$

where $\otimes$ denotes a convolution. Of these four terms, the first is the auto-correlation of the object beam $E_{\mathrm{obj}}(\vec{k})$ which has a diameter of $4\pi(\mathrm{NA}/\mathrm{M})/\lambda$ and is centered at the origin. Likewise, the second term is the auto-correlation of the reference beam $E_{\mathrm{ref}}(\vec{k})$, resulting in a delta function placed at the origin (Figure 2.4.b). These two terms are the DC components of the recorded intensity.

The last two terms are cross-correlation terms that describe the interference between the object and reference beams. These terms are the Fourier transforms of the shifted object beam and its complex conjugate, respectively. The magnitude of the shift, $|\vec{k}_{ref}|$ is given by:

$$|\vec{k}_{ref}| = \frac{2\pi \sin\theta_{ref}}{\lambda} \tag{2.7}$$

where θ_{ref} is the angle of the reference beam. In order to fully recover the object wave distribution, these side-bands need to be completely separated from the base-band. In case of incomplete separation, imaging artifacts may occur which can only be removed with advanced algorithms [83]. As a side-band separation is preferred we can determine the required angle of the reference beam. According to Eq. (2.6) the side-bands are completely separated from the base-band term if $|\vec{k}_{\mathrm{ref}}| > 6\pi(\mathrm{NA/M})/\lambda$.

At the same time, the Nyquist sampling criterion [84] sets an upper limit on the maximum angle-of-incidence of the reference beam. For an image sensor pixel pitch of p_x we require that $|\vec{k}_{ref}| + 2\pi(\mathrm{NA/M})/\lambda < 2\pi/2\mathrm{p}_x$. These two conditions are summarized in the following expression:

$$\frac{\lambda}{2p_x} - \frac{NA}{M} > \sin\theta_{ref} > \frac{3NA}{M} \tag{2.8}$$

If this condition is satisfied then the hologram is adequately sampled and the two side-bands are separated from the base-band in the Fourier domain. For example, an NA=0.5, a magnification M of 100x, a wavelength of 550 nm and a typical image sensor pixel size of 4 µm results in a reference angle between 0.86° and 3.65°.

Retrieving the complex object field from an off-axis hologram requires only a few simple signal processing steps. Fourier transforming the acquired hologram yields the 2D-spatial frequency spectrum. Then by selecting only one of the two side-bands and filtering out the rest of the signal we obtain the spectrum of the object field. Finally we obtain the complex object field with an inverse Fourier Transform of this object spectrum.

This concept can be extended to retrieve multiple dark-field images in a single multiplexed hologram. Our approach is schematically shown in Figure 2.4. Instead of using one illumination beam and a corresponding reference beam we now use two illumination beams that each generate two object beams that are projected on the image sensor. To each of these object beams we add two corresponding reference beams and we use coherence gating [85, 86] to ensure that each object beam only adds coherently with its corresponding reference beam. In addition, we also give the two reference beams different azimuthal angles resulting in a different orientation of the side-bands of the spectra of the resulting holograms as shown in Figure 2.4(b). With this approach, two holograms are captured by the image sensor using only one image acquisition, and the two object fields can be retrieved with only three Fast Fourier Transforms (FFT's).

This method is essentially a form of frequency multiplexing, which is already

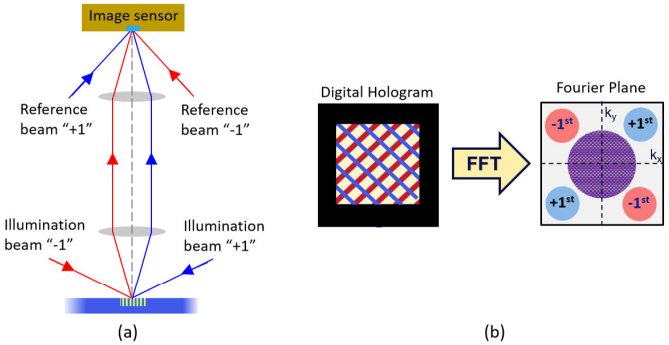

Figure 2.4: (a) Schematic drawing of an off-axis dark-field digital holographic microscope. Camera image contains two interference patterns initially introduced by the two separate branches. (b) Spatial frequency domain representation of the detected signals. The illumination branches have different azimuthal angles in the reference arms resulting in a 90° angle difference.

used in telecommunications for multiplexing signals [87]. Compared to time domain signals, images have 2D spatial frequency spectra which offers a lot of room to fill the frequency spectrum with multiple object fields that can all be acquired in a single image acquisition. The number of object fields that can ultimately be packed in the spatial frequency-domain depends on the pixel size of the image sensor (according to Eq. (2.8)) and dynamic range. With the continuous improvements of image sensor technology we expect that this technique can be scaled-up to ultimately acquire more than four object fields in parallel.

In our off-axis DHM the reference beams are placed at azimuthal angles of nominally +45° and +135° relative to the x-axis. For convenience we refer to these beams as Ref_{-1} and Ref_{+1}. The target is illuminated from opposite directions which generates two object beams ill_{-1} and ill_{+1} that are imaged on the camera.

2.3 off-axis df-DHM setup

Figure 2.5 shows the novel off-axis dark-field digital holographic microscope that was built to demonstrate the parallel acquisition of multiple holograms scheme that was presented in the previous section.

The off-axis df-DHM setup is comprised of a fiber coupled Supercontinuum White light source (LS ; Leukos Rock 400 5) combined with an Acousto-Optical Tunable Filter (AOTF ; Gooch & Housego TF550-300-4-6-GH57A). This AOTF device provides beams with a bandwidth in the range of [4–7 nm] and covers the whole visible range [400–700 nm]. We also added dichroic mirrors and bandpass filters in front of the AOTF to block longer wavelengths of the source. This AOTF was selected based on considerations that will be presented in Chapter 3 ([78]), where we will show that the required Field-of-View (FoV) (100 µm) for

semiconductor metrology in a df-DHM setup can be achieved with light sources with bandwidth of about 5 nm. With this combination we get a horizontally polarized laser beam with an optical power of more than 1 mW. The AOTF introduces some wavefront distortions which we remove using a spatial filter to improve the wavefront quality and to obtain a beam with a Gaussian beam profile.

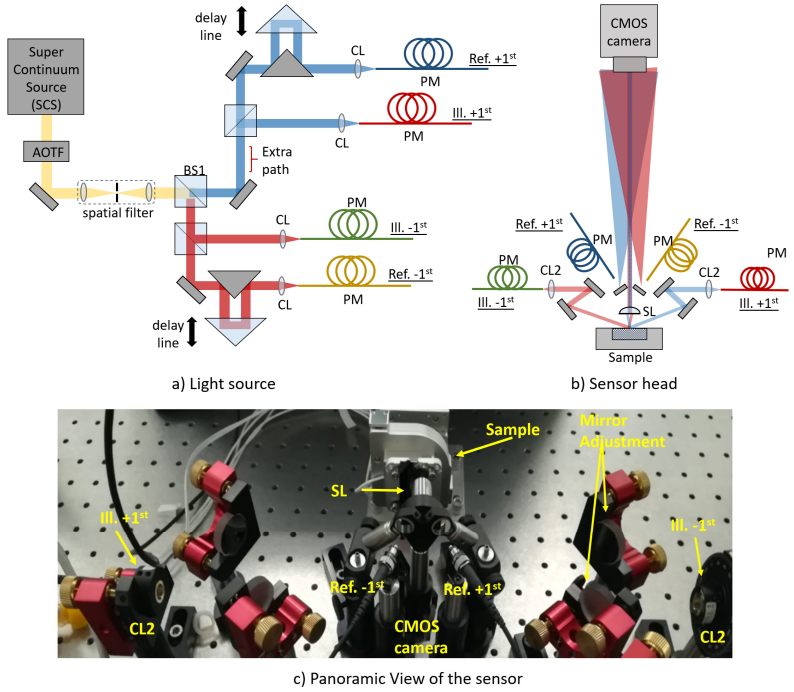

Figure 2.5: Detailed drawing of df-DHM holographic setup. a) Light source. On the left-hand side the light source and the AOTF direct the illumination beam to the interferometric part of the setup. A 50/50 beam splitter separates the light in two branch ($+1^{st}$ and -1^{st} branch) where two additional 90/10 beam splitters splits the light between illumination and reference arm. With collimators (CL) and polarization maintaining single mode fibers (PM) the four paths are coupled and sent to the microscope. b) Sensor head. On the microscope, the four paths are distributed in two illumination and two reference arms. With collimator lenses (CL2) we illuminate the sample at an incident angle of $\approx 70°$ and the generated diffraction orders are captured by a single lens (SL) and are recombined with the reference arms on the CMOS camera. c) A panoramic view of the illuminator is presented, showing the azimuthal angles of the two reference arms.

For the parallel acquisition of $+1^{st}$ and -1^{st} order we separated the beam in two paths using a 50/50 beam splitter (BS1; Thorlabs BS013) and for each path we added a 90/10 beam splitter (BS2; Thorlabs BS025) that splits 10% of the light in the reference beam and the remaining 90% of the light in the illumination beam. As shown in Fig. 2.5, we matched the distances of each beam pair

(illumination beam and reference beam) with the use of delay lines so that the optical path difference (OPD) between each pair is minimized. In addition, we have also introduced an optical path length difference between the two pairs of approximately 10 cm. This is well beyond the (24 µm) coherence length of the light source which ensures that we have two mutually incoherent holograms on the camera.

Our df-DHM setup uses four polarization maintaining (PM) fibers (PM - Shafter-Kirchhoff PMC-400Si-2.3-NA014) with a nominal length of 1.5 meters to couple the two illumination beams and the two reference beams to the holographic microscope head with collimation lenses (CL; Schafter Kirchhoff 60FC-M10-01). This separates the "light source" from the "sensor head" and offers flexibility to build a compact df-DHM inside a metrology system where volume constraints can be challenging. Realizing a stable fiber coupling, however, is a challenge since small beam pointing fluctuations can lead to variations in coupling efficiency [88, 89] that creates small additional beam intensity fluctuations at the fiber output. In order to minimize this effect we have placed the optics in front of the fibers in a separate housing that reduces beam pointing fluctuations. This resulted in coupling efficiencies of approximately 60% for all the four arms. The first results that we got from this setup and that we will present in section 2.4 indicate that this simple approach already reduces the intensity noise in the illumination beams to acceptable levels.

The microscope has two off-axis illumination arms which illuminate the target from opposite directions at an incident angle of $\approx 70°$ with respect to the normal of the sample plane. Each illumination arm consist of a collimation lens (CL2; Schafter Kirchhoff 60FC-M3.1-51) resulting in a large illumination spot of $\approx$ (500 µm). Two adjustable mirrors were used for fine-tuning the angle of incidence using the approach that is described in Chapter 3.

The objective lens is a plano-asphere lens with effective focal length of 8 mm and an NA of 0.5 (SL ; Thorlabs A240TM). With this NA the setup of Fig. 2.5 is capable of imaging small gratings with pitches down to 400 nm. We choose a nominal magnification of 100x by placing our detector 800 mm away from the SL. A camera (Basler acA4112-8gm) with a 12 Mpixel CMOS image sensor with 3.45 µm pixel size was used.

According to eq. (2.8) the 3.45 µm pixel size and the 100x magnification yields an upper and lower limit of θ_{ref} of, respectively, 3° and 0.86° (for the shortest wavelength). In our setup we set θ_{ref} to approximately 1° for both reference beams. This was measured from the angular spectrum of a measured hologram. The azimuthal angles of the two holograms were measured from the angle between a horizontal line and the line through the origin of the spectrum and the center of the side-band. The azimuthal angles were 37.5° and 142.8° respectively.

Our microscope uses a single imaging lens which adds a parabolic phase profile to the object image on the camera [23]. We can compensate for this curvature by also using a spherical reference wavefront. We realize this by directing the spherical wave that is radiated from the reference fiber directly to the image sensor without using a collimation lens.

2.4 Experimental Results

This section presents the first experimental results that demonstrate the diffraction-based overlay metrology capabilities of our df-DHM setup. For these experiments we used an ASML test wafer with multiple targets. The square gratings printed on this wafer have various pitches, P, ranging from 400 to 1200 nm and various sizes ranging from 58x58 μm^2 to 5x5 μm^2. Firstly, we present the parallel acquisition of multiple holograms followed by the first OV measurements on targets with a known pre-programmed overlay where we compare the measured values with these pre-programmed values. Finally, we present measured overlay reproducability data that demonstrate that our parallel image acquisition setup reduces the impact of intensity noise.

2.4.1 Parallel acquisition of multiple holograms

Firstly, we measured the actual magnification M of the setup. We measured M by collecting dark-field images of a known target. The silicon wafer that we used contained square gratings with dimensions of 58x58 μm^2 and etch depth of 90 nm. From the measured image size of this target on the camera we obtained a 100x magnification with an uncertainty of approximately $\pm$ 0.5 which is based on five repeated measurements.

In order to demonstrate our concept of parallel acquisition, we set the center wavelength at 532 nm with the AOTF. At this wavelength the bandwidth B is approximately 6 nm. This wavelength ensured that most of the diffracted light travels through the center region of the lens. This improved the imaging performance since lens aberrations are not yet corrected for in the experiments that we report here.

For the image acquisition, the delay lines of the reference arms (Fig. 2.5) were adjusted to ensure that the maxima of the observed fringe patterns were centered in the images. Then we acquired several holographic images of different targets of this test wafer. Fig. 2.6(a) shows two overlapping holograms of two square gratings in one camera image. The presented targets are two square top-only (resist only) gratings with dimensions of 38x38 μm^2 and etch depth of 90 nm.

The large 1° tilt angle of the reference beam results in a large fringe density and only if we enlarge the area of interest we can see the fringe pattern that is formed by the two overlapping off-axis holograms. Fig. 2.6(b) presents the angular spectrum of the detected image, obtained with a Fast Fourier Transform (FFT). This image shows that the cross-correlation terms of the two overlapping fringe patterns are fully separated.

Figure 2.6 presents the reconstruction steps needed to retrieve the amplitude and phase of the obtained object field. From Fig. 2.6(b) we selected the two cross-correlation terms located on top-left and top-right of the image. These areas contain the cross-correlation information for image reconstruction of the -1st and +1st order images. As shown, top left is the side-band of the -1st order image and top right is the side-band of the +1st order image while the side-bands at the bottom of the image are their complex conjugates, as explained in section

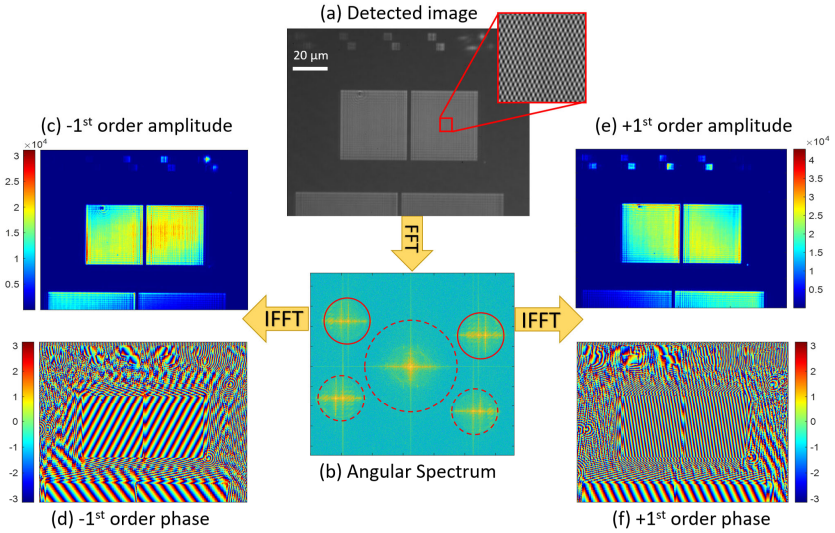

Figure 2.6: Off-axis df-DHM process for a semiconductor wafer.(a) Recorded Hologram with two interference patterns;(b) angular spectrum,with the cross-correlation term used for the reconstruction within the solid red circled areas, top left for the -1st diffraction order and top right for the +1st diffraction order;(c),(d) amplitude and phase reconstruction for -1st order; and (e),(f) amplitude and phase reconstruction for +1st order.

2.2.1.

The side-bands in the spatial frequency spectrum show multiple displaced bright spots that correspond to the different pitches of the gratings that are present in the image. Figure 2.6(c),(e) show the intensity and Fig. 2.6(d),(f) show the phase of the retrieved images of -1st order and +1st order respectively. The phase images represent a phase profile of the optical field reflected from the surface of the target. For targets with different pitches we expect different phase profiles, similarly displayed in the spatial frequency domain.

2.4.2 Overlay measurements with off-axis df-DHM

After demonstrating the parallel acquisition of multiple holograms, we move to the next step where we demonstrate the use of our DHM concept for overlay metrology. The presented off-axis df-DHM can simultaneously measure the +1st and -1st diffraction orders which can be used to calculate overlay using Eq. (2.4).

The silicon test wafer that was used for our measurements contains various diffraction-based overlay targets with programmed overlay values in a range of -20 nm to +20 nm. Each target consist of two overlapping grating pairs as shown in Fig. 2.2 with a bias d of +20 nm and -20 nm that was added to the programmed overlay. The size of each grating pair is 38x38 µm^2, the same as the ones shown on Fig. 2.6.

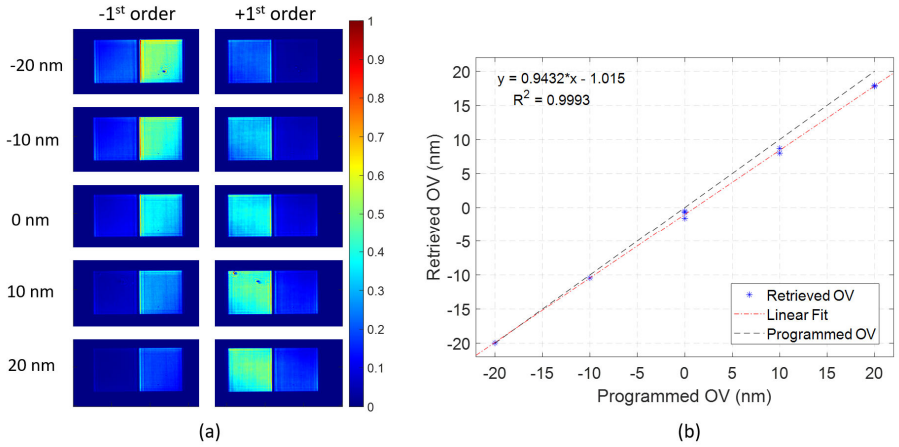

Figure 2.7: Overlay measurements of targets with known bias. (a) Reconstructed Amplitudes for $+1^{st}$ and -1^{st} order; (b) Plot of the programmed OV versus retrieved OV. Black dashed line is the expected OV while the red dotted line is the linear fit of the retrieved OV spots (red dots)

Fig. 2.7(a) presents the retrieved -1^{st} and $+1^{st}$ order images for targets with various programmed OV errors and using a wavelength of 532 nm. These retrieved images were obtained using the method described in Section 2.4.1. In our setup the two illumination spots have a small intensity difference that leads to significant overlay offsets. In order to correct for this we also measured a reference resist grating without the etched grating underneath. For such a grating an unbalance in the measured $+1^{st}$ order and -1^{st} order images can only come from an unbalance in the two illumination intensities. The measured intensities for this reference grating have therefore been used to correct for the illumination unbalance in the overlay measurements.

In order to come to an overlay number we determined the total signal level for the -1^{st} order image and the $+1^{st}$ order image in a Region-of-Interest (RoI). The RoI size was 10x10 μm^2 and was centered on the two grating pairs. This is done for the positively biased grating pair (d=+20 nm) and the negatively biased grating pair (d=-20 nm). This yields two intensity difference signals of ΔI_{+d} and ΔI_{-d} that allow us to calculate overlay with eq.(2.4).

Fig. 2.7(b) presents measured OV as a function of the programmed OV. The black dashed line shows the expected OV while the red dotted line is a linear fit of the experimental data. A comparison of the measurements and the programmed OV are off by approximately 1 nm. Our measurements show good matching to a linear fit of the measured data ($R^2 = 0.9993$), which only shows small deviations from the expected value. The observed average -1 nm offset between measured and programmed overlay can be explained by the estimated 1 nm OV uncertainty that can occur during the lithographic patterning step of the resist grating. In addition we have also observed a small drift in our breadboard that may also

contribute to this offset.

2.4.3 Differential intensity noise and measured Overlay Reproducibility

DBO encodes overlay in a small intensity difference between the $+1^{st}$ and -1^{st} images which makes it only sensitive to differential intensity noise in the illumination beams since common-mode noise in the measured $+1^{st}$ and -1^{st} order images will drop-out in the difference. We use a single light source for measuring these images so ideally the differential noise in the measured images should be zero. However, our setup uses single-mode fibers to guide the two illumination and two reference beams to the microscope head and, as noted in section 2.3, small fluctuations in the fiber coupling efficiency can introduce some differential intensity noise to the illumination and reference beams.

The impact of intensity fluctuations in the illumination beams on the measured overlay can be modeled with the DBO signal formation model that we presented in the introduction. Denoting the normalized intensity fluctuations on the $+1^{st}$ and -1^{st} order illumination beam by ϵ_{+1} and ϵ_{-1} yields for the detected DBO signals:

$$I_{+1,\pm d} = I_{ill} \times DE \times (1+\epsilon_{+1})(1+K\times(OV\pm d)), \tag{2.9}$$

$$I_{-1,\pm d} = I_{ill} \times DE \times (1+\epsilon_{-1})(1-K\times(OV\pm d)) \tag{2.10}$$

Taking the difference $\Delta I_{\pm d} = I_{+1} - I_{-1}$ and substituting these differences in eq.(2.4) using the approximation that $1(1+\epsilon) = 1-\epsilon$ for $\epsilon \ll 1$, yields for the noise δOV in the measured overlay:

$$\delta OV = \frac{\epsilon_{+1}-\epsilon_{-1}}{2K} - \frac{\epsilon_{+1}^2-\epsilon_{-1}^2}{4K}. \tag{2.11}$$

The noise terms $\epsilon_{\pm 1}$ are of the order of 1% so we ignore the second term on the right-hand side. It can be seen that only differential noise will result in an overlay error. In practice K is of the order of 10^{-2} nm^{-1} [90] so for overlay errors less than 0.1 nm the normalized differential noise $\epsilon_{+1}-\epsilon_{-1}$ must be below 10^{-3}.

Figure 2.8(a) shows the measured normalized intensity fluctuations of the two illumination beams. This data was obtained by redirecting the two illumination beams to a CCD camera (Vimba Prosilica GT2300 with 4.1 Mpixels of 4.5 µm pixel size) and acquiring 100 images with an acquisition time of 50 µs over a time interval of about 100 seconds. The intensity in each beam was determined by summing the signal levels of those pixels that are covered by an illumination spot. As a final step we normalized the measured intensity to the mean value of all 100 measurements. The result shown in Fig. 2.8(a) clearly shows highly correlated intensity fluctuations in the "$+1^{st}$ illumination" and "-1^{st} illumination" beams. The differential noise has a standard deviation of 6.7×10^{-4} and a correlation coefficient of 0.98. This encouraging result shows that the impact of fiber coupling fluctuations is small compared to the intensity noise of the source.

In holography, however, intensity noise in the reference beams also shows up

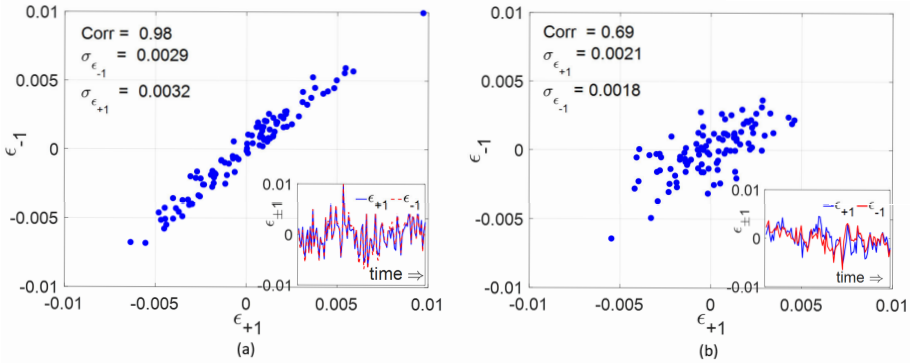

Figure 2.8: Normalized intensity fluctuations over 100 images that were acquired over a time interval of approximately 120 s. (a) Noise correlation between the two illumination beams spots for 100 measured intensities, here Corr is the correlation coefficient and σ_ϵ is the standard deviation of the intensity fluctuations the two signals. The fluctuations over time are presented in the bottom right corner; (b) Noise correlation between the two reference beams spots for 100 measured intensities. The fluctuations over time are presented in the bottom right corner.

as noise in the first order images so we also measured the intensity fluctuations for the two reference beams using the same procedure as described above for the illumination beams. Since the reference beams have lower intensities we used a longer acquisition time of 500 µs. The result of the measured normalized intensity fluctuations for the reference beams is shown in Fig 2.8(b). This measurement was separately done from the measured illumination beams so a point-to-point comparison of the measured noise between illumination and reference beams is not possible. Fig 2.8(b) shows that the standard deviation of the observed noise is comparable to the noise in the illumination beams (standard deviation of the differential noise is 1.5×10^{-3}). However, we clearly see that the correlation between the two reference beams is not as good as what we observe in the illumination beams. The measured correlation is only 0.69 which indicates that we suffer from some fluctuations in the fiber coupling efficiency in one (or potentially both) of the reference fibers. This is supported by the fact that one of the reference beams in the current setup travels a much longer path through air before it is being coupled in the fiber. Since we have achieved such encouraging results on the illumination fibers we are confident that we can ultimately also achieve a good noise correlation between the reference beams.

After characterizing the differential noise in the illumination and reference beam we moved on to characterize the differential noise in the $+1^{st}$ and -1^{st} order images that we acquired with our df-DHM setup. Fig. 2.9 shows the normalized signal variations in the retrieved $+1^{st}$ and -1^{st} order images that we measured with our df-DHM setup. This was done by collecting 100 holograms at an acquisition time of 30 ms and measuring the signal levels in the $+1^{st}$ order and -1^{st} order signals. The signal is formed by a coherent addition of a reference beam and an object beam so we can expect that the noise has contributions from

the illumination and reference beams and possibly also from air turbulence that can lead to contrast loss fluctuations of the interference pattern.

The data in Fig. 2.9 show that the -1st order and +1st order signals have an encouraging correlation of 0.91. However, we also observe a difference in the magnitude of the noise that will result in an incomplete cancellation of the noise in the measured intensity difference. The measured data indicates that a combination of sub-optimal fiber coupling and beam pointing fluctuations is currently preventing us from achieving a complete suppression of the differential noise. We believe that better fiber couplers and shorter beam paths before the fiber couplers will solve this problem.

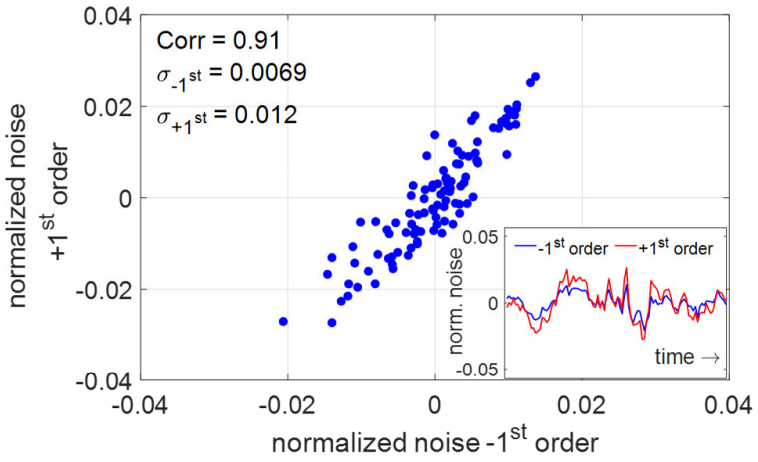

Figure 2.9: Correlation between the normalized intensity noise between -1st and +1st reconstructed amplitudes. The normalized noise over time is presented on the bottom right corner.

Figure 2.10(a), presents measured overlay reproducibility data on nine different overlay targets for both a parallel and a sequential acquisition of the +1st and -1st order images. These results were obtained by doing 150 overlay measurements for each target and calculating the standard deviation of the overlay variation. It can be seen that parallel acquisition consistently has a better reproducibility which is due to the suppression of the common mode intensity noise.

The measured reproducibility of the parallel acquisition is of the order of 0.13 nm which is promising since this already approaches the level of what is needed for overlay metrology. Moreover, we have to bear in mind that this result was obtained on a simple breadboard setup where we could not yet achieve a complete suppression of the differential noise in the illumination beams. It is expected that a more stable setup will significantly improve the reproducibility which will make the benefit of parallel acquisition over a sequential acquisition even more pronounced.

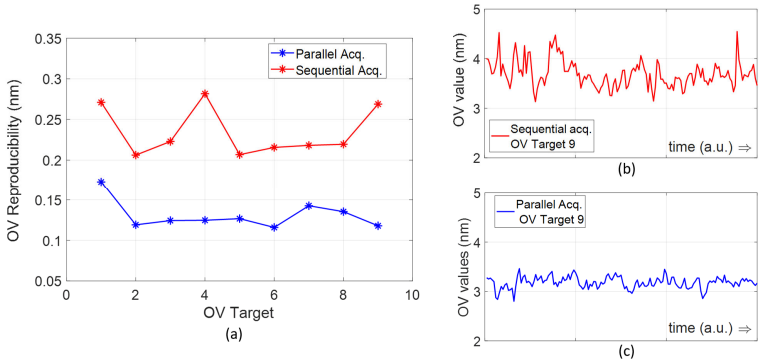

Figure 2.10: (a) Measured overlay reproducibility data for nine OV targets. Red line presents the measured values for sequential acquisition and blue line for the parallel acquisition. (b) shows the OV variation for OV Target 9 over time for sequential acquisition and (c) for parallel acquisition.

2.5 Conclusion

We have presented a novel concept for measuring overlay based on spatial frequency multiplexed dark-field Digital Holography (df-DHM). We have also presented first measured overlay data using this concept. We have built a breadboard version of this concept using standard off-the-shelf components and only a single imaging lens. This setup was not yet optimized for mechanical stability and alignment. Moreover, the retrieved images were not yet corrected for aberrations that are introduced by the single imaging lens. Despite these minor imperfections the measured data shows the potential of using df-DHM for overlay metrology.

After an experimental demonstration of the capability to acquire two holograms in parallel we have presented data showing good agreement between measured overlay and programmed overlay on a test sample. The linearity was very good (R^2 =0.9993) and the maximum observed deviation of about 1 nm between the measured overlay and the expected overlay can be explained by a combination of overlay uncertainty in the test sample ($\approx$ 1 nm) and overlay errors ($\approx$ 1 nm) that are introduced by various small imperfections in our breadboard setup. For example, a small mechanical misalignment of the stage on which the sample was mounted in combination with a small illumination beam inhomogeneity can already introduce a 1 % relative intensity unbalance between $+1^{st}$ order and -1^{st} order images. For our sample this 1 % unbalance would already lead to a 1 nm error.

Diffraction-Based overlay measurements are sensitive to differential noise in the illumination beams that generate the $+1^{st}$ and -1^{st} order images so we have also looked in the noise performance of our df-DHM setup. The two illumination beams and the two reference beams originate from the same source so ideally the noise between these four beams is common mode with no differential noise terms. Measured data on the two illumination beams clearly show a strong com-

mon mode noise term that cancels in the overlay measurement and only a small differential noise term that has a negligible impact on the overlay measurement. Unfortunately, the two reference beams show a significant differential noise term on top of the common-mode noise. After carefully studying this effect we have come to the conclusion that this is most likely coming from a small fiber misalignment in combination with small beam point fluctuations of the beams that are coupled into the single mode fibers. Despite these imperfections we have been able to show 0.12 nm overlay reproducibility using parallel acquisitions.

During the course of our investigations we have identified various improvements to our setup that we will implement in future experiments. For example, more stable fiber couplers in combinations with shorter beam paths in the illuminator part are expected to significantly reduce the differential noise. Better aligned sample stages in combination with a more homogenous illumination beam are expected to significantly improve the overlay metrology precision to the levels that are required in the semiconductor industry. Once we have also calibrated the lens aberrations we can also apply image corrections enabling overlay measurements over a larger wavelength range. In this paper, we have shown that df-DHM is a very promising candidate for future overlay metrology and we are working on many directions for further improvements.

Chapter 3

Study on the Impact of coherence length on the field of view in dark-field holographic microscopy

In this chapter we perform a feasibility study of the limitations of the use of dark-field Digital Holographic Microscopy due to the impact of the coherence length. This report is essential as it confirms that df-DHM can be a promising optical metrology technique that uses optics with acceptable complexity. A theoretical analysis and an experimental demonstration of this technique is presented, showing the impact of the coherence length of the light source on the Field-of-View. At the end of the chapter we also present the first holographically obtained images of metrology targets with the first iteration of a df-DHM test setup.

3.1 Introduction

The aggressive reduction of semiconductor devices according to Moores law [2] has driven many improvements in optical wafer metrology and semiconductor processing equipment such as lithography. Currently, chips with feature sizes

The content of this chapter has been published in: Christos Messinis, Vasco T. Tenner, Johannes F. De Boer, Stefan Witte, and Arie den Boef, *Impact of coherence length on the field of view in dark-field holographic microscopy for semiconductor metrology: theoretical and experimental comparisons,* Appl. Opt. **59**(11): 3498-3507 (7 Apr 2020).

below 10 nm are in production and require robust metrology of parameters like pattern placement [overlay (OV)] and pattern shape [critical dimension [CD]) with sub-nanometer precision. In addition, these parameters need to be measured at high throughput on many points on a wafer, requiring small measurement times in the millisecond range [69].

Over the years, several studies and industrialized products have investigated optical techniques for CD and OV metrology, like scatterometry [3, 14, 91]. For pattern placement measurements, diffraction-based overlay metrology (DBO) has emerged as a robust scatterometry-based technique [16, 70, 71].

DBO technology measures the overlay of small overlapping diffraction gratings ($<$ 5x5 µm^2) printed on a multilayered semiconductor wafer by measuring a small intensity difference between the +1st (I_{+1}) and -1st (I_{-1}) diffraction order, which scales linearly with the overlay error between these gratings according to [3]:

$$\frac{I_{+1} - I_{-1}}{I_{+1} + I_{-1}} = K \times OV. \tag{3.1}$$

For convenience, we have normalized the intensity difference to the total intensity. The scale factor K is a sensitivity parameter that depends on the material properties of the thin film stack in which the gratings are embedded. This unknown scale factor K is eliminated by measuring the intensity difference on 2 pairs of overlapping gratings where a small known shift ("bias") of, respectively, $+d$ and $-d$ is added to the unknown overlay, as presented in the previous chapter. In practice K can become as small as 10^{-2} nm^{-1} which results in the need for an accurate and robust measurement of the +1st and -1st order intensities. This is only possible if the 0th order light coming back from the target is effectively suppressed using dark-field imaging techniques.

Good accuracy and robustness is achieved by a careful selection of 1 or more wavelengths [16]. Due to the large variety of materials in modern semiconductor devices, these optimum wavelengths can cover a large range from 400 nm up to 900 nm. Fast (sub-ms) wavelength tunability over a large range can be provided by a super-continuum source in combination with an acousto-optic tunable filter (AOTF). These sources provide an illumination intensity of more than 1 mW/nm which is needed for metrology with sub-nm precision on small metrology gratings ($<$ 5x5 µm^2) that can have a low diffraction efficiency ($<$ 0.01 %). Shot noise considerations show that the noise in DBO scales with $P/\sqrt{N}$ where P is the grating pitch and N is the number of detected photons. Using this approximate formula shows that we need to detect $\approx 10^6$ photons for sub-nm noise levels. Assuming a diffraction efficiency of a DBO grating pair of 0.01 % and a total sensor transmission of about 10 % leads to a required illumination power of about 4 mW. This is achievable with a super-continuum source and an AOTF that has a bandwidth of about 4 nm.

The need to measure with high-precision on small gratings also drives the need for high NA optics that must have low aberrations over a large wavelength range and with a sufficiently large transmission. As a result of these challenging requirements modern metrology tools use complex high-precision optics.

As a consequence of Moores law, overlay metrology requirements will continue to tighten so we can expect that this will lead to even more complex optics, meaning higher number of optical surfaces. In order to deal with this trend, dark-field Digital Holographic Microscopy (df-DHM) can be a potential technique to meet the challenging future metrology requirements with a few lens elements (preferably one) which allow high transmission over a large wavelength range. With df-DHM we measure the complex field on a camera which allows the use of computational techniques to correct for residual imaging imperfections that would give rise to metrology errors [92, 93].

Recently, C. Shen et al, reported on a similar optical metrology challenge where aberration correction over a large wavelength range was needed in the field of silicon chip imaging [12]. They proposed a multi-spectral microscope system using aperture-scanning Fourier ptychographic microscopy for phase retrieval. Our application, however, requires measurement times well below a fraction of a second which is highly challenging with iterative phase-retrieval techniques but quite feasible with digital holographic microscopy (DHM).

In essence, digital holographic microscopy (DHM) is a well know technique that has already been described in many papers like references [26, 27, 41, 77, 94–101]. In summary, in DHM the light scattered from the sample (object field) is coherently mixed with a reference beam resulting in an interference pattern on the camera that allow the acquisition of both amplitude and phase of diffracted fields [26, 94]. In our investigation we look into dark-field DHM since specularly reflected light often has a low sensitivity for the parameter of interest like overlay and we therefore do not want to include the 0^{th} order in the image acquisition.

Comparing to other techniques, the main advantage of DHM is that it offers the capability to image small scattering targets (of a computer chip) that can have a diffraction efficiency as low as 0.01 % simply by boosting the detected signal with a reference by the virtue of coherent amplification.

Many holographic systems have already been presented [95, 98–100], which can be categorized in two main groups, in-line and off-axis systems. In-line holographic systems are characterized by a nominally zero angle between the object and the reference beam, where a sequence of measurements is used to determine the complex field and is known as phase-shifting interferometry (PSI) [97, 101]. Conversely, off-axis systems use an angularly offset reference wave, as was originally done by Leith and Upatnieks [77], offering a single-shot acquisition of the complex field by separating the two beams in spatial frequencies [41, 100].

Several groups have already reported df-DHM. For instance, Dubois and Grosfils used df-DHM to improve the detection of 3D nanosized particles smaller than the resolution limit [74]. Likewise, Gross et al, combined df-DHM with off-axis-DHM for single hologram 3D-tracking of gold nanoparticles diffusing in water [75]. The use of df-DHM for semiconductor metrology is a relatively new topic that can potentially improve the metrology capabilities but that also offers some challenges that need to be addressed. A particular challenge of df-DHM using an oblique illumination beam is the impact of the coherence length of the light on the Field-of-View (FoV). In order to have sufficient intensity from a supercontinuum source with an AOTF we need a bandwidth of a few nanometers ($\cong$ 4

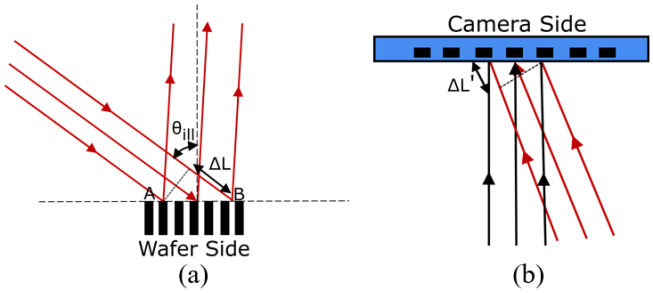

Figure 3.1: (a) Propagation of the illumination beam over a high angle θ_{ill} on the wafer. Here ΔL is the delay between the edges A & B of the wavefront. (b) The interference of the reference beam (red) with the image beam (black) on the detector. Here ΔL' is the delay between the edges of the diffracted wavefront.

nm) as stated earlier. However, this results in a relatively short coherence length that limits the FoV where fringes are visible. Only for specific reference angle, NA, magnification and source bandwidth parameter ranges, the fringes are resolved over a sufficiently large FoV. Since the information of the complex field is encoded in the measured fringe pattern, a more detailed understanding of the fringe contrast as a function of various sensor parameters is required since this will enable us to design a df-DHM system where the bandwidth of the light is optimized for sufficient intensity and sufficiently large FoV.

In this chapter, we analyze the impact of the coherence length of the light source on the FoV and we present a custom-built df-DHM that we used to verify our analysis. Finally, we present the first holographically obtained images of metrology targets that have been acquired with our df-DHM setup.

3.2 Dark-Field Digital Holographic Microscope

3.2.1 Temporal Coherence limitations

The use of the higher diffraction order creates a time delay between the edges of the illumination beam as depicted in Fig. 3.1(a). This time delay will propagate through the imaging system. At the camera the imaging beam is mixed with a reference beam where an additional time delay can be introduced as depicted in Fig. 3.1(b).

Fringes are only visible when the optical path length between the object and reference beam is within the temporal coherence length of the source. This effect means that fringe visibility is dependent on the location within the target image and on the temporal coherence length of the light source.

In the remainder of this section we will further quantify this relation between FoV and coherence length using a simple model that can be applied to both in-line and off-axis holography.

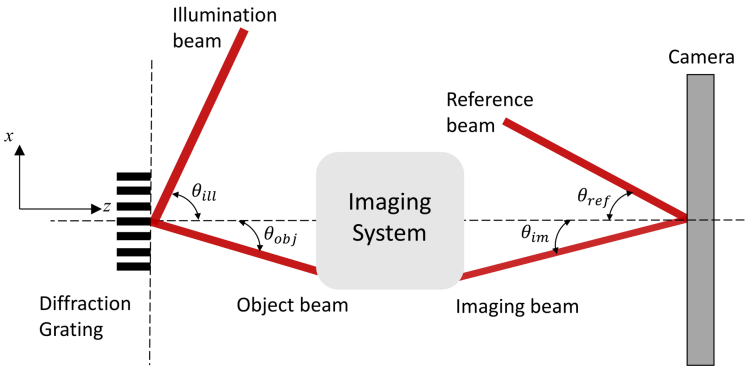

Figure 3.2: The theoretical model for df-DHM. We denote θ_{ill} as the illumination angle, θ_{obj} as the angle of the 1^{st} diffraction order captured by the imaging system, θ_{im} as the angle of the illumination beam after exiting the imaging system and θ_{ref} as the angle of the reference beam.

3.2.2 Theoretical Analysis

In this chapter, we will derive a simple analytical model of the relation between the coherence length (i.e. bandwidth) of the light source and the FoV of the image. To begin with, we define the basic principles of this model. For the sake of simplicity, we present only the 1D implementation where all the image-forming beams are in the x-z plane as shown in Fig. 3. An extension to a more general 2D model is quite straightforward and is presented in Appendix 3.A. We start with the well-known grating equation:

$$sin(\theta_n) = n\frac{\lambda}{P} + sin(\theta_{ill}), \tag{3.2}$$

where θ_{ill} is the illumination angle, λ is the wavelength, P is the grating pitch and θ_n is the angle of the nth diffraction order generated from the target. With the grating equation we can determine the NA of an objective lens that is needed to capture the 1^{st} order in an imaging system as shown in Fig. 3.2.

For simplicity, we will consider an ideal aplanatic imaging system as shown in Fig. 3.2 that obeys the following relation:

$$sin(\theta_{im}) = \frac{1}{M} sin(\theta_{obj}), \tag{3.3}$$

where θ_{obj} is the angle of the 1^{st} diffraction order, which is essentially θ_n with n equal to ± 1. M is the magnification of the imaging system.

In our analysis we consider simple plane wave propagation and we assume equal amplitudes of reference beam and object beam. The illumination beam has a complex amplitude at the grating plane of:

$$E_{ill}(x) = e^{i\frac{2\pi}{\lambda} sin(\theta_{ill})x}, \tag{3.4}$$

and using the sign convention of Ref. [102], we find for the object field:

$$E_{obj}(x) = e^{-i\frac{2\pi}{\lambda}sin(\theta_{obj})x}. \tag{3.5}$$

The image field and the reference fields at the camera plane are, respectively, given by:

$$E_{im}(x) = e^{-i\frac{2\pi}{\lambda}sin(\theta_{im})x}. \tag{3.6}$$

$$E_{ref}(x) = e^{i\frac{2\pi}{\lambda}sin(\theta_{ref})x}. \tag{3.7}$$

On these expressions, i indicates the imaginary unit. In holography the detected intensity is defined as:

$$I(x) = |E_{obj}(x) + E_{ref}(x)|^2 = |E_{obj}(x)|^2 + |E_{ref}(x)|^2 + E_{obj}(x)E^*_{ref}(x) + c.c. \tag{3.8}$$

where the product of the two fields (cross-terms) will give the interference of reference and object wave. From this interference we can define the spatial frequencies Δk difference of the k vectors. The wavenumber of the imaging wave on the detector is :

$$k_{im} = \frac{2\pi}{\lambda}sin(\theta_{im}), \tag{3.9}$$

which from Eq. (3.2) and (3.3) becomes:

$$k_{im} = \frac{1}{M}\left(n\frac{2\pi}{P} + \frac{2\pi sin(\theta_{im})}{\lambda}\right), \tag{3.10}$$

while the wavenumber of reference wave is :

$$k_{ref} = \frac{2\pi}{\lambda}sin(\theta_{ref}), \tag{3.11}$$

From the first cross term of Eq. (3.8) we reach to a sinusoidal interference pattern given by :

$$I(x) = 1 + cos[(k_{im} - k_{ref})x]. \tag{3.12}$$

Using the previously defined plane wave expressions for the illumination and reference beam and using the grating equation, Eq. (3.2) and the aplanatic imaging condition, Eq. (3.3) we find for the intensity on the camera:

$$I(x;\lambda) = 1 + cos\left(\frac{n}{M}\frac{2\pi}{P} + \frac{2\pi}{\lambda}\left(\frac{sin(\theta_{ill}}{M} - sin(\theta_{ref}\right)x\right). \tag{3.13}$$

In order to describe the finite coherence length of the light source, we have to extend the model to quasi-monochromatic illumination which we can easily do by writing the wavelength λ as center wavelength λ_c on which we add a small wavelength deviation $\Delta\lambda$. Eq. (3.13) then becomes:

$$I(x;\lambda_c,\Delta\lambda) = 1 + cos\left(2\pi\left(\frac{n}{M}\frac{1}{P} + \left(\frac{1}{\lambda_c} - \frac{\Delta\lambda}{{\lambda_c}^2}\right)\left(\frac{sin(\theta_{ill})}{M} - sin(\theta_{ref})\right)\right)x\right). \tag{3.14}$$

For the completeness of the analytical model we must integrate over the bandwidth (B) for various spectrum shapes. Here we consider the rectangular and the Gaussian case, where the bandwidth of the Gaussian beam is defined by the full width at half maximum (FWHM).

- The case of a rectangular spectrum yields an intensity of:

$$I(x;\lambda_c,B) = 1 + cos\left(2\pi\left(\frac{n}{M}\frac{1}{P} + \frac{1}{\lambda_c}S_\lambda\right)x\right)\text{sinc}\left(\pi\frac{B}{\lambda_c^2}S_\lambda x\right). \quad (3.15)$$

- For a Gaussian spectrum we find:

$$I(x;\lambda_c,B) = 1 + cos\left(2\pi\left(\frac{n}{M}\frac{1}{P}\right)x\right)\exp\left(-2\pi^2\frac{B^2{S_\lambda}^2x^2}{\lambda_c^4}\right). \quad (3.16)$$

So far, this analytical model is valid for both off-axis and in-line DHM. It can be seen that $S_\lambda = 0$, occurs when the direction of the reference beam coincides with the direction of the 0^{th} diffraction order in a bright-field setup. This is of course the case of an ideal imaging system where the FoV is independent of bandwidth.

In the two final expressions for the two different spectra, we focus on the fringe contrast of the detected intensity, which is a *sinc* function for a rectangular shape and a Gaussian for a Gaussian shape. From the fringe contrast in each case, Eq. (3.15), Eq. (3.16), we can draw some conclusions on the design requirements of a df-DHM setup.

In order to establish a relation between bandwidth and FoV from Eq. (3.15) and Eq. (3.16) we need to set a limit on the required fringe contrast. We selected a contrast limit of $2/\pi$ since for this value, the Field-of-View (FoV) of our analytical model is equal to the FoV of the simple path-length ray model that is shown in Fig. 3.1. This yields the following relation between FoV and bandwidth (B) for a rectangular spectrum:

$$B < \frac{1}{FoV}\frac{\lambda_c^2}{MS_\lambda}. \quad (3.17)$$

Expression (3.17) shows that the FoV depends on the bandwidth of the source and several parameters of the setup, like the magnification, the wavelength and the angle sensitivity S_λ. For an accurate prediction of the FoV for a given bandwidth B we need to know this sensitivity term S_λ. According to Eq. (3.15) we can determine the value of S_λ via the fringe period Λ. Starting from the definition of fringe period, Λ:

$$\Lambda = \frac{2\pi}{\Delta k}, \quad (3.18)$$

from Eq. (3.15) we know that the spatial frequency in the rectangular spectrum case is:

$$\Delta k = 2\pi\left(\frac{n}{M}\frac{1}{P} + \frac{1}{\lambda_c}S_\lambda\right), \quad (3.19)$$

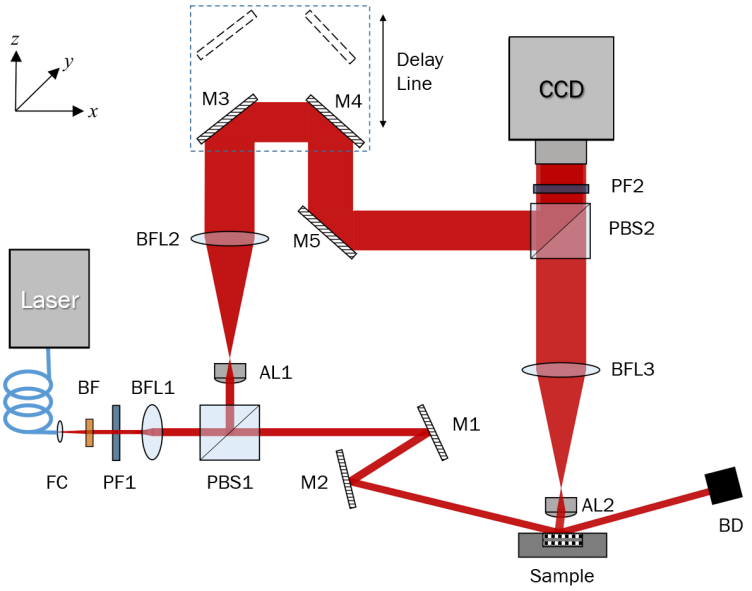

Figure 3.3: Schematic of dark-field digital holographic microscope (df-DHM). Two illumination beams are separated using polarizing beam splitter (PSB1) following a Mach-Zehnder interferometer configuration. The transmitted illumination beam hits the target with an oblique angle and generates the 1^{st} diffraction order (object beam) that is captured by the imaging system. The reflected illumination beam (reference beam) is recombined with the object beam with a second polarizing beam splitter (PBS2).

For $n = 1$ we reach to the following expression for the fringe period:

$$\Lambda = \frac{\lambda_c}{\left|\frac{\lambda_c}{MP} + S_\lambda\right|}, \tag{3.20}$$

With this simple model we can calculate the required values of the design parameters of a dark-field digital holographic microscope, that offers the FoV that is needed for metrology.

3.2.3 Experimental Setup

In this section we describe a dark-field digital holographic microscope (df-DHM), as shown in Figure 3.3 that was built to verify the theory presented in the previous section.

A fiber-coupled superluminescent diode (SUPERLUM cBLMD Light Source) was used as light source (LS) with a central wavelength of 785 $\pm$ 10 nm and 46 $\pm$ 5 nm bandwidth. To test the validation of the theoretical model, two additional bandpass filters (BF) of 5$\pm$1 nm and 10$\pm$2 nm FWHM bandwidths (Edmund Optics, Hard Coated with OD $\geq$ 4) were used with a center wavelength of 785

nm. The spectra used in the experiments are presented in the results section (Fig. 3.4). The light of the fiber was collimated using a 2 lens telescope, of a fiber coupler (FC Thorlabs F280APC-B) and a best form lens (BFL1 Thorlabs LA1908-B). By rotating the linear polarizer (PF1 Thorlabs LPVIS100-MP2) that is in front of a polarizing beamsplitter (PBS1 Thorlabs PBS252) we can tune the intensity ratio between the illumination and reference beams which allows us to minimize the acquisition time. The illumination beam is projected on the target at an angle of $\approx 70^{\circ}$ and a spot size of $\approx$1.2 mm. The $+1^{st}$ diffraction order generated from the grating was captured by a 4f imaging system and the 0^{th} order light that was reflected by the target was blocked by a beam dump (BD).

This imaging system contained two lenses, a plano-asphere as the objective lens with effective focal length of 8 mm and an NA of 0.5 (AL2- Thorlabs A240TM). With this NA according to Eq. (3.2) the setup of Fig. 3.3 is capable to detect targets with minimum pitch size of $\cong$ 550 nm. We choose a nominal magnification of 25x with the use of a best form lens (BFL3) with focal length of 200 mm and back focal length of 197.8 mm (Thorlabs LBF254-200-B). The CCD camera was a Vimba Prosilica GT2300 with 2336 x 1752 pixels and a pixel pitch of 5.5 µm.

The reference beam is incident on the CCD camera through a nominally identical 2-lens system (AL1 and BFL2), resulting in similar beam size with the object wave. In addition, the optical path length of the reference can be tuned with an adjustable delay line of two mirrors (M3, M4) which is needed for in-line phase-shifting holographic interferometry. The reference beam is recombined with the object beam using a second polarizing beam splitter (PBS2) that is placed on a high precision rotation stage. This rotation allows us to do in-line and off-axis holographic microscopy. Finally, by rotating the linear polarizer PF2 we can optimize the contrast of the fringe pattern on the camera. With this setup we are able to measure the intensity I_1 of the $+1^{st}$ diffraction order. However, according to Eq. (3.1) we also need to measure the -1^{st} diffraction order intensity for an overlay measurement. This could be done by rotating the wafer over 180° around its normal vector and measure I_{-1}.

However, a wafer rotation can cause a small lateral position shift of the gratings which impacts the contrast of the hologram according to Eq. (3.15) and (3.16) and thus also impacts the measured intensity. Our setup does not yet have this wafer rotation stage since we first wanted to experimentally verify our analysis on the impact of coherence length on FoV. Once we have experimental data to support our model we can use these result to select a rotation stage for actual overlay measurements.

3.2.4 Experimental Results

In this section, we present the experimental results that demonstrate the impact of coherence length on the Field-of-View and test the validity of the model that we presented in the previous section.

Firstly, we measured the spectrum of the light source with a spectrometer (Ocean Optics FX-series) with a spectral resolution of 1.5 nm. We took three different spectra, shown in Fig. 3.4, without any filter (black curve) and after

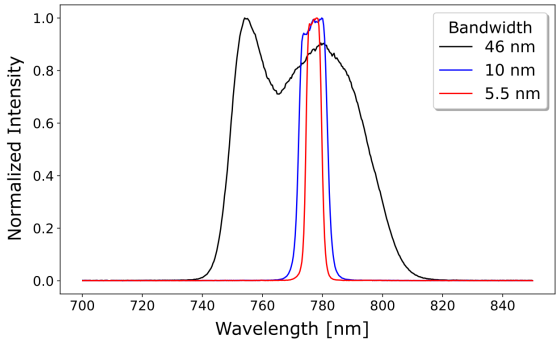

Figure 3.4: Spectrum used in the experiment. Black curve is the unfiltered spectrum of the SLD, blue curve is the 10 nm bandwidth filtered spectrum and red curve is the 5nm bandwidth filtered spectrum.

transmission through the narrowband interference filters (red and blue curves). All the spectra were within the range of what was expected, we can see that the unfiltered spectrum of the light source gave two peaks, one at 752 nm and one at 785 nm. For the other two measurements we slightly increase the exposure time and we obtain a 5.5 nm bandwidth (FWHM) for the 5 nm bandpass filter and a 10 nm FWHM for the 10 nm bandpass filter. Based on the resolution of the spectrometer that was used, we expect that our measurements should be within the margin of ± 1.5 nm of the measured data, and on our comparison with the theoretical results we take this tolerance into account.

In order to correctly determine the FoV at the target, we also need to know the magnification M. We measured M by using a silicon test wafer from ASML. This silicon substrate contained square gratings with dimensions of (58x58 μm^2) and etch depth of 90 nm. These square gratings have various pitches from 700 to 900 nm. From the measured image size of this target on the camera we obtained a magnification of 24.5 with an uncertainty of $\approx \pm 0.4$ which is based on 5 repeated measurements.

For this experiment, we acquired several holographic images of a large blazed grating with pitch (P) of 833 nm (Thorlabs GR25-1208) for 3 different bandwidths. For this pitch, a 785 nm wavelength and a 70° angle-of-incidence, the 1^{st} order is diffracted almost normal to the grating surface. The delay line (Fig. 3.3) was adjusted to ensure that the maxima of the observed fringe patterns were centered in the images. Fig. 3.5(a,b,c) shows the interference pattern located in the central part of the captured images. The fringes are oriented vertically and with a fringe period Λ of ≈ 6 µm. This fringe period is determined by the measured fringe period on the detector divided by the magnification. Fig. 3.5(d,e,f) shows the intensity averaged over the vertical direction. We used this measured fringe period to determine the value of S_λ using Eq. (3.21). We found the value of S_λ to be 0.033. The uncertainty in this value is estimated to be approximately 2%, and is mainly determined by the uncertainty in the wavelength (785 $\pm$ 10 nm) and the measured magnification (24.5 $\pm$ 0.4). From this measured S_λ we obtained a

reference angle of 5.2 mrad, with a similar amount of relative uncertainty. This reference angle indicates an in-line configuration.

The fringe contrast as function of location is extracted as follows. From the average curves we move to the Fourier space and select the cross-correlation terms and then with inverse Fourier space transform we obtained the orange curves of Fig. 3.5(g,h,i). The width of the area where the fringe contrast exceeds $2/\pi$ ($\approx$ 0.6) is around 30, 75 and 130 µm for 46, 10 and 5.5 nm bandwidths respectively. From the images of Fig. 3.5 we can also notice that for 5.5 and 10 nm bandpass filters we see a revival of the fringe visibility. For the 10 nm bandwidth we see a revival at $\pm$ 110 µm position on the wafer, while for the 5.5 nm bandwidth this revival begins at the edge of the FoV. Fringe contrast and spectral shape are connected via a Fourier Transform (FT) [103], so this revival is indeed expected for a rectangular spectrum (also seen in Eq. (3.15)). However, the spectrum of the 46 nm bandwidth is more smooth and given the properties of FT we do not expect to see a significant revival in fringe contrast.

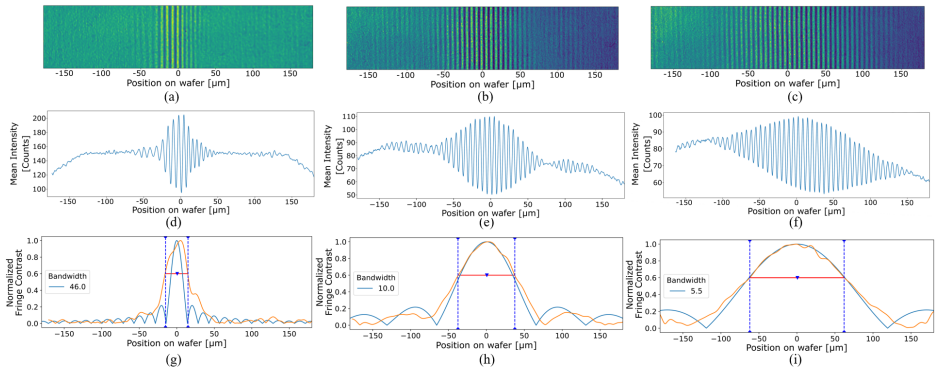

Figure 3.5: Measured fringe visibility (a, b, c) and period (d, e, f) of the interference patterns. Normalized fringe contrast (g, h, i) comparison with the theoretical fringe contrast (blue curves) and the measured fringe contrast (orange curves).

To validate our model, Figure 3.6 shows a plot of the FoV as a function of bandwidth according to Eq. (3.18) using the measured values of M and S_λ. In this figure we also added the three measured results that we obtained from the experiment with error bars that indicate the measurement uncertainty (Figure 3.5).

The final measurement that we did with this experimental setup was to obtain a complex image of overlay metrology targets on an ASML test wafer. Since speed is important for overlay metrology we decided to use single-shot off-axis df-DHM. We began with setting the delay line at a point where the fringe visibility is maximum at the center of the FoV, as previously shown with the blazed grating. Then we increased the angle of the reference beam to $\approx 2\,^\circ$ by rotating the angle of PBS2 which resulted in off-axis holographic images from which the complex image object field was determined.

Figure 3.7(a) is the obtained hologram for a 10 nm bandwidth, where the

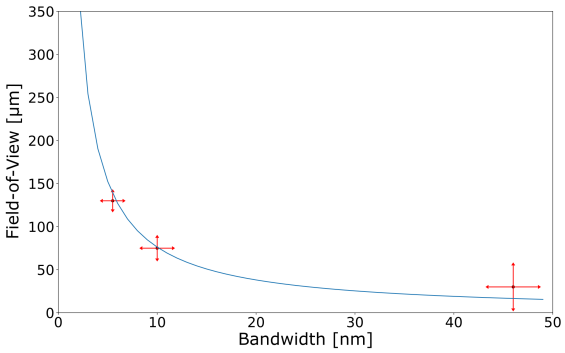

Figure 3.6: Theoretical curve of the expected FoV for selected bandwidth of light source. Blue curve is calculated for the measured reference angle of 5.2 mrad. Black dotted spots with error bars for the experimental results for 3 different bandwidths with red arrows presenting the uncertainties of the measurements.

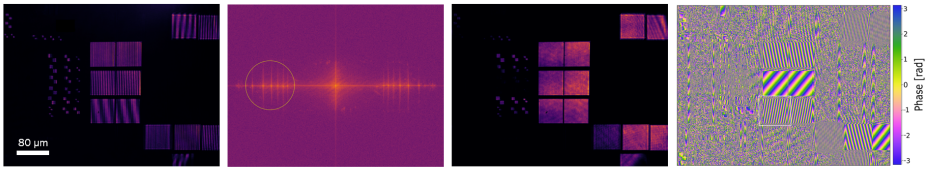

Figure 3.7: Off-Axis Digital holographic microscopy process for a semiconductor wafer. The bandwidth of the light source was set at 10 nm (FWHM). (a) hologram with interference pattern, (b) angular spectrum, with the cross-correlation term used for the reconstruction within the yellow circled area, (c) amplitude image; and (d) phase image.

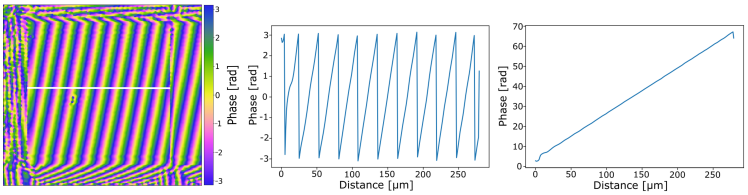

Figure 3.8: (a) Reconstructed phase for a selected square grating with pitch size of 900 nm. (b) Phase profile of Fig. 8(a) across the drawn white line, showing the 2π interference phase modulo and (c) the unwrapped interference phase of the selected target.

interference fringes are visible on the locations of the known targets. We chose the 10 nm bandwidth as it corresponds to a sufficiently large FoV and it provides higher intensity and therefore shorter acquisition times compared to the 5.5 nm bandwidth. For these targets we focused on the ones in the center which have pitches from top to bottom of 700, 800 and 900 nm respectively. Fig. 3.7(b) is the Fourier transform of the recorded hologram showing the zero-order which is the DC terms of the recorded intensity and the twin image peaks which are the two cross-correlation terms. From Fig. 3.7(b) we selected one of the twin image peaks as it contains the cross correlation information for image reconstruction. As shown, these cross correlation terms have different positions for different targets, but for this demonstration we selected a large enough region-of-interest (ROI) to reconstruct more targets. Figure 3.7(c) shows the intensity and Figure 3.7(d) shows the phase of the image reconstruction. The phase image represents a phase profile of the optical field reflected from the surface of the target. For targets with different pitches we expect different phase profiles.

To validate the phase image of Fig. 3.7(d), we have plotted the phase profile of one reconstructed target. Specifically, we have selected the bottom left target, that has a pitch size of 900 nm (as shown in Fig. 3.7(d)). On the observed phase image on Figure 3.8(a), the phase interference is not completely vertical, indicating that the reference beam is not perfectly aligned in the x-z plane but that it has a small spurious azimuthal angle which we can ignore since it has a negligible impact on our results. Figure 3.8(b) shows the measured phase profile of this target as shown on the drawn white line, where we can observe 2π phase jumps. After applying a phase-unwrapping algorithm to the data in Figure 3.8(b) we obtain the continuous phase variation.

3.2.5 Discussion

In order to compare the measured values for the Field-of-View with our theoretical derivation, we have to know the bandwidth of the spectrum, the magnification M, the illumination and reference angles. Here, we describe the procedure for determining these quantities from the measured data.

With respect to the magnification, we have used a target with known size and then through the pixel size of the detector, the determination of the magnification

is straightforward. Moreover, we also need to consider the uncertainties in the illumination and the reference angles.

The illumination angle was determined by observing the direction of the 1st order that was diffracted by the Thorlabs blazed grating. For the 785 nm illumination wavelength, the 1^{st} order passed through the center of the objective lens indicating that this 1^{st} order propagates normal to the grating surface. Using the grating equation, Eq. (3.2) we find an angle of incidence of $\approx 70°$. We also note from Eq. (3.17) that small errors in the illumination angle hardly impacts the uncertainty in S_λ.

The angle of the reference beam was determined by measuring the pitch Λ of the fringes on the camera. Using Eq. (3.21) we obtained a reference angle of 5.2 mrad for the images shown in Figure 3.5. This allows us to calculate the sensitivity parameter S_λ (Eq. (3.17)) which is needed for the calculation of the FoV as a function of bandwidth, given by Eq. (3.18).

The measured fringe contrast, as shown in Fig. 3.5, also shows that the width of the contrast curve increases for smaller bandwidth. The red dots shown in the graph of Fig. 3.6 proves this argument as the experimental results match with the theoretical curve.

For the theoretical curves of Figure 3.5(g,h,i) we have plotted the fringe contrast that we had derived from Eq. (3.15), Eq. (3.16). For the results we consider only the rectangular shape as it was the shape of the two bandpass filters. For the unfiltered spectrum, the shape is neither Gaussian nor rectangular shape so we have calculated the expected contrast curve numerically from the measured shape of the spectrum. The numerically calculated contrast curve looks similar to a sinc function.

For the first holographically obtained images of metrology targets we have increased the reference angle by rotating the PBS2. Our theory indicates that with off-axis holography for small angles of $\approx 2°$ of the reference beam, we have a larger FoV compared to in-line holography. With the off-axis measurements, the predicted FoV for the 10 nm bandpass filter is around 727 µm at the contrast limit of $2/\pi$ (using Eq. (3.18)) which is larger than the in-line case. Note that for a 2° reference beam angle, the cross-correlation terms are not completely separated from the DC term. For a complete separation of these terms in our setup the reference beam angle needs to be $\approx 3.4°$ but the resulting fringe density was too high for our camera that had an image sensor with a 5.5 µm pixel pitch. Fortunately, for this particular wafer sample there is almost no diffracted light at the edge of the NA so the resulting imaging artifacts are small.

Our experiments confirmed that the fringe contrast varies within the image according to Eq. (3.17). We now use this result to estimate the impact of contrast variations that may be introduced by a spurious translation after a 180° wafer rotation. The effect of a spurious translation means that the measured interference patterns for the acquisition of the $+1^{st}$ and -1^{st} order images will have slightly different contrast values of, respectively, $C + \Delta C$ and $C - \Delta C$. This will impact the measured intensities that we retrieve from the interferograms and

using Eq. (3.1) we find for the measured overlay OV_m:

$$\frac{(C+\Delta C)I_1-(C-\Delta C)I_{-1}}{(C+\Delta C)I_1+(C-\Delta C)I_{-1}} = K \times OV_m, \tag{3.21}$$

where $\Delta C(I_1 - I_{-1})$ tends to 0 and can be ignored from the denominator part, simplifying Eq. (5.1) as:

$$\frac{I_1-I_{-1}}{I_1+I_{-1}} + \frac{\Delta C}{C} = K \times OV_m. \tag{3.22}$$

Using this expression we find for the overlay error $\Delta OV = OV_m$ - OV:

$$\Delta OV = \frac{1}{K}\frac{\Delta C}{C}. \tag{3.23}$$

With todays overlay requirements the OV metrology errors must be less than ≈ 0.1 nm and assuming an overlay sensitivity K of 10^{-2} nm^{-1} we find that the relative contrast difference $\Delta C/C$ should be less than 10^{-3}. In order to deal with such a severe requirement, we need a good understanding of the mechanisms that result in a contrast variation across the image field. The results presented here are a first step towards dealing with this challenge.

3.2.6 Conclusion

This work presents a theoretical model of the impact of coherence length on the Field-of-View in a dark-field digital holographic microscope. This model has shown that the FoV is inversely proportional to the bandwidth of the light source.

With the presented model we can define requirements of design parameters that ensures that the setup offers sufficient FoV. These parameters are the wavelength and the bandwidth of the light source, the magnification and NA of the imaging system, as well as the specifications of the camera. These limiting factor will lead to the required bandwidth for a desired Field-of-View.

The experimental setup presented here, can be a novel addition to the future optical metrology tools. Our first demonstration presented a technique that can provide both phase-shifting and off-axis measurements, with off-axis able to reach single shot acquisition. This publication is a first step to build a df-DHM that should ultimately be able to offer fast and precise metrology on small metrology targets on semiconductor wafers. The next step in this investigation is to correct for small residual aberrations coming from the wavefront of the objective lens.

Appendix 3

3.A The 2D extension of the df-DHM model

Following the sign convention of Ref. [102], the grating equation describing the configuration of Fig. 3.2 takes the form of Eq. (3.2). This sign convention requires that $n > 0$. If the rays are diffracted to the left (the counterclockwise side) of the zeroth order ($n = 0$), then positive diffraction orders are generated, $n > 0$. If the diffracted ray runs rights of the zeroth order (the clockwise side), then negative diffraction orders ($n < 0$) are generated.

We will consider backward propagation as positive, meaning $\theta_i > 0$ always. All angles are taken positive with respect to the normal, counterclockwise. All the analysis was obtained by following the above sign convention.

For the simple plane-wave model, using Fig. 3.2 we define the reference wave as:

$$E_{ref}(\vec{r}) = A_r e^{j\frac{2\pi}{\lambda}\vec{n_r}\vec{r}}, \tag{3.24}$$

where A_r is the amplitude of the wave, λ is the wavelength, $\vec{r}$ is the position vector and $\vec{n_r}$ is a unit vector describing the direction of propagation of the reference wave and is given by:

$$\vec{n_r} = \begin{pmatrix} n_{xr} \\ n_{yr} \\ n_{zr} \end{pmatrix} = \begin{pmatrix} sin(\theta_r)cos(\phi_r) \\ sin(\theta_r)sin(\phi_r) \\ cos(\theta_r) \end{pmatrix}, \tag{3.25}$$

here θ_r is the angle of the reference wave with respect to the z-axis and ϕ_r is the azimuthal angle with respect to the x-axis. Following a similar notation for the object wave we have:

$$E_o(\vec{r}) = A_o e^{j\frac{2\pi L}{\lambda}} e^{j\frac{2\pi}{\lambda}\vec{n_o}\vec{r}}, \tag{3.26}$$

where

$$\vec{n_o} = \begin{pmatrix} n_{xo} \\ n_{yo} \\ n_{zo} \end{pmatrix} = \begin{pmatrix} sin(\theta_o)cos(\phi_o) \\ sin(\theta_o)sin(\phi_o) \\ cos(\theta_o) \end{pmatrix}, \tag{3.27}$$

For planar diffraction in (x,z) plane $sin(\phi_o) = 0$. For the description of the imaging system we use the expression:

$$sin(\theta_o) = \frac{F_1}{F_2} sin(\theta_1). \tag{3.28}$$

The intensity in the image plane for digital holography is:

$$\begin{aligned} I(x) &= |E_{obj}(x) + E_{ref}(x)|^2 \\ &= |E_{obj}(x)|^2 + |E_{ref}(x)|^2 + E_{obj}(x)E^*_{ref}(x) + E_{ref}(x)E^*_{obj}(x). \end{aligned} \tag{3.29}$$

Expanding this expression with the model description that we follow yields:

$$I(x) = A_o^2 + A_r^2 + 2A_oA_rcos\left(\frac{2\pi}{\lambda}(L + (\vec{n_o} - \vec{n_r})\vec{r})\right), \tag{3.30}$$

where $2\pi L/\lambda$ is a path length difference between reference and object beam at (0,0,0).

We normally consider the intensity in the (x, y)-plane where the camera is located so we split the unit vectors in an in-plane (parallel) unit vector and a perpendicular (senkrecht) unit vector :

$$\vec{n} = sin(\theta_o)\vec{p} + cos(\theta_o)\vec{s}. \tag{3.31}$$

Likewise, the position vector is also decomposed in the z-component $\vec{r_s}$ and an in-plane (x, y) position $\vec{r_p}$. The following drawings illustrate the two vectors, Fig. 3.9.

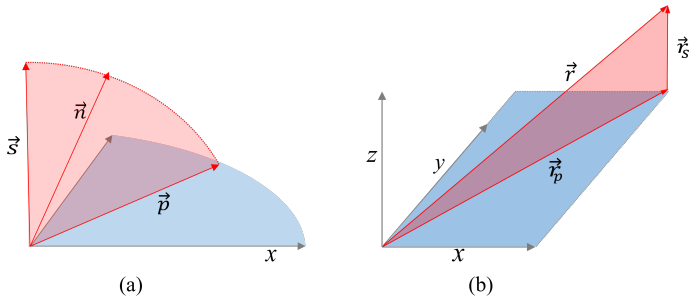

Figure 3.9: (a) the unit vector direction of Eq. (3.32), (b) the position vector direction.

The intensity in the image plane of Eq. (3.31) will take the form:

$$I(\vec{r_p}) = A_o^2 + A_r^2 + 2A_oA_rcos\left(\frac{2\pi}{\lambda}(L + ((sin(\theta_o)\vec{p_o} - sin(\theta_r)\vec{p_r})\vec{r_p})\right), \tag{3.32}$$

The in-plane propagation of the nth diffraction order is given by the grating vector equation. This expression includes Eq. (3.2) which is the case of conical diffraction by a 1D-periodic grating:

$$sin(\theta_n)\vec{p_n} = n\frac{\lambda}{P}\vec{p_G} + sin(\theta_{ill})\vec{p_{ill}}, \tag{3.33}$$

with the use of the sine-rule for imaging:

$$sin(\theta_o)\vec{p_o} = \frac{1}{M}sin(\theta_n)\vec{p_n}, \tag{3.34}$$

we now define a sensitivity vector $\vec{S_p}$, similar to the angle sensitivity parameter

of Eq. (3.17) to keep the expression of the detected intensity manageable:

$$\vec{S_p} = \frac{sin(\theta_{ill})}{M}\vec{p_{ill}} - sin(\theta_r)\vec{p_r}, \tag{3.35}$$

with the use of Eq. (3.35) and Eq. (3.36) , the vectorized notation yields the following expression of the detected intensity:

$$I(\vec{r_p}) = A_o^2 + A_r^2 + 2A_oA_rcos\left(\frac{2\pi}{\lambda}(L - \vec{S_p}\cdot\vec{r_p}) + \frac{2n\pi}{MP}\vec{p_G}\cdot\vec{r_p})\right), \tag{3.36}$$

this expression is valid for monochromatic light with infinite coherence length. Quasi-monochromatic light contains a range of wavelengths centered around a center wavelength λ_c. For small wavelength deviations $\Delta\lambda$ away from the central wavelengths we can use the following approximation for the wavelength λ:

$$\frac{1}{\lambda} = \frac{1}{\lambda_c + \Delta\lambda} \approx \frac{1}{\lambda_c} - \frac{\Delta\lambda}{{\lambda_c}^2}, \tag{3.37}$$

this yields for the detected interference pattern:

$$I(\vec{r_p}) = A_o^2 + A_r^2 + 2A_oA_rcos\left(2\pi\left(\frac{1}{\lambda_c} - \frac{\Delta\lambda}{{\lambda_c}^2}\right)(L - \vec{S_p}\cdot\vec{r_p}) + \frac{2n\pi}{MP}\vec{p_G}\cdot\vec{r_p})\right), \tag{3.38}$$

The total intensity is now obtained by integrating over the wavelength range (bandwidth) for the spectrum shape of the light source. For simplicity, for the rectangular case this integration runs from $B/2$ to $+B/2$ where B is sufficiently large to cover all the light in the spectrum:

$$I_T(\vec{r};\lambda_c,B) = \frac{1}{B}\int_{-B/2}^{B/2} I(\vec{r};\lambda_c,\Delta\lambda)d\Delta\lambda. \tag{3.39}$$

For a symmetric spectrum (which is generally sufficiently true) we can write for the integral:

$$I(\vec{r}) = A_o^2 + A_r^2 + 2A_oA_r\gamma(\vec{r_p};\lambda_c,B)cos\left(2\pi\left(\frac{1}{\lambda_c}\right)(L - \vec{S_p}\vec{r_p}) + \frac{2n\pi}{MP}\vec{p_G}\cdot\vec{r_p}))\right), \tag{3.40}$$

here γ is a coherence term that describes the local image contrast at position $\vec{r_p}$. In order not to further complicate the analysis we assume a simple rectangular spectrum with full bandwidth B:

$$\gamma(\vec{r_p};\lambda_c,B) = \frac{1}{B}\int_{-B/2}^{B/2} cos\left(2\pi\left(\frac{\Delta\lambda}{{\lambda_c}^2}\right)(L - \vec{S_p}\cdot\vec{r_p})\right)d\Delta\lambda, \tag{3.41}$$

evaluating this integral yields:

$$\gamma(\vec{r_p};\lambda_c,B) = sinc\left(\pi\left(\frac{B}{\lambda_c^2}\right)(L-\vec{S_p}\cdot\vec{r_p})\right). \tag{3.42}$$

For the simplicity of this analysis we have considered planar diffraction in (x,z) where $sin(\phi_o)=0$. In reality this needs to be included and can be easily added on the vectorial derivation of $\vec{S_p}$ for $\vec{r_p}=x\vec{n_x}+y\vec{n_y}$. Now $\vec{r_p}$ is a vector that denotes a position (x,y) on the camera image and $\vec{S_p}$ is modified as:

$$\vec{S_p} = \frac{1}{M}((\sin\theta_{ill} - M\sin\theta_{ref}\cos\phi_{ref})\vec{n_x} - (M\sin\theta_{ref}\sin\phi_{ref})\vec{n_y}), \tag{3.43}$$

where ϕ_{ref} is the azimuthal angle of the reference. For convenience we now convert all parameters to wafer level by adding the magnification of the setup, M, and we introduce to following notation: $x_w,y_w=\frac{x,y}{M}$, $\sin\theta_{ill}=NA_{ill}$, $NA_{ref} = M\sin\theta_{ref}$. So NA_{ref} is essentially the sine of the reference angle as seen from the wafer side. This yields a compact expression for the coherence γ in the image:

$$\gamma(x_w,y_w) = sinc\left(\pi\frac{B}{\lambda_c^2}(L - x_w(NA_{ill} - NA_{ref}\cos\phi_{ref}) - y_w NA_{ref}\sin\phi_{ref})\right). \tag{3.44}$$

Figure 3.10 presents the coherence of the image as derived on Eq. (3.46) where the direction is given by the tangent of the two coordinates:

$$\tan\beta = \frac{\sin\phi_{ref}}{\frac{NA_{ill}}{NA_{ref}} - \cos\phi_{ref}}, \tag{3.45}$$

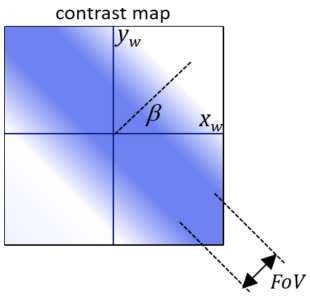

Figure 3.10: Schematic drawing of the contrast direction for an azimuthal angle of 135°.

To derive an expression for the FoV, we consider a contrast limit of $2/\pi$. For the case of L=0, the maximum of the coherence is in the center of the image and the FoV, with a sinc function that depends only on the sensitivity term. In the 2D case this term is defined by the direction of the parallel unit vectors and the

position vectors of the two beams. The FoV can be shown to be given by:

$$FoV = \frac{\lambda_c^2}{B} \frac{1}{\sqrt{NA_{ill}^2 + NA_{ref}^2 - 2NA_{ill}NA_{ref}cos\phi_{ref}}} \tag{3.46}$$

We can use this equation to determine the expected FoV of our setup. For instance, with $\phi = 0°$ we expect a FoV of 75 µm while if we increase the azimuthal angle to $\phi = 45°$ the expected FoV decreases to 50 µm. We need to denote that expression (3.18) is the bandwidth for the rectangular shape with the original expression:

$$B < \frac{\lambda_c^2}{2x} \frac{1}{S_\lambda}, \tag{3.47}$$

where 2x is equal to the FoV, leading to the full expression of Eq. (3.18):

$$B < \frac{\lambda_c^2}{FoV'} \frac{1}{S_\lambda} = \frac{\lambda_c^2}{MFoV} \frac{1}{S_\lambda} = \frac{\lambda_c^2}{FoV} \frac{1}{sin(\theta_{ill} - M\theta_{ref})}. \tag{3.48}$$

3.B Experimental Validation of the 2D extension

In this Appendix we compare signal variations of experimental data with the theoretical expectations to confirm the impact of coherence in the setup. For this comparison we use a sample that consists of larger gratings in order to make the effect better visible. These targets have large pitch sizes (900-1200 nm) and for that reason we use a 635 nm wavelength. A longer wavelength according to the specifications of the used AOTF resulted in a bandwidth B of about 7 nm which limits the FoV according to our analysis.

Figure 3.11 shows the reconstructed images of these targets for both diffraction orders along with a comparison of the measured and predicted values of the field of view and the direction β of "constant coherence" lines.

Fig. 3.11(a) and 3.11(c) represents the reconstructed amplitudes of -1st and +1st order respectively, where the signal variation between the two is visible as expected from the analysis in section 3.A. It can be seen that the coherence variations γ between object and reference beams are tilted in a different orientation between the two signals due to the different azimuthal angle of the two reference beams. For instance, for $\phi = 0°$ we expect that the orientation of the fringes would be parallel to the y-axis of the detector. In order to measure the contrast direction, β, we measure the angle difference of the brightest line of FoV from the positive x-axis (as shown of Fig. 3.11(c)). For the -1st order the contrast direction was 106.9° while for the +1st order it was 70.03°.

We determine the FoV from the measured images by fitting a quadratic profile to the signal variation inside the grating along the y-direction and determining the width W at which the signal level has reduced to 60% of its maximum value. This was done for all pixel columns along the x-direction which allowed us to obtain an average value of W and an estimate of the standard deviation of W. In order to come to the FoV from the measured width W we need to take the orientation

of the coherence function into which is done by multiplying the measured W by $\sin(\beta)$. The measured FoV for the two diffraction orders was found to be 61.69 µm for the -1st order and 45.98 µm for the +1st order. The standard deviation of the measured width was measured to be 5 µm.

The location of the side-bands in Fig. 3.11(b) allow us to determine the tilt angles of the 2 reference beams. Inserting the sine of these angles in Eq. (3.47) and Eq. (3.48) and using the central wavelength of 635 nm and a bandwidth B of 7 nm yields an expected FoV and and expected orientation angle β of the signal level as a function of the azimuthal angle of the reference beams. These expected values for the FoV and β as function of azimuthal angle are shown in, respectively, Fig. 3.11(d) and 3.11(e). Here the blue curve denotes the -1st order image and the red curve denotes the +1st order image. The blue and red dots in these figures indicate the measured values that we obtained from the images in Fig. 3.11(a).

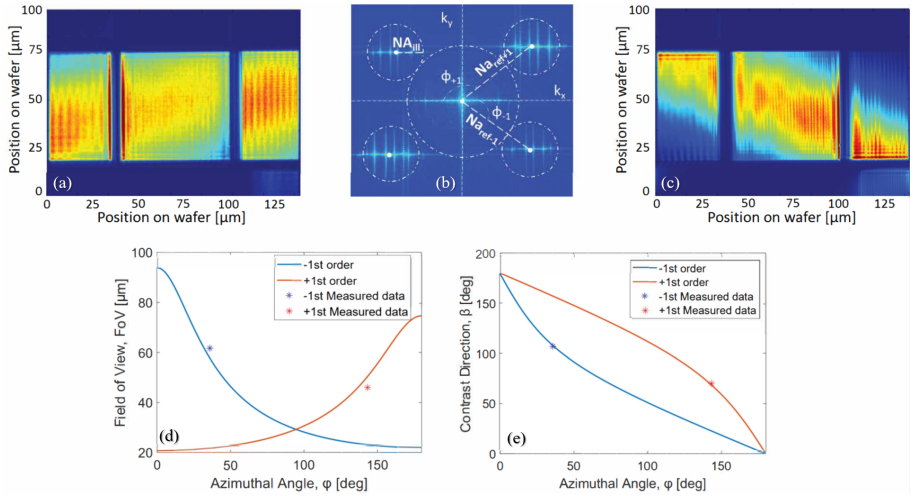

Figure 3.11: Impact of coherence length. (a), (c) Reconstructed amplitudes of -1st and +1st order respectively. (b) the angular spectrum of the signal. (d) the expected FoV against the azimuthal angle and (e), the contrast direction against the azimuthal angle, with the addition of the two measured values of figures (a) and (c).

Both plots of Fig. 3.11(d) and 3.11(c) show a good match between measured and expected data. On Fig. 3.11(d) we see a small deviation of $\approx$ 4 µm on the FoV and on Fig. 3.11(e) a small deviation of $\approx 1°$ on contrast direction. This deviation is small and can be attributed to the difference between the actual spectrum shape and the model's rectangular shape, and the noise level during the measurement.

From the experiments shown above, we find that the FoV is mainly limited by the coherence length of the source. As such FoV can be increased significantly by reducing the bandwidth of the source. Also, the required FoV for OV metrology is continuously shrinking as the size of the target gratings is continuously shrinking.

Chapter 4

Diffraction-based overlay metrology from visible to infrared wavelengths using a single sensor

Thus far, overlay measurements have been limited to visible wavelengths, but the use of materials that are opaque to visible wavelengths necessitates measurements using infrared light. In this chapter we demonstrate that an overlay sensor based on digital holographic microscopy can perform such overlay measurement at infrared wavelengths, while maintaining functionality at visible wavelengths. This was done by constructing a breadboard setup that is capable of measuring overlay at wavelengths ranging from 400 to 1100 nm, with the possibility to extend to 1600 nm. Using the setup we demonstrated good linearity between an applied amount of overlay and the measured amount. In addition, we demonstrated that the setup is only sensitive to structures at the top of the wafer. Measurements are therefore unaffected by the fact that Si is transparent at 1100 nm. These results demonstrate the viability of an overlay sensor that is sensitive to visible and infrared light, allowing more freedom in choice of materials for integrated circuits.

The content of this chapter has been published in: Theodorus T. M. van Schaijk, Christos Messinis, Nitesh Pandey, Armand Koolen, Stefan Witte, Johannes F. de Boer, and Arie den Boef, *Diffraction-based overlay metrology from visible to infrared wavelengths using a single sensor,* J. of Micro/Nanopattern. Mater. Metrol. **21**(1): 014001 (14 Feb 2022).

4.1 Introduction

Over the years, optical overlay metrology has seen significant innovations that were needed to keep up with the demanding overlay requirements of the semiconductor industry. For many years, image-based overlay metrology using box-in-box metrology targets has been the work horse on essentially all layers [10]. A big improvement in metrology precision and robustness came with the introduction of advanced imaging metrology targets where the box structures were replaced by gratings.

Another big step forward was the introduction of (micro) diffraction-based overlay metrollogy (µDBO) where an overlay target consists of overlapping grating-pairs [9, 15, 104]. These overlapping gratings are optically coupled, and as a result of this coupling, a small shift between the gratings (overlay) creates a small but measurable intensity variation in the diffracted light. The use of multiple grating-pairs with different intentional overlay bias in an overlay target allows an accurate determination of overlay from the measured diffracted intensities [3]. An evolution of the µDBO targets that is much less sensitive to stack variations was proposed previously [105]. The use of multiple wavelengths in µDBO has significantly improved process-robustness and allowed accuracy levels in the sub-nanometer range even in the presence of process variations [16, 70, 71]. As a result, metrology using µDBO-marks has become the standard for many overlay-critical layers in logic and memory devices.

However, in addition to improving precision, accuracy, and robustness, overlay metrology tools must also deal with decreasing signal levels. Several materials that are regularly used in semiconductor device manufacturing, such as amorphous carbon, are highly absorbing at visible wavelengths, resulting in a loss of overlay signal. Solutions such as topography-transfer and mark clear-out are sometimes used to still detect a signal from an overlay target that is buried underneath an absorbing layer. However, topography transfer is not always robust, and it can also introduce additional overlay metrology errors. Mark clear-out is also not preferred since it involves additional processing steps that increase cost.

A more preferred approach would be the use of (near) infrared wavelengths since many materials like silicon and amorphous carbon tend to become more transparent towards longer wavelengths. However, enlarging the wavelength range of optical overlay metrology tools is far from trivial since these tools contain many high-quality lenses that need anti-reflection (AR) coatings to minimize light losses and ghosting effects. The wavelength range of these AR coatings is usually limited to about one octave which prevents a significant extension of the wavelength range of an optical metrology tool. Moreover, one would also need an image sensor that covers the visible to the infrared wavelength range and that also offers a high quantum efficiency and low read noise levels. Despite the impressive progress in image sensor technology there is still a significant challenge to reach the low read noise levels in the infrared wavelength range.

One could consider using dedicated overly metrology tools for visible-only and infrared-only. From a technical perspective this is possible but this will significantly raise the cost-of-metrology. Moreover, this is also not attractive in terms

of ease-of-use. Ideally, one would like to have an overlay metrology tool that covers the full wavelength range from visible to infrared in a single sensor with the performance and cost level of existing tools.

In this chapter we present dark-field digital holographic microscopy (df-DHM) that offers a wavelength range of 400 to 1100 nm and uses only one uncoated lens for imaging an overlay target on an image sensor. The aberrations of this single lens can be computationally corrected using established back-propagation algorithms [106]. The df-DHM concept has been previously described in Ch. 2 and Ch. 3 and here we extend this concept with a camera sensor that offers a large wavelength range with high quantum efficiency but with somewhat elevated read noise levels [107] (Sony IMX990). However, the coherent detection in df-DHM raises even weak metrology signals well above the noise levels of this image sensor.

It should be noted that sythetic extensions of the wavelength range are possible using DHM [108]. In such a system, a digital hologram is illuminated using two beams, each at a different wavelength. Each of these beams provides phase information about the object modulus its wavelength. By combining the phase information from both beams it is then possible to define a synthetic beat wavelength as $\Lambda = (\lambda_1\lambda_2)/(\lambda_2 - \lambda_1)$, where λ_1 and λ_2 are the wavelengths of the two beams, respectively. While such a solution provides an excellent extension of the wavelength range when the object responds similarly to each individual wavelength, it's use is limited when the object response depends on the wavelength. For example, amorphous silicon has an absorption coefficient of 17184 cm^{-1} at a wavelength of 800 nm, but is almost completely transparent at 1600 nm [109]. This means that any object that is buried beneath a layer of amorphous silicon yields a weak signal at visible wavelengths, and thus does not allow to synthetically extend this wavelength. In the infrared, it is quite possible to image through the layer of amorphous silicon demonstrating the benefit of using longer wavelengths.

In the next section we first briefly summarize our df-DHM concept followed by a description of the breadboard setup. We then present the first proof-of-concept data to demonstrate the potential overlay metrology capabilities of our df-DHM concept. We end the chapter by identifying the major effects that are currently limiting performance and by proposing methods of solving these limitations.

4.2 UV-Vis dark-field DHM

We propose to measure OV of µDBO gratings using a dark-field digital holographic microscope. Our df-DHM microscope has already been extensively reported previously in Chapter 2 (and ref.[110]) and is schematically shown in Fig. 4.1. The wafer is illuminated at an angle of 70° relative to the wafer normal using a polarized, collimated and coherent beam of light. The dark-field is subsequently imaged onto a camera which is located above the wafer using a single imaging lens. Here, an off-axis hologram is created due to the coherent interference with a tilted reference beam. From this hologram, the complex electric field of the

light at the camera plane can be recovered computationally as was described in Ch. 2.2.

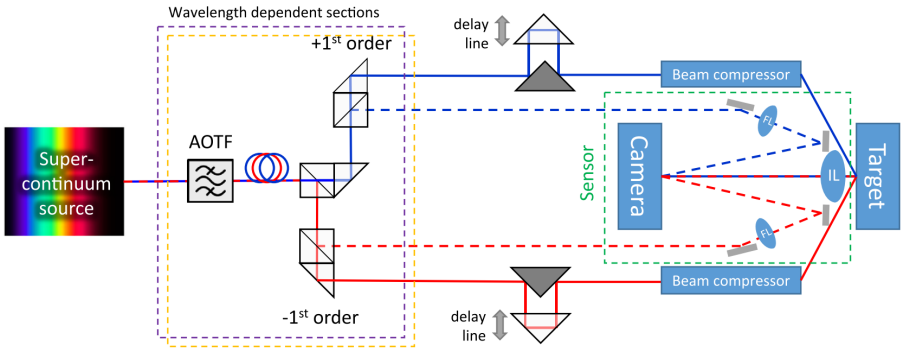

Figure 4.1: Schematic representation of df-DHM setup consisting of the actual sensor (highlighted in green) and the illuminator (rest of the setup). Light is generated using a supercontinuum source, filtered by an AOTF and split into four branches. The blue and red lines indicate the beam path of the beams corresponding to the $+1^{st}$ and 1^{st} diffraction orders, respectively. The solid lines indicated the illumination beams, while the dashed lines indicate the reference beams. A dark-field image is created using the imaging lens (IL). Finally, the reference beams are focussed next to the IL by a focussing lens (FL) such that the beam on the camera is diverging. The setup contains two AOTFs and two beam splitting sections as indicated in the figure by the dashed rectangle. Currently, switching between the two wavelength ranges is performed using flip-mirrors, but these can be easily replaced by dichroic mirrors.

Since the complex electric field fully describes a polarized beam of light, the collected hologram can be used to computationally back-propagate the light, e.g. to the pupil plane. When the object is a point scatterer, the phase profile that is obtained in this plane is a good representation of the aberrations of the imaging lens. It is therefore possible to correct for the lens aberrations, e.g. by subtracting the phase profile that was measured for a point scatterer (the reference) from the profile that was measured for an overlay target. This technique is explained in detail in one of our papers [106] and will be presented in the Ch. 5. As shown in this paper, excellent imaging performance can be achieved using this method even using a severely aberrated optic. Since the lens does not have to be well-corrected for aberrations a simple, single lens element can be used. This limits the number of airglass interfaces and results in low reflection losses even without anti-reflective coatings. This eliminates the main reason for the limited wavelength range of most optics, and therefore the simple imaging lens can operate over a very wide wavelength range.

One other feature of our df-DHM concept is the parallel acquisition of the $+1^{\text{st}}$ and -1^{st} order dark-field images of the µDBO overlay targets Ch. 3.As a result of this unique feature of DHM, we can use the full numerical aperture (NA) of the imaging lens which helps to improve the spatial resolution which is beneficial for small metrology targets. Moreover, a large imaging NA also offers a larger

wavelength range over which a metrology target can be measured.

4.3 Experimental setup

The experimental setup consists of two parts: an illuminator that generates and conditions the two illumination- and reference beams, and a sensor that collects the actual holograms. Both are schematically shown in Fig. 4.1 and a photograph of the setup is shown in Fig. 4.2. Coherent light is generated using a supercontinuum laser spanning a bandwidth of 410 to 2400 nm (Leukos Rock 400 5). Subsequently, the light is spectrally filtered using two acousto-opti tunable filters (AOTF) (Leukos Tango Dual VIS-NIR1). These AOTFs cover wavelength ranges of 400 to 650 nm and 640 to 1100 nm, respectively. Each of the AOTFs is fiber coupled to an endlessly single mode photonic crystal fiber and the output of each of these fibers is collimated using an off-axis parabolic mirror (OAPM) that operates over a very wide wavelength range (Thorlabs MPD01M9-P01). Next, the three beams are split into four beams using a set of beam splitter cubes optimized for each respective wavelength range with a $45\% - 45\% - 5\% - 5\%$ splitting ratio. A number of flip-mirrors then allows to select between the three operating ranges. It should be noted that this beam combining can also be done using dichroic mirrors to eliminate this mechanical step. Finally, the two illumination beams each pass through a separate optical delay line matching the optical path length of the illumination beam to its corresponding reference beam to well within the coherence length of the light source, ensuring interference at the camera plane. The resulting four beams propagate to the sensor.

This sensor was already described in some detail in the previous section. The illumination beams pass through a beam compressor consisting of two OAPM, allowing for a wide wavelength range. As a sample, we typically use a simple test wafer containing multiple µDBO grating pairs as shown in Fig. 4.3. The dark field is imaged using a custom-made CaF_2, biaspheric lens with a focal length of 4.283 mm and an NA of 0.5. This lens was optimized for a magnification of 50× and a wavelength of 400 nm, which minimizes the total aberrations over a bandwidth of 400 to 1100 nm.

The reference beams pass through a focusing lens. This lens focusses the beam onto a mirror adjacent to object beam and this serves two purposes. Firstly, the center of the focussed spot can be closer to the object beam than that of a large beam. This significantly reduces the angle between the object and reference beams and therefore the fringe frequency on the camera and the requirement on the pixel pitch. Secondly, the imaging system is non-telecentric and shows a spherical wavefront at the camera. By matching the radius of curvature of the reference beam to that of the object beam, recovery from the hologram improves. In our current setup we use free-space coupling to project illumination beams on the wafer and the reference beams on the camera. However, we have shown previously that we can also use fiber coupling which we will implement as one of the next steps in this investigation.

Finally, the beams interfere at the camera (Aval ABA-013VIR-GE, Sony

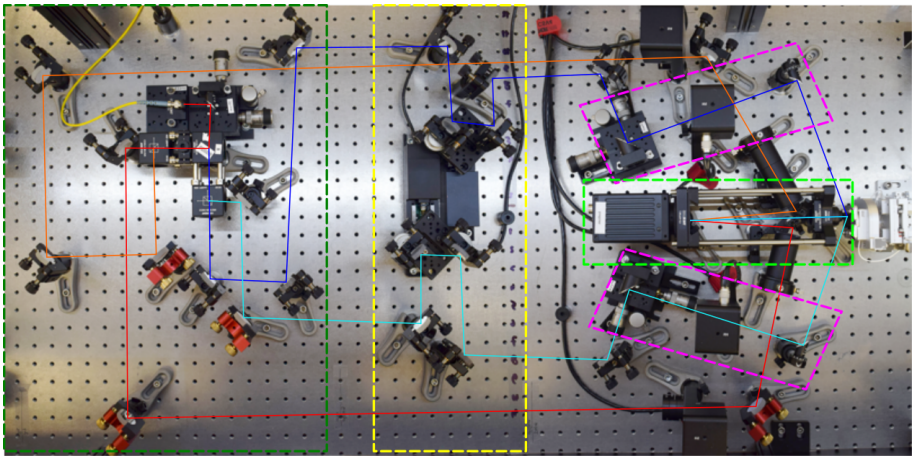

Figure 4.2: Photograph of the experimental setup. Not included in the photo are the fiber-coupled supercontinuum source, the AOTFs and the beamsplitting cubes for the near-infrared wavelengths. Visible light arrives from the AOTF through the yellow fiber in the top left and is collimated using an OAPM. Then, a set of beam splitting cubes splits the beam into four, indicated in red, orange, blue, and cyan. After the splitting section (dashed dark green box), two delay lines ensure path length matching (yellow box). Subsequently, two beam compressors consisting of OAPMs reduce the beam size of the illumination beams (magenta boxes). Finally, the dark field of the overlay targets is imaged onto a camera in the actual sensor (light green box). The photo is mirrored in the horizontal direction to match the schematic in Fig. 4.1.

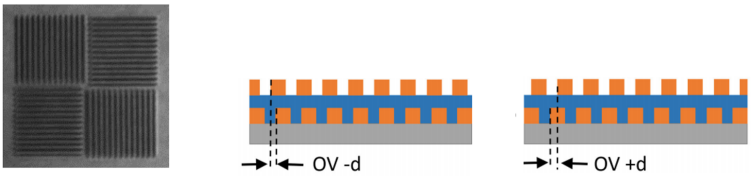

(a) Bright-field image of a µDBO-target.

(b) Schematic cross section of a negatively biased target.

(c) Schematic cross section of a positively biased target.

Figure 4.3: (a) A µDBO-target consists of four grating pairs. Two of these grating pairs run in the vertical direction and are used to measure overlay in the horizontal direction, the other two grating pairs are used to measure overlay in the vertical direction and are not used in this work. (b), (c) A cross-section of the two vertical grating pairs. As can be seen, each of the grating pairs has an intentional offset in the overlay of d = 20 nm. By measuring both gratings pairs, the measurement can be made independent of the stack in between the top and bottom gratings.

IMX990 sensor). This camera has a relatively uniform quantum efficiency ranging from 400 to 1600 nm. This is achieved by thinning down the InP substrate of a backside-illuminated InGaAs camera sensor. In addition, this sensor features a pixel pitch of 5 µm, which is achieved by replacing the typical In-bump that connect the photosensitive die to the readout electronics by Cu-Cu bonds. Both

features have been industrialized relatively recently and play a crucial role in enabling holography from the visible to infrared using a single sensor.

4.3.1 Signal processing

After capturing the hologram on the camera, all processing is done computationally. These steps were explained in great detail before in Ch. 2, and will be covered more briefly in this section. All images in this section were obtained at a wavelength of 520 nm. For each additional wavelength of interest, we repeat the entire procedure.

As an input to the algorithm, two images are required: a hologram of the target and a hologram of a reference grating which allows to calibrate the beam profile of the illumination beam. This reference grating would normally be on a fiducial, but for this first experiment we used a resist-only grating that was present on our wafer sample. The signal flow is schematically illustrated in Fig. 4.4. Each of these holograms is first converted to the spatial frequency domain using a Fourier transform (FFT), resulting in images such as Fig. 4.4(c). Subsequently, the two sidebands are computationally filtered and shifted to the baseband.

Then, an inverse FFT (iFFT) is performed to obtain the two dark field images corresponding to the two diffraction orders, which are shown in Fig. 4.4(b) and 4.4(d). In these images we can then define a region of interest for each of the biased gratings and integrate the power in each of these gratings. This yields four values for the target hologram and four values for the reference hologram. To make the system less susceptible to inhomogeneities in the illumination beam, the target values are divided by their corresponding reference value. Finally, the asymmetry in the diffraction pattern is calculated and the OV is calculated from these asymmetries as is typically done for µDBO-targets.

4.4 Experimental Results

4.4.1 Wide wavelength range operation

To demonstrate the wide wavelength range of operation for the sensor, we show images of µDBO targets ranging from 500 to 1100 nm in Fig. 4.5. As shown in Fig. 4.5(a), the sensor captures multiple diffraction orders at shorter wavelengths. At longer wavelengths, the diffraction orders pass through the edge of the NA and more and more aberrations start to become more apparent. This is especially apparent in Fig. 4.5(e). Such aberrations can be corrected using the procedure outlined in Ref. 10, but this is outside the scope of this paper.

4.4.2 Overlay measurements

To demonstrate the wide bandwidth of operation further, we used this setup to measure the OV of a range of µDBO targets with a programmed overlay of 20, 10, 0, 10, and 20 nm. The resulting measured overlay values are shown for each programmed overlay value in Fig. 4.6(a) and Fig. 4.6(b) for a wavelength of

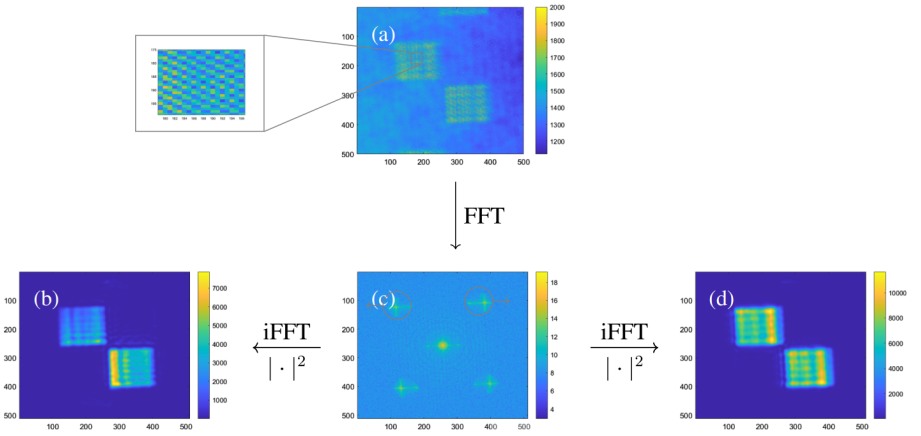

Figure 4.4: Signal flow for the reconstruction. (a) The raw camera image and the zoomed image clearly shows that the fringes of the hologram are resolved. After performing an FFT, it is clear that the signal is split into a baseband and four sidebands in (c). The baseband is not of interest to us, but the sidebands contain the complex electric field of the -1^{st} and +1^{st} diffraction orders. Each sideband is separately filtered using the window shown, shifted to the baseband, and converted back to image space using an iFFT. Finally, the absolute squared value is taken to obtain an image similar to a regular dark-field image, but with the advantage that both diffraction orders can be measured simultaneously and that the phase-image is also retrieved. The resulting image for the -1^{st} and +1^{st} diffraction orders are shown in (b) and (d), respectively.

(a) 500 nm (b) 650 nm (c) 800 nm (d) 950 nm (e) 1100 nm

Figure 4.5: Demonstration of the wide wavelength range over which the sensor can operate. Each of the images shows a 900-nm-pitch µDBO-target measured at the indicated wavelength. Each of the gratings is 8 x 8 µm^2.

520 nm and 1100 nm, respectively. These wavelengths were also chosen because they clearly demonstrate the potential to provide visible to infrared overlay measurements using a single sensor. It should be noted that the target used for the measurement at $\lambda = 520$ nm showed a stack sensitivity of 0.59, while target used at $\lambda = 1100$ nm showed a stack sensitivity of 0.12. Since stack sensitivity is a measure for the asymmetry in the diffraction pattern as a function of overlay, this means that the measured asymmetry and thus the signal-to-noise ratio is almost five times greater for the same overlay value for the $\lambda = 520$ nm target as compared with the $\lambda = 1100$ nm target. This explains the difference in performance for these two wavelengths.

In these figures it can be clearly seen that the sensor is sensitive for wavelengths

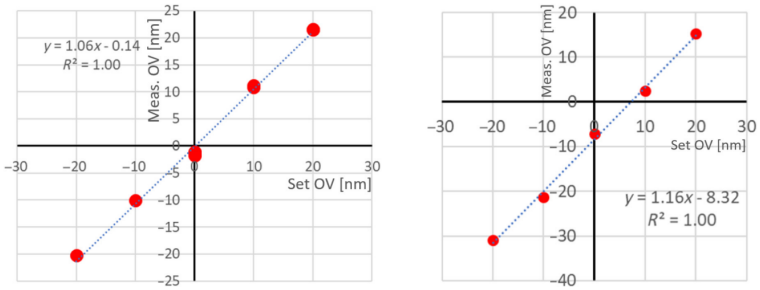

(a) $\lambda = 520\,\text{nm}$, $P = 600\,\text{nm}$ (b) $\lambda = 1100\,\text{nm}$, $P = 1200\,\text{nm}$

Figure 4.6: Measured overlay versus the expected overlay for wavelengths (λ) of 520 and 1100 nm. The grating pitch (P) was selected such that the diffracted light would be close to the center of the pupil for minimum aberrations. These constitute the first-ever overlay measurements ranging from the visible to the infrared with a single sensor. As can be seen, performance is slightly worse in the infrared. This is not inherent to the wavelength, but to the sample that we used as is explained in the text.

ranging from the visible to the infrared. Large errors are still present however due to a combination of low stack sensitivity, poor focus control and a poor beam quality in combination with oblique illumination. In addition, the sensor is sensitive to phase fluctuations and therefore to air turbulence, which also affects the static reproducibility, as shown in Fig. 4.7.

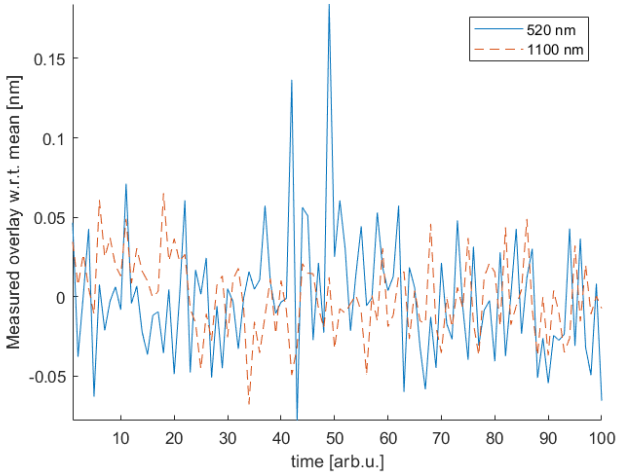

Figure 4.7: Static reproduction of the overlay with respect to its mean value for 600 and 1200 nm pitch targets measured at a wavelength of 520 and 1100 nm, respectively. After preparing the setup, 100 camera images were acquired without intentionally changing the setup in any way. Any fluctuations in the measured overlay value therefore represent noise which we attribute to mechanical instabilities and turbulence.

The 3σ-deviation was determined to be 122 and 76 pm for the $\lambda = 520$ nm and $\lambda = 1100$ nm measurements, respectively. The stability of the current breadboard setup can still be improved substantially by a reduction of the optical path lengths and by physically shielding the beams from turbulence.

4.4.3 Coherence gating with df-DHM

Finally, it is worthwhile to note that Si becomes transparent above 1030 nm. This means that a significant fraction of the light propagates to the back of the wafer, reflects of the sample holder, and propagates back to the camera. This is most apparent when comparing a regular dark-field image obtained at 1030 nm to one obtained at 1100 nm as shown in Fig. 4.8(a) and 4.8(b), respectively. Fortunately, the coherence length of the light that we use is much shorter than the thickness of the sample, meaning that the reflected light does not interfere with the reference beam. From a hologram obtained at 1100 nm, it is therefore possible to recover the dark-field image using the process shown in Fig. 4.4. The result is shown in Fig. 4.8(c) and it is indeed clear that the background is much darker.

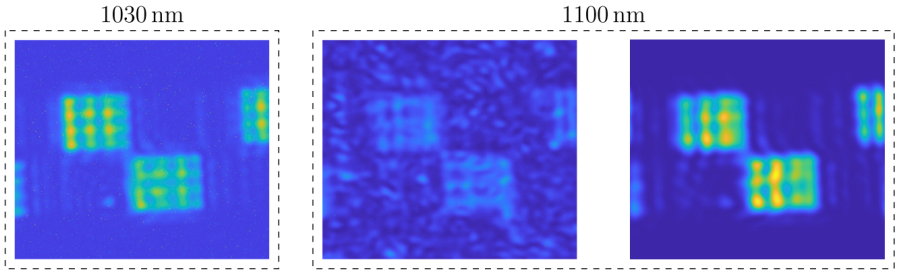

(a) Regular dark-field image at 1030 nm.

(b) Regular dark-field image at 1100 nm.

(c) Recovered dark-field image at 1100 nm.

Figure 4.8: Demonstration of the power of coherence gating at infrared wavelengths. Up to a wavelength of 1030 nm Si is opaque and good images can be obtained using a regular dark-field microscope as is shown in Fig. 4.8(a). For longer wavelengths, Si becomes transparent which allows the light to propagate to the backside of the wafer. This results in a strong background signal as is shown in Fig. 4.8(b). DHM is only sensitive to signals with an optical path length that match the optical path length of the reference beam due to coherence gating. By carefully matching the optical path length for light diffracted of the front side of the wafer, the background can be suppressed quite substantially as shown in Fig. 4.8(c).

4.5 Conclusion

In conclusion, we have demonstrated for the first time a single sensor for measuring overlay on semiconductor wafers from the visible up to the near infrared. The sensor operates based on digital holographic microscopy and is able to obtain the

overlay values using a single image acquisition, while at the same time allowing the use of the full NA of the lens. A good correlation between programmed and measured overlay was found.

In the future, the wavelength range of the sensor can be extended even further by including an additional AOTF operating up to the maximum wavelength covered by the camera, 1600 nm. In addition, the stability of the measurements can be increased by enclosing the beam to avoid turbulence and by increasing the region with good fringe contrast by reducing the bandwidth of the source and by path length matching the illumination beam to the reference beam coming from the opposite side of the sensor. Another interesting addition to the sensor is the aberration correction technique, that will be explained in the next chapter and which will increase the image quality and remove the need for mechanical refocusing. Finally, many other technical improvements are envisioned to make the sensor more suited to an industrial setting. DHM therefore provides an interesting route towards the next generation of overlay sensors.

Chapter 5

Aberration calibration and correction with nano-scatterers

We have shown that our microscope offers several features that are beneficial for overlay metrology, like a large wavelength range in Ch. 4. However, imaging with a single lens results in highly aberrated images. In this chapter, we present an aberration calibration and correction method using nano-sized point scatterers on a silicon substrate. Computational imaging techniques are used to recover the full wavefront error, and we use this to correct for the lens aberrations. We present measured data to verify the calibration method and we discuss potential calibration error sources that must be considered. A comparison with a ZEMAX calculation is also presented to evaluate the performance of the presented method.

5.1 Introduction

The aggressive reduction of semiconductor device dimensions as stated by Moores law [2] has driven many improvements in optical wafer metrology and semiconductor processing equipment like lithography. Integrated circuits consist of multilayer complex structures with feature sizes below 10 nm that need to be

The content of this chapter has been published in: Christos Messinis, Theodorus T. M. van Schaijk, Nitesh Pandey, Armand Koolen, Ilan Shlesinger, Xiaomeng Liu, Stefan Witte, Johannes F. de Boer, and Arie den Boef, *Aberration calibration and correction with nano-scatterers in digital holographic microscopy for semiconductor metrology,* Opt. Express **29**(23): 38237-38256 (2 Nov 2021).

controlled in terms of placement (overlay, OV) and minimum feature size (Critical Dimension, CD). As a result, overlay and CD need to be robustly measured with sub-nm precision at high throughput on many points on a wafer, requiring small measurement times in the milli-second range [3].

Optical Overlay metrology has seen notable advances over the years to keep up with the demanding requirements of the semiconductor industry. For many years image-based overlay metrology (IBO) using Box-in-Box (BiB) metrology targets has been the main approach. IBO uses a bright-field microscope to create an image of this BiB target and OV is determined by measuring the position of the inner box edges with respect to the outer box edges. Significant improvement of metrology precision and robustness came when the box structures were replaced by gratings. These advanced imaging metrology targets have a smaller size allowing more features in a device and more edges which improves the precision [9, 10].

Another big step forward was the introduction of (micro) Diffraction-Based Overlay metrology (DBO) where an overlay target consists of overlapping grating-pairs [14]. DBO is a scatterometry-based technique for measuring overlay on advanced layers at high throughput [111]. DBO measures on metrology targets that consist of small overlapping gratings with approximately 8×8 µm^2 size. An overlay error between these overlapping gratings creates a small intensity difference between the $+1^{st}$ and -1^{st} diffraction order, which scales linearly with overlay. Dark-field microscopy with high-quality optics is used to create $+1^{st}$ and -1^{st} order images of the metrology targets on a camera and these images are used to determine overlay (OV). Robustness and sub-nm accuracy is possible by optimizing the grating etch and using carefully selected multiple wavelengths [112]. However, the relentless push to follow Moores law drives existing optical overlay metrology to the extreme limits of its possibilities. For example, novel devices and process flows result in the use of new materials that are only sufficiently transparent at infrared wavelengths which drives the need for OV metrology tools that cover a larger wavelength range. In addition, there is a strong push to reduce the size of the metrology targets which requires improved imaging resolution in OV metrology. On top of this, the diffraction efficiency of overlay targets continues to decrease to the 0.01 % levels due to thin resist that is used in EUV lithography and increased light losses in the stack of layers that cover the bottom grating. Last but not least, a solution for all these challenges needs to be realized at acceptable cost and in a small footprint since available space for metrology is limited.

We are exploring dark-field Digital Holographic Microscopy (df-DHM), as a DBO metrology technique that can potentially address these challenges [110]. Our df-DHM uses a supercontinuum source in combination with an Acousto-Optical Tunable Filter (AOTF) as a tunable light source and a single uncoated aspheric imaging lens which allows imaging over a large wavelength range since there are no anti-reflecting coatings that limit the usable wavelength range. Moreover, this results in a compact sensor with a high transmission and at acceptable cost. As an alternative for a single imaging lens, a catadioptric Schwarzschild objective could be of interest as well [113]. However, the central obscuration of

these objectives limits the freedom in optimizing the wavelength and pitch of a metrology grating for best accuracy and robustness. This makes these objectives less preferred for the high-end metrology applications for which our df-DHM is intended.

However, a single aspheric lens only offers diffraction-limited imaging performance for the wavelength for which the lens was designed. For other wavelengths large aberrations will significantly degrade the image quality to levels that are unacceptable for metrology applications. For example, Figure 5.1(b) shows a dark-field image of a grating with a pitch of 400 nm that was obtained with our single-lens setup using a wavelength of 532 nm and an illumination angle of incidence of 70° (Fig. 5.1(a)). For these measurement settings, the -1st diffracted order passes through the edge of the exit pupil where spherical aberration will lead to a serious image degradation. Figure 5.1(c) shows the wavefront error in the exit pupil of our lens (Thorlabs A240TM) which has been calculated with ZEMAX optical design software using nominal lens design data. The graph shows the Zernike coefficients of this wavefront error where we have used the fringe-indexing convention (Appendix 5.A). It can be clearly seen that a large 4th order spherical aberration (Z_9) is present that explains the poor imaging quality in Figure 5.1(b).

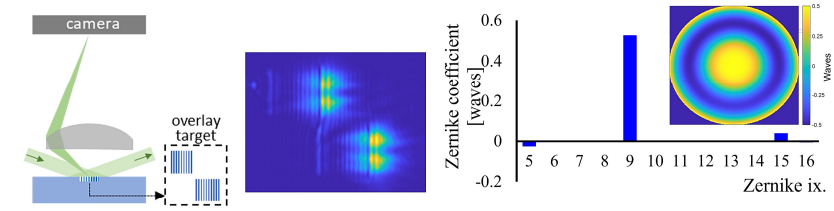

(a) Dark field microscope (b) Dark field mage (c) Zernike coefficients for nominal lens

Figure 5.1: (a) schematic drawing of a dark field microscope with a 532 nm wavelength and 70° illumination angle. (b) dark field image of 400 nm grating pitch targets. (c) Zernike decomposition for Thorlabs A240TM lens as obtained with ZEMAX for λ = 532 nm and NA = 0.465.

Fortunately, Digital Holographic Microscopy (DHM) is able to correct for these lens aberrations since a hologram allows us to retrieve the complex field of the aberrated image. This complex field can then be back-propagated to the exit pupil where we can apply a wavefront error correction. Calibrating wavefront aberrations in DHM has been a subject of research for many years. It has been shown that the wavefront errors introduced by a microscope objective and lenses can be successively removed in DHM [50, 55], as well as spherical aberration [56], chromatic aberration [57], astigmatism [58, 59], or anamorphism [60, 61]. For the wavefront reconstruction in DHM with a single hologram, an accurate knowledge of setup parameters such as the wavefront shape of the reference beam and the object-image distance are critical.

The possibility of correcting lens aberrations in digital holography was first outlined by Stadelmaier and Massig [56]. A pupil-based evaluation of the com-

plex point-spread-function (PSF) was originally proposed by Charrire *et al.* [114], where the complex amplitude point-spread function of a high NA microscope objective was measured with DHM and the retrieved wavefront error was decomposed in a set of Zernike polynomials. In that work the authors used the fiber tip of a scanning near field microscope as a point source.

Here we will present aberration calibration and aberration correction for dark-field DHM by measuring the complex PSF using point scatterers on a flat substrate. In contrast to the work presented in [114, 115] we use a single imaging lens with high aberration levels instead of a high-quality microscope objective. Moreover, instead of using a strong point source (a single-mode fiber tip) we use a nanometer-sized scattering structure that has been created on a bare silicon wafer surface. Such a structure can be reproducibly made in various ways and allows an easy and fast in-line aberration calibration in DHM-based wafer metrology. The amount of light that is diffracted from such a small structure is weak, but we will show that the coherent amplification of the reference wave in DHM still allows wavefront calibrations with sub-milli-wave repeatability. We will also show that this method is able to calibrate and correct even very large aberrations in a single lens df-DHM. Finally, our method uses a spherical reference wave coming from the tip of a single-mode fiber without collimation optics. As a result, the reference wavefront shape is known with a high degree of accuracy which helps to reduce wavefront calibration errors.

In the next section (5.2) we will briefly explain the concept of lens calibration using a point-scatterer in a single-lens DHM setup. We will show that non-telecentric single-lens imaging allows us to use a spherical reference wave coming from the tip of a single mode fiber. We will then present our experimental df-DHM setup followed by a detailed description of the calibration procedure and the measured wavefront aberrations of our single lens. Section 5.3 presents results of lens aberration calibration with a point source and on the correction that has been applied to highly aberrated images of small grating targets that are used for overlay metrology. Section 5.4 discusses potential error sources that impact the precision and accuracy of our aberration calibration method and section 5.5 concludes the paper with an outline of the following steps that we plan to take to improve overlay metrology.

5.2 Theory

5.2.1 Imaging model of a single lens Digital Holographic Microscope

Many DHMs create an image of an object with a microscope objective and a tube lens [26, 115]. Such a double-telecentric imaging setup introduces no quadratic wavefront curvature in the image and a collimated off-axis reference beam is used to retrieve the complex image via well-known Fourier transform techniques. This collimated reference beam is often made with a beam expander and wavefront errors in this beam expander will impact the retrieved complex image and need to be compensated.

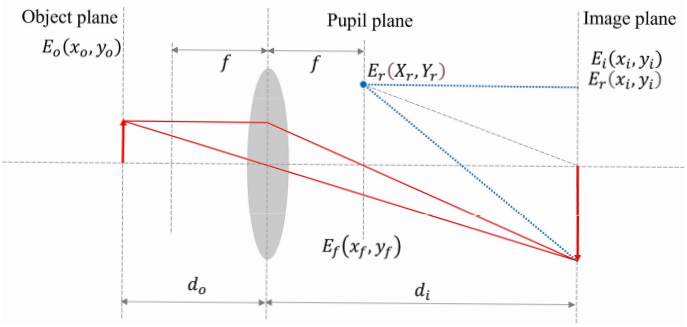

Figure 5.2: Schematic drawing of a single lens holographic imaging system, where d_o is the object distance, d_i is the image distance and f is the focal length of the lens. Red solid lines indicate the ray tracing of the object beam while blue dotted lines indicate the presence and orientation of the spherical reference beam.

Alternative designs for DHM use only a microscope objective to produce a magnified image of an object, which is also equivalent to a lensless holographic setup with an object wave emerging directly from the magnified image of the specimen and not from the sample itself [49, 116]. Usually, these designs use a lens in the reference beam to produce a spherical reference wave with a curvature that matches the curvature that is created by the microscope objective. The additional optical elements on the reference beam path may add undesired wavefront errors that should also be calibrated.

Our fiber-coupled df-DHM setup, uses a single imaging lens which adds a quadratic wavefront to the complex image field on the camera. At first sight, this quadratic wavefront may seem undesired. However, such a wavefront allows the use of a spherical reference wave which can be created using the tip of a single-mode fiber. This further reduces the required amount of optics and therefore the number of potential error sources.

Using the plane wave propagation model as described by Goodman in [23] we can show that the complex field E_i of the image on the camera is given by:

$$E_i(x_i, y_i) = e^{j\frac{\pi}{\lambda(d_i - f)}(x_i^2 + y_i^2)} \left(H(x_i, y_i) \otimes E_o\left(-\frac{x_i}{M}, -\frac{y_i}{M}\right)\right). \tag{5.1}$$

Here $\otimes$ denotes a convolution and $H(x_i, y_i)$ is the Fourier transform of the aperture stop in the back focal plane of the lens (for the full derivation of Eq. (5.1) see appendix 5.B). H is essentially the complex point-spread-function (PSF) of this single-lens imaging system. $E_o(-\frac{x_i}{M}, -\frac{y_i}{M})$ is the complex field in the object plane and M is the magnification. The quadratic phase term in Eq. (5.1) has a radius of curvature $d_i - f$ where d_i is the image distance and f is the focal length of the lens. For clarity, the symbols used in Eq. (5.1) are also indicated in Figure 5.2 which shows the paraxial single lens imaging along with the reference beam.

The spherical reference beam E_r at the image plane in our df-DHM has a radius of curvature $d_i - f$ and its complex amplitude in the image plane is given

by:

$$E_r(x_i, y_i) = Ae^{j\frac{\pi}{\lambda(d_i-f)}((x_i-X_r)^2+(y_i-Y_r)^2)}. \tag{5.2}$$

The reference beam, that is propagated from the tip of a fiber, generates spherical waves that are described with the quadratic phase approximation. The quadratic phase terms in the image field and the reference beam are identical when the fiber tip is positioned in the pupil plane of the imaging lens. In this case the coherent sum of the image field and the reference wave yields an intensity I on the camera:

$$I(x_i, y_i) = |E_i|^2 + A^2 + Ae^{j\frac{2\pi}{\lambda(d_i-f)}(x_iX_r+y_iY_r)}\left(H(x_i, y_i) \otimes E_o\left(-\frac{x_i}{M}, -\frac{y_i}{M}\right)\right) + c.c. \tag{5.3}$$

In this expression, the term c.c. denotes the complex conjugate. The quadratic phase terms in the image field and the reference beam are eliminated, and the complex field of the image field can be retrieved with standard Fourier transform techniques.

5.2.2 Lens calibration and correction with complex point-spread-functions

The usual way to characterize an optical imaging system, is its point-spread function (PSF) which is an image of a single point source. A point source illuminates the lens aperture with a spherical wave that is insensitive to non-uniformity in the illumination beam. Without aberrations, the wavefront in the exit pupil of our df-DHM will be perfectly spherical (Fig. 5.3), and the point source will be imaged as a diffraction limited Airy disk. However, lens aberrations will deform the wavefront (red curve in Fig. 5.3) and will result in an aberrated Airy disk with enhanced side lobes and a lower peak intensity. For isoplanatic imaging the PSF is invariant to a shift of the object and in that case a measurement of the complex PSF at 1 point in the field is sufficient to calibrate the aberrations in the imaging system. For this assumption to be valid we keep the object in the center of the field of view (FoV), where any small shifts will not impact the measured wavefront.

For a point source that is centered in the object plane, we find for the retrieved complex PSF in the image plane:

$$PSF(x_i, y_i) = H(x_i, y_i) \otimes \delta\left(-\frac{x_i}{M}, -\frac{y_i}{M}\right). \tag{5.4}$$

Here, the point source is represented by the Dirac-delta function δ. The complex field can be computationally back-propagated to the pupil plane using a Fourier transform, which yields:

$$\mathcal{F}\{PSF\} = |P(x_f, y_f)|e^{jW(x_f, y_f)}. \tag{5.5}$$

Here $|P(x_f, y_f)|$ represents the amplitude of the field in the exit pupil and $W(x_f, y_f)$ represents the wavefront aberration of the object wave. In general,

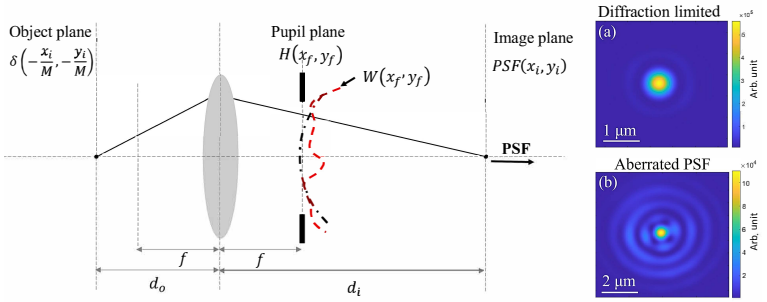

Figure 5.3: The lens calibration process with a point source. A point-scatterer illuminates the whole lens aperture. A lens free of aberrations corresponds to a smooth spherical wavefront and a diffraction limited point-spread function (PSF) on the image plane (shown in (a). A non-ideal lens will deform the wavefront and will result in an aberrated PSF in the image plane (shown in (b).

this wave aberration is field-dependent. However, non-isoplanatic behavior is usually small for the field sizes that are commonly used in metrology.

Once the lens aberrations have been calibrated with the method as described above, the aberration correction in off-axis DHM is quite straightforward. Fourier transforming the camera image yields the spatial frequency spectrum of the hologram. This consists of a baseband term and two sidebands. These two sidebands are, respectively, the complex field in the exit pupil and its complex conjugate. We select the sideband with the complex field in the exit pupil and we multiply this with the conjugate wavefront error $e^{-jW(x_f,y_f)}$ that we calibrated with the point-scatterer. Then with a second Fourier transform we obtain an aberration-corrected amplitude image of the object.

In practice, the object (a metrology target in our case) is often imaged at a different focus position as the focus position that was used for the aberration calibration. As a result, a (small) focus correction may be needed as well which is easily realized by adding a focus correction term to the field in the exit pupil. The lens aberration and focus correction is given by:

$$\mathcal{F}\{E_{f_{cor}}(x_f,y_f)\} = \mathcal{F}\{E_f(x_f,y_f)\}e^{-jW(x_f,y_f)}e^{-j\alpha_4 Z_4(x_f,y_f)}. \tag{5.6}$$

Where $E_{f_{cor}}(x_f,y_f)$ is the corrected field in the exit pupil, with $e^{-j\alpha_4 Z_4(x_f,y_f)}$ as the focus correction term. The term α_4 represents the amount of defocus and $Z_4(x_f,y_f)$ is the Zernike polynomial, as presented in [117]. The polynomial expression of Z_4 is given in Appendix 5.A. In the following section, we apply this concept to df-DHM to obtain the complex amplitude point-spread function of our imaging system and correct for the aberration introduced by the lens element on an overlay test target.

5.3 Experimental results of aberration calibration and correction

5.3.1 Sample preparation

To test the calibration method that we described in the previous section we created two samples with well-defined point objects. The first sample is a bare silicon substrate on which we deposited gold nanoparticles. The nanoparticle solution (A1C-70-CIT-DIH-1-5, Nanopartz) is specified to contain 75 nm gold cubes with citrate ligands that are dispersed in water. For the preparation we cast a drop of 20 uL on the silicon and after 30 seconds we rinse with ethanol and dry with N_2 (dinitrogen). The size of the nanoparticles was measured to be approximately 80 nm while the shape was varied, with spherical, nanorods or other nanoparticles also present. Potential nanoclusters were also formed at some parts of the sample but for the calibration we used an isolated gold nanoparticle, like the one that is shown in the scanning electron microscope (SEM) image on Figure 5.4. The second sample was also fabricated on bare silicon, but now a nano-hole pattern was milled with a 30 keV focused gallium ion beam (FEI Helios Nanolab 600). The ion beam current was set to 100 pA with a focal spot diameter of 80 nm. The nano-hole array was milled in 500 cycles and with a dwell time of 1 ms.

5.3.2 Experimental setup

To demonstrate DHM capability for lens aberration calibration we selected as our imaging lens an off-the-shelf plano-aspheric lens (Thorlabs A240TM - SL) with an effective focal length of 8 mm and an NA of 0.5. Because of the extreme level of aberrations on the edges of the used lens, we have selected a digital aperture stop of 0.465. This lens is intended for collimating laser diode light with a wavelength of 780 nm and cover glass between the laser and the lens. The lens material was molded glass type D-LAK 6 with a focus shift of 0.35 mm in the visible range. In our experiment, however, we used a 532 nm wavelength and there was no cover glass present between the object and the lens. As a result, we can expect high spherical aberrations that will result in a severely degraded image of the metrology targets that we are interested in (as already shown in Figure 1).

The off-axis df-DHM setup (Fig. 5.4(a)) uses a fiber coupled Supercontinuum White light source (LS; Leukos Rock 400 5) combined with an Acousto-Optical Tunable Filter (AOTF; Gooch & Housego TF550-300-4-6-GH57A). This AOTF device has a bandwidth in the range of 47 nm and covers the whole visible wavelength range from 400 to 700 nm. For the majority of the presented experiments, we have selected an AOTF frequency that corresponds to a 532 nm wavelength with a bandwidth of 5 nm. We verified the selected wavelength with a bandpass filter (FLH532-4). A delay line is used to match the optical path of the reference and the illumination beam and polarization maintaining fibers (PM - Shafter-Kirchhoff PMC-400Si-2.3-NA014) are used to couple the light from the source

path to the sensor head. The sensor head is comprised of two off-axis illumination arms which illuminate the target from opposite directions at an incident angle of approximately 70° with respect to the normal of the object plane.

For DBO measurements the two sides generate the -1st (L. Arm) and +1st (R. Arm) diffraction orders. Each illumination arm generates a Gaussian-shaped spot on the object plane ($1/e^2$ diameter approximately 130 µm) with the use of two microscope objectives (FL- 50X Mitutoyo Plan Apo Infinity Corrected Long WD Objective) and two adjustable mirrors for fine-tuning the angle of incidence. These objectives give a well-defined illumination spot in the whole visible range but at the same time negate the compactness of the setup and increase the total cost. We plan to replace them with small parabolic mirrors that can operate in a broader wavelength range, combined with an illumination beam characterization. In addition, two corresponding spherical reference beams are coherently added to the corresponding object beams. The two reference beams have different azimuthal angles resulting in a different orientation of the sidebands of the spectra of the resulting holograms. With this approach, two holograms are captured by the image sensor using only one image acquisition, and the two object fields can be retrieved with only three Fast Fourier Transforms (FFTs). Further details of this setup and the parallel acquisition of multiple holograms are given in Ch. 2. The microscope consists of the single plano-aspheric Thorlabs lens (SL) and a camera (Basler acA4112-8gm) with a 12 Mpixel CMOS image sensor with 3.45 µm pixel size. We chose a nominal magnification of 100x by placing our detector 800 mm away from the lens.

5.3.3 Aberration Calibration in dark-field Digital Holographic Microscopy

For calibrating the lens aberration, we used only one of the illumination beams and the corresponding reference beam (R.arm and R.ref in Figure 5.4). The illuminated sample contains either gold nanoparticles or nanoholes and light that is scattered from these structures is captured by the lens and creates an aberrated PSF on the camera. This aberrated PSF is coherently mixed with the spherical reference beam and the resulting hologram is used to retrieve the complex PSF. Figure 5.4(b) shows some of the images in the various steps of the retrieval of the complex PSF and the complex field in the exit pupil.

With df-DHM we obtain the hologram of the PSF and by Fourier transforming we move to the spatial frequency domain (angular spectrum) where the cross-correlation or interference terms of Eq. (5.3) are fully separated from the base-band. To retrieve the amplitude and the phase of the PSF, using the angular spectrum method that was first outlined by E. Leith and J. Upatnieks [34], we select the sideband that corresponds to the 3^{rd} term of Eq. (5.3) (top right sideband), filter out the other terms and shift this sideband to the origin of the angular spectrum.This yields the complex field in the exit pupil (Eq. (5.5)). We could retrieve the PSF in the image plane (Eq. (5.4)) with an additional FFT, but this is not required for the aberration calibration.

In order to verify our results with ZEMAX, we decompose the wavefront aber-

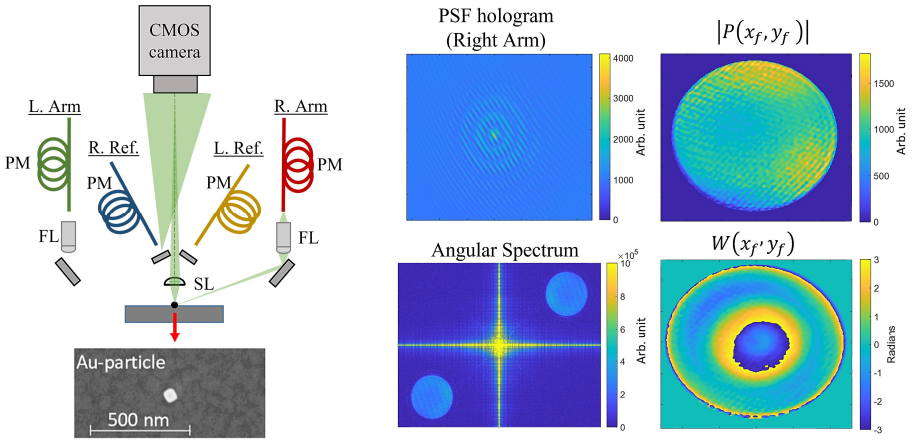

(a) Sensor head

(b) Holographic Reconstruction process

Figure 5.4: (a) the fiber-coupled df-DHM. An Au nanoparticle of approximately 80 nm size is illuminated with an oblique illumination beam (R. Arm) of 70°. The object beam will form a PSF that is coherently mixed with the reference beam (R. Ref) resulting in a hologram on image plane. An SEM image of the sample (Au nanoparticle) is shown in the bottom. (b) the holographic reconstruction process. By Fourier transforming the PSF hologram we back-propagate to the pupil plane and the angular spectrum. To retrieve the complex field in the pupil (Eq. (5.5)), we select one of the sidebands, filter out the other terms and shift it to the origin of the angular spectrum. The right-hand side graphs show the recovered wavefront (amplitude and 2π-wrapped phase of the PSF).

rations of the imaging lens into Zernike polynomials [118–120]. ZEMAX simulations generates Zernike coefficients using the fringe-indexing convention [117] which is commonly used by lens designers [121]. More details about Zernike polynomials are summarized in Appendix 5.A.

The wavefront error of the pupil that we recovered with our calibration method, contains 2π phase wrapping errors because of the large spherical aberrations of our lens. This is of no concern for aberration correction as the wrapped phase distribution can be directly used. However in order to quantify the aberrations by a Zernike decomposition, we must apply a 2D phase unwrapping algorithm to the measured wavefront error. The absolute deformation of the phase front can now be decomposed in Zernike polynomials. Figure 5.5 shows the unwrapped wavefront errors for the two measured samples and a first comparison of the measurements and the ZEMAX prediction in terms of Zernike coefficients.

For this first comparison in Figure 5 we present the measured wavefront errors of the gold nanoparticle (PSF 1) and the FIB-sample (PSF 2). Using the same color-scale the two wavefronts look almost identical with a small asymmetry on the wavefront error distribution. On the Zernike decomposition of the wavefronts (Fig. 5.5(a)), it is shown that the two samples are in quite good agreement. Almost all the Zernike coefficients follow the same trend with Z_9 coefficients

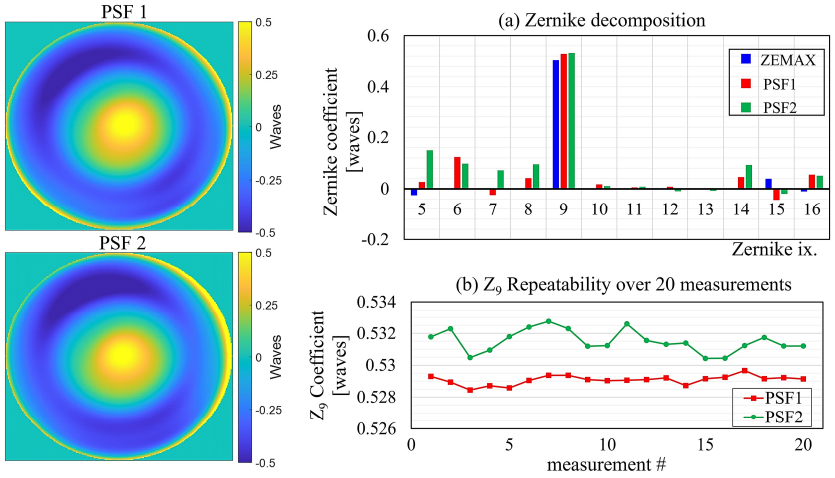

Figure 5.5: (a) Zernike decomposition of measured wavefront errors for two different samples along with simulated data as predicted with ZEMAX optical design software (blue bars). PSF 1 (red bars) is the gold nanoparticle and PSF 2 (green bars) is the FIB-sample. The results were obtained for $\lambda = 532$ nm and NA = 0.465. (b) Repeatability measurements of the Z_9 aberration of the measured PSFs.

with only 3 milli-waves difference. The only significant deviation between the two samples is on Z_5 (astigmatism) where we measured a 0.12 waves difference. We are still investigating the main cause for this deviation.

Figure 5.5(a) also shows the Zernike decomposition of the ZEMAX wavefront. The observed differences between the measured wavefront and the ZEMAX wavefront are due to a combination of lens manufacturing tolerances and residual measurement errors in our setup. The lens in our setup is mass-produced and the tolerance data of this lens are not available but are expected to be significant. In our setup we have also identified a few small error sources that we will discuss in section 5.4. We also measured the repeatability of the retrieved Zernike coefficients. For each of the two nano-scatterers we acquired 20 holograms under the same conditions and the measured reproducibility of the dominant spherical aberration Z_9 is shown in Fig. 5.5(b). Despite the small amount of light scattering, we found a standard deviation of only 0.3 milli-waves for PSF 1 and 0.7 milli-waves for PSF 2.

We also performed a wavefront measurement through focus, and we compared the retrieved Zernike polynomial Z_4, that correspond to defocus, with the amount of Z_4 that was expected for this lens. Figure 5.6(a) shows the comparison of the measured data and the expected behavior. These results were obtained by measuring the PSFs for various focus positions. For PSF1 1 µm steps from -6 µm up to +6 µm defocus were obtained along with two more measurements in the extreme cases of 10 µm defocus. For PSF2 since the signal for the nanohole array was weaker we limit the measurements to 2 µm steps and align the measured Z_4 with the data for PSF1. As a result, for the second sample the defocus range was

from -9 µm up to 5 µm. For larger positive defocus the visibility of the PSF2 was low and we could not complete the measurement. The two sets of measured data change linearly through focus with almost the same slope and with R^2 values of almost unity. There is a small offset in the measured graphs compared to the calculated graphs of approximately 2 µm which can be explained by the fact that the depth-of-focus (DoF) scales with λ/NA^2 which in our case yields a DoF of approximately 2 µm and the best focus position of the measured PSFs was done manually.

Since we ultimately also plan to use our DHM setup over a large wavelength range, we also measured how the amount of spherical aberration Z_9 varies over the wavelength range that we could cover with the AOTF that we currently have in our setup. Figure 6(b) shows the measured through-wavelength Z_9 variation for the gold nanoparticle sample (red dots) and the nanohole sample (green dots), along with the variation predicted by ZEMAX (blue dotted line). It can be seen that our measured wavelength variation is consistent with the behavior that we expect from the dispersive nature of the lens material. Moreover, we also see that our measurement results are in agreement with the ZEMAX calculations. The discrepancy between ZEMAX calculations and measured data can be explained by some uncertainty in the actual wavelength of our AOTF and some uncertainty in the actual NA that was used in the ZEMAX calculation. The AOTF drifts over time and can correspond to an uncertainty on the selected wavelength that deviates from 1-2 nm to 5-10 nm in the whole visible range. At the same time, due to numerical approximations, we estimated an uncertainty of 10^{-3} on the NA that was used in the ZEMAX calculations.

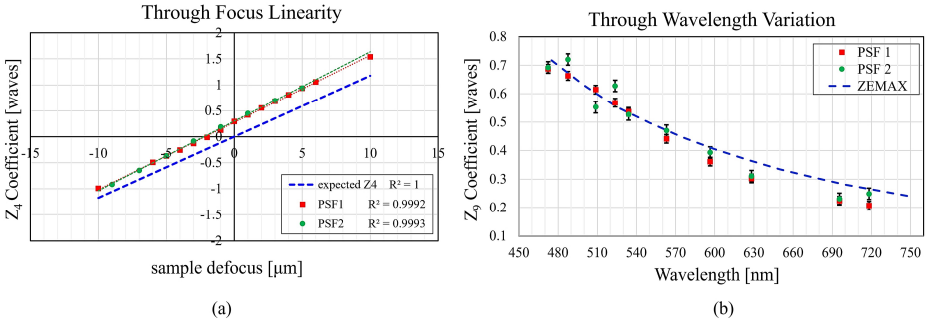

Figure 5.6: (a) through focus comparison of the measured PSFs and the predicted slope from ZEMAX. Red squares are the data points of the gold nanoparticle fitted with a red dashed line while the green circles are the data points for the nanohole fitted with a green dotted line. The blue dash-dotted line is the Z_4 slope predicted by a ZEMAX calculation. (b) through wavelength variation of Z_9 of the measured PSFs and the predicted slope from ZEMAX. Red squares are the data points of the gold nanoparticle with error bars indicating an uncertainty of about 15 milli-waves while the green circles are the data points for the nanohole with uncertainty of about 25 milli-waves. The blue dashed line is the Z_9 slope that was calculated with ZEMAX.

In the following subsection we use the calibrated wavefront errors to correct for the lens aberrations and we will show how this improves the imaging of grating targets that are used for OV metrology.

5.3.4 Aberration Correction in dark-field Digital Holographic Microscopy

The df-DHM setup is intended to be used for diffraction-based Overlay metrology on multiple grating targets. To test the aberration correction capabilities of our df-DHM we use a test wafer with overlay targets of small overlapping gratings. The gratings in the bottom layers are etched in a silicon wafer and have an etch depth of about 90 nm. The gratings in the top layer are lithographically made in a resist film with a thickness of about 90 nm. The size of these square gratings varies, and in this experiment, we will focus on gratings of 10×10 µm^2, 8×8 µm^2 and 5×5 µm^2 size and a pitch of 400 nm. This pitch in combination with the used wavelength of 532 nm will result in highly aberrated images since the 1$^{\text{st}}$ diffraction orders are at the edge of the lens aperture where the impact of aberrations is highly visible, as already shown in Figure 5.1.

In these measurements we used the left illumination pair (L. Arm) to generate the -1$^{\text{st}}$ diffraction order and the right illumination pair (R. Arm) to generate the +1$^{\text{st}}$ diffraction order as shown in Figure 5.4. The two holograms were measured in parallel, as explained in Ch. 2. For the calibration the nano-scatterers were also placed at the center of the field of view (FoV). Figure 5.7 shows the aberration correction process for the image that is formed by the -1$^{\text{st}}$ diffraction order.

Figure 5.7 shows the impact of lens aberrations on the quality of a retrieved image of an overlay target. The highly aberrated image of the targets with a 400 nm grating pitch can significantly affect the overlay measurements since there is not a well-defined target area to measure the total amount of light that is diffracted in the -1$^{\text{st}}$ order. Moreover, in real production wafers an overlay target is normally surrounded by patterns and the aberrations would cause a large amount of optical crosstalk from the surrounding patterns into the target area. The correction of the retrieved aberrated image of the -1$^{\text{st}}$ diffraction order is shown in Figure 5.7. As described in subsection 5.2.2, the complex field E_f in the pupil is multiplied by the conjugate wavefront aberration $e^{-jW(x_f,y_f)}$ that we obtained in the calibration step. For the correction of the two diffraction orders the same error phase mask was used. Moreover, an additional focus correction $e^{-j\alpha_4 Z_4(x_f,y_f)}$ was also applied since the gold nanoparticle was measured at a (slightly) different focus than the grating sample.

Figure 5.8 shows the aberration correction of the retrieved df-image for the +1$^{\text{st}}$ diffraction order. The correction steps are the same. We are using the same raw hologram from which we reconstruct the raw df-images. For the correction we apply the same wavefront error phase mask and with an additional FFT we obtain the corrected df-image for the +1$^{\text{st}}$ diffraction order.

As shown in Fig. 5.7 and Fig. 5.8, the -1$^{\text{st}}$ and +1$^{\text{st}}$ order images of the 400 nm test grating are now nicely corrected resulting in a vast improvement in sharpness. Even an incidental dust particle located on the left of the first

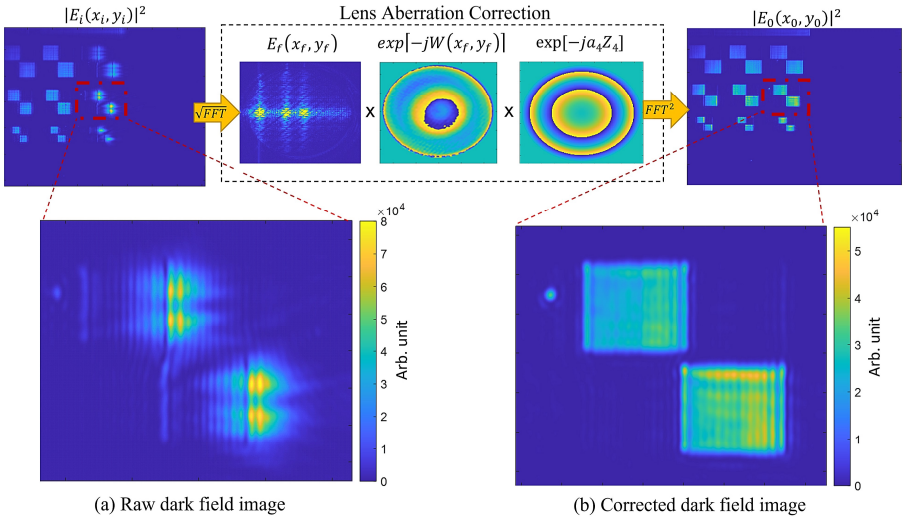

(a) Raw dark field image (b) Corrected dark field image

Figure 5.7: The aberration correction process for the -1st diffraction order, A retrieved -1st order amplitude of OV targets with df-DHM, $E_i(x_i, y_i)$ is back-propagated to the pupil. In pupil plane we select the cross-correlation term of the -1st order $E_f(x_f, y_f)$ and we filter out the remaining signals. We then multiply the complex field with the phase of the retrieved wavefront error from the calibration $e^{-jW(x_f, y_f)}$ and the focus correction term $e^{-j\alpha_4 Z_4}$. With an additional FFT the corrected image is obtained $E_0(x_i, y_i)$. (a) A close look on the -1st intensity of a highly aberrated target with grating pitch of 400 nm and 8 $\times$ 8 µm^2 size. (b) a close look of the corrected -1st intensity image of the same target.

grating is now sharply imaged. This significant improvement in image quality will improve metrology performance since the target area is now very localized and well-defined. Moreover, it is expected that crosstalk from surrounding patterns will also be significantly reduced. Before concluding this section, it is important to emphasize that our aberration correction in the exit pupil implicitly assumes that the aberrations are the same for every position in the field. This assumption cannot be generally made. However, for OV metrology we focus on an area of approximately 100 µm^2 and within this region we can assume that the aberrations are the same.

5.4 Potential error sources in our calibration method

In the previous section we showed that our calibration and correction method significantly improves image quality even in the presence of large aberrations. In this section we will have a closer look at some items that must be considered for the best possible aberration calibration and correction result:

1. size of the selected PSF

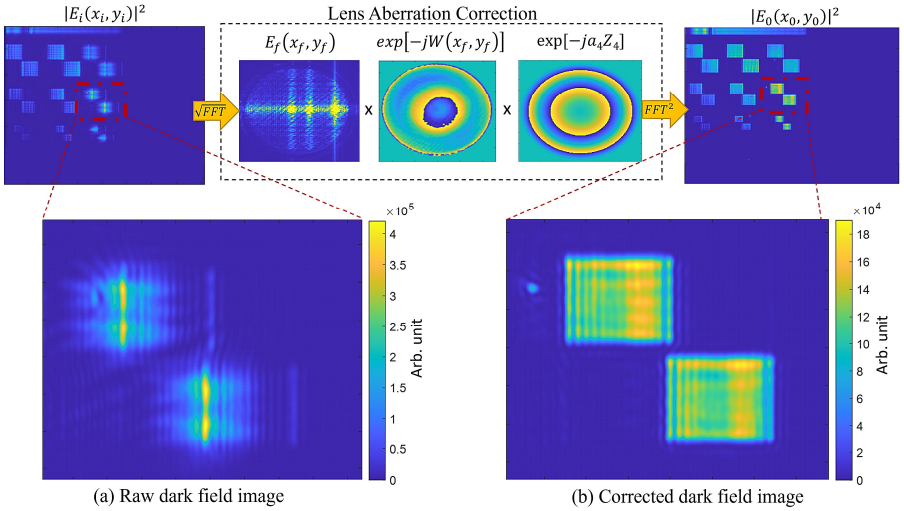

(a) Raw dark field image (b) Corrected dark field image

Figure 5.8: The aberration correction process for the $+1^{\text{st}}$ diffraction order, A retrieved $+1^{\text{st}}$ order amplitude of OV targets with df-DHM, $E_i(x_i, y_i)$ is back-propagated to the pupil. In pupil plane we select the cross-correlation term of the $+1^{\text{st}}$ order $E_f(x_f, y_f)$ and we filter out the remaining signals. We then multiply the complex field with the phase of the retrieved wavefront error from the calibration $e^{-jW(x_f, y_f)}$ and the focus correction term $e^{-j\alpha_4 Z_4}$. With an additional FFT the corrected image is obtained $E_0(x_i, y_i)$. (a) A close look on the $+1^{\text{st}}$ intensity of a highly aberrated target with grating pitch of 400 nm and 8×8 µm^2 size. (b) a close look of the corrected $+1^{\text{st}}$ intensity image of the same target.

2. amplitude inhomogeneity of the reference beam
3. decentering of the virtual field E_f in the exit pupil
4. longitudinal position errors of the reference fiber tip

The first 2 items generally result in very small calibration errors that will impact the quality of aberration correction, so it is imperative to keep them at the milli-wave level. Items 3 and 4 can lead to a significant error in the calibrated wavefront but these errors also occur in the imaging of the metrology target so they will effectively cancel in the aberration correction.

5.4.1 Size of the selected PSF

The PSF of an aberrated coherent imaging system generally contains many diffraction rings around the central peak. In practice, however, we can only select a finite part of the PSF in a digital hologram. In that case the measured PSF (PSF_{meas}) can be written as the multiplication of the real PSF (PSF_{real}) and a (rotationally symmetric) window function A_W :

$$PSF_{meas}(x_i, y_i) = PSF_{real}(x_i, y_i) * A_W(x_i, y_i). \tag{5.7}$$

This windowing operation results in a low-pass filtering of the field in the exit pupil since this field will be convolved with the Fourier transform of A_W.This convolution will smoothen steep wavefront variations in the exit pupil so it will result in measured aberrations that are less than the actual aberration. This is clearly visible in Figure 5.9(a) and 5.9(b) which shows the retrieved 4^{th}-order spherical aberration (Z_9) of our lens as function of diameter of the circular window A_W. For the calibration and correction of the overlay targets that we reported in the previous sections we used a circular window with a diameter of 40 µm (indicated with the dashed line in Figure 5.9(c)). This window diameter offers a consistency on the measured Z_9 for both samples as many diffraction rings are included and at the same time potential interference from the surroundings is also minimized.

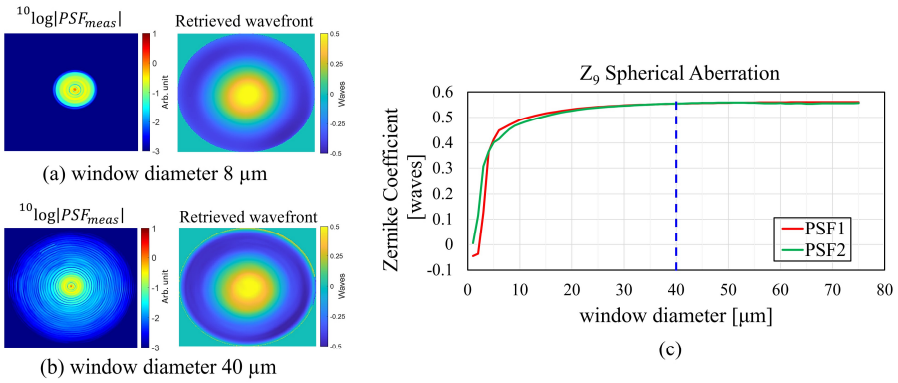

Figure 5.9: (a) The retrieved wavefront of a measured PSF that is multiplied by a 8 µm size window. (b) the retrieved wavefront of the same PSF multiplied with a 40 µm window. (c) Measurement variation of Z_9, spherical aberration of the 2 PSF for different window filtering size that ranges from 1 µm up to 70 µm.

5.4.2 Amplitude inhomogeneity of the spherical reference beam

In the df-DHM setup (fig. 5.4(a)) we use the tip of single mode fiber to generate a well-defined spherical reference wave. To redirect the reference beam to the camera we use a standard half-inch mirror. This additional mirror surface can introduce some micro speckle to the reference beam due to the roughness of the mirror. Moreover, the mirror surface can potentially be degraded over time. The rate of degradation of the coating of the mirror depends on the way the mirror was stored, the humidity and the air flow which can potentially add dust particles in the mirror surface. All these factors can potentially affect the amplitude homogeneity of the reference beam and introduce a small amount of speckle noise in the reference beam.

This speckle noise leads to small amplitude inhomogeneities on the reference beam which affect the retrieval of the complex PSF. This introduces calibration errors on the wavefront measurements, and we need to be sure that the impact

on the lens calibration is sufficiently small. To see the impact of the amplitude inhomogeneity we used a first order approximation to correct the hologram from spatial amplitude variations in the reference beam using the following equation:

$$S_{corr} = \frac{S_{DHM} - S_{REF}}{\sqrt{S_{REF}}}. \tag{5.8}$$

Here S_{DHM} is the acquired digitized camera image of the measured hologram and S_{REF} is the acquired digitized camera image of the measured reference beam. After averaging out the reference beam on a measured hologram we compared the retrieved Zernike coefficients between the raw PSF and the corrected PSF. Figure 5.10(a) presents the measured intensity of the reference beam where the amplitude inhomogeneities are visible. The inset shows an enhanced contrast image of the speckle noise in a region of interest of about 3.5x1.4 mm^2 at camera level. The relative signal variation in this region was measured to be 2.5% which can be further reduced by using a better-quality mirror. Figure 5.10(b) presents the Zernike decomposition of the same sample (PSF 1) when the raw measured hologram (Raw PSF) was used compared to the measured hologram after calibrating for the speckle noise of the reference beam using Eq. (5.8). (Corrected PSF).

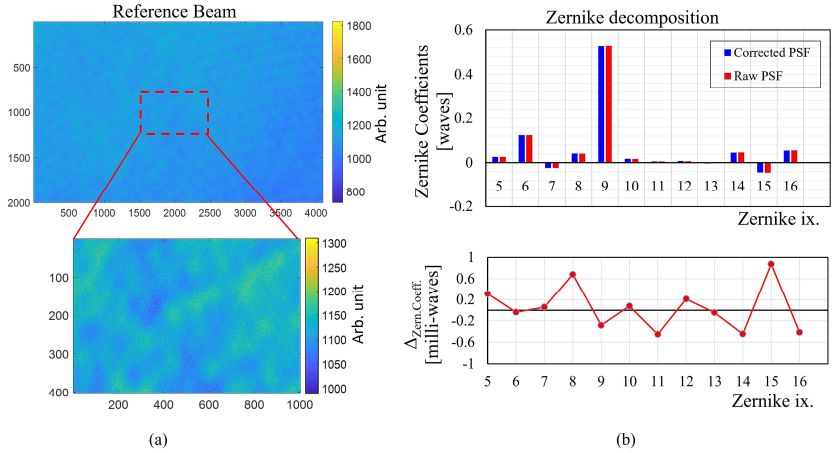

Figure 5.10: (a) The measured intensity of the reference beam and a close look on a region of interest with relative speckle noise of 2.5%. (b) the Zernike decomposition of the retrieved wavefronts of the PSF in the two cases along with the difference of the Zernike Coefficients ($\Delta_{Zern.Coeff.}$) of the two wavefronts in milli-waves.

As shown in Fig. 5.10(b), there is a very good correlation between the two wavefronts with Zernike coefficients difference $\triangle_{Zern.Coeff}$ less than 1 milli-wave. This shows that the amplitude inhomogeneity of the reference beam in our experimental setup has a minimum effect on the measured wavefronts and the assumption that we made in section 5.2.1 is valid.

5.4.3 Decentering of the virtual field E_f in the exit pupil

In the holographic image retrieval, the hologram is initially transformed from the image plane to the pupil plane with a Fourier transform to uncover the baseband signal and the four sideband signals. To retrieve a complex image, we shift the proper sideband term to the origin of the angular spectrum and multiply this with a pupil window (dashed circle in Fig. 5.11(a)) with a radius that is equal to the NA of the imaging lens. In practice a small offset $\vec{s}$ of the shifted sideband can occur as shown in Fig 5.11(a). This will result in a small amount of pupil decentering that lead to small wavefront calibration errors.

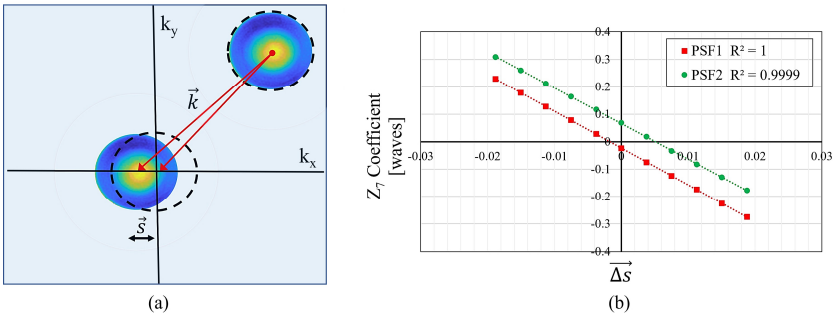

Figure 5.11: (a) Schematic drawing of decentering of the exit pupil. (b) Effect of the decentered pupil to coma Z_7. $\vec{\Delta s}$ is the shift in k space and is equal to λ/FoV.

Figure 5.11 shows a schematic drawing of the pupil after shifting to the origin of NA space and windowing. In this particular case the window defines the NA stop and blocks all signals outside the sideband. A small error shift $\vec{s}$ will slightly de-center the sideband and introduce wavefront aberrations in a manner that is somewhat similar to additional wavefront aberrations that are introduced by an aperture stop shift as reported in chapter 10 of [119]. For a small shift error and a sufficiently smooth wavefront we can approximate the wavefront of the shifted sideband by a Taylor expansion:

$$W(\vec{k}+\vec{s}) = W(\vec{k}) + \nabla W \cdot \vec{s}. \tag{5.9}$$

Here ∇W denotes the gradient of the wavefront W. A large 4^{th} order spherical aberration (Z_9) in combination with a shift $\vec{s}$ (in either k_x or k_y) shows up as, respectively X-coma (Z_7) and Y-coma (Z_8). To show this effect we start with the wavefront error of Z_9:

$$W_9 = \alpha_9(6\rho^4 - 6\rho^2 + 1). \tag{5.10}$$

Here α_9 represents the amount of spherical aberration Z_9 which is multiplied with the Zernike polynomial, expressed in waves and $\rho = \sqrt{{\rho_x}^2 + {\rho_y}^2}$ is the normalized radial pupil position. A small shift in $\triangle\rho_x$ results in a new wavefront

$W_{9,\triangle}$:

$$W_{9,\triangle} = W_9 + \frac{dW_9}{d\rho}\frac{d\rho}{d\rho_x}\triangle\rho_x. \tag{5.11}$$

Evaluating the 2^{nd} term shows that the shifted wavefront introduces X-coma and a tilt in x-direction:

$$W_{9,\triangle} = W_9 + \triangle\rho_x Z_9(24\rho^3 - 12\rho)\cos\phi. \tag{5.12}$$

The 3^{rd} order coma is described by the Zernike polynomial $W_7 = \alpha_7(3\rho^3 - 2\rho)\cos\phi$ (see Appendix 5.A). So the small shift $\triangle\rho_x$ introduces a coma increment with a $\triangle Z_7$ given by:

$$\triangle Z_7 = 8\alpha_9\frac{\triangle k_x}{NA_{obj}}. \tag{5.13}$$

Here NA_{obj} is the edge of the objectives NA. This analysis shows that a small shift error only becomes significant for lenses with large spherical aberrations that we have in our setup. Fortunately, this shift error also occurs in the imaging of the metrology target so residual wavefront calibration errors will effectively drop out in the aberration correction.

Figure 5.11(b) shows the effect of small decentering errors. In this numerical experiment we have deliberately introduced a shift in the k_x direction in the range about -0.02 to +0.02 in k-space. It can be clearly seen that the retrieved amount of X-coma varies linearly with the amount of shift.

5.4.4 Longitudinal position errors of the reference fiber tip

In section 5.2.1 we presented the single lens DHM where the fiber tip of the reference beam is located in the pupil plane as shown in Figure 5.2. In DHM the Z-position of the reference beam defines the Z-location of the Fourier plane where we have the virtual NA stop. However, in practice small longitudinal position errors of the reference fiber tip can occur that result in a mismatch between the Z-location of the virtual Fourier plane and the actual exit pupil of the imaging lens. Here we will show that this results in additional field-dependent coma. The cause of this field-dependent coma is similar to the effect that we described in the previous section and is further clarified in Figure 5.12(a). An off-axis position of the point-scatterer will result in a tilted wavefront behind the lens. This tilt in combination with a Z-offset of the virtual aperture will introduce additional coma that scales linearly with field position of the nano-scatterer. On Fig. 5.12(a) an over-exaggerating drawing is used to highlight the impact of these position errors.

We estimated the longitudinal position error d_{fx} of the reference fiber tip in our setup to be approximately 15 mm, as shown in Fig. 5.12(a). To evaluate the effect of this position error, we measured the wavefront error as function of x-position of the gold nanoparticle. We determined the X-coma (Z_7) and plotted the measured Z_7 as function of x-position in the field. The result is shown in Figure 5.12(b) along with the ZEMAX calculation that was done for an aperture stop that was 15 mm away from the exit pupil. The bottom graph of figure 5.12(b) represents the deviation from a straight line of the measured data.

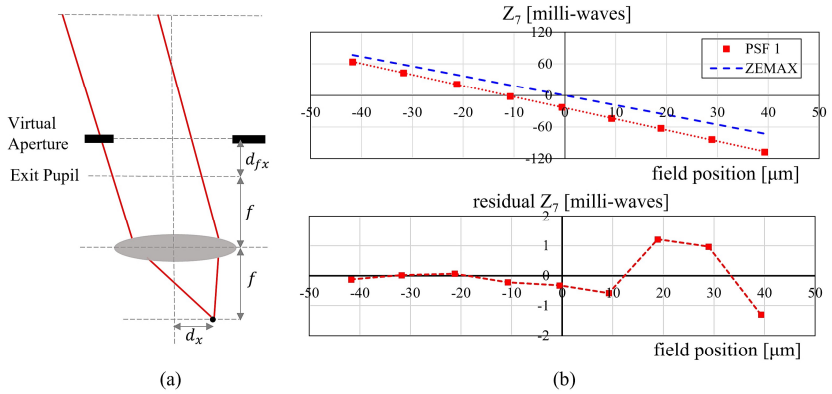

Figure 5.12: (a) schematic drawing of the measured distances in the setup, d_x is the field position variation and d_{fx} is the longitudinal error shift of the reference fiber tip. (b)(Top) Through field comparison of the measured PSF and the predicted slope from ZEMAX. Red dots are the data points of the gold nanoparticle fitted with a dashed line while the solid blue line is the expected Z_7 slope by ZEMAX. (Bottom) the deviation of the measured data from the fitted line.

We observe that our measured data is in good agreement with the ZEMAX calculations. The small difference in the slope can be caused by a residual measurement error of the fiber Z-position. The offset of the measured coma may be real or due to a small offset of the virtual aperture as explained in the previous section. The deviation of the measured coma as function of field position from the expected linear behavior is on average below 1 milli-wave which demonstrates the capability of achieving milli-wave calibration precision using weakly scattering nanostructures.

The field-dependent coma that is introduced by a reference fiber Z-misalignment results in non-isoplanatic imaging where aberration cannot be efficiently corrected. It is therefore essential that the fiber tip is placed as closely as possible to the exit pupil. We checked with ZEMAX that this indeed resulted in a negligibly small field-dependent coma for our Thorlabs lens.

5.5 Conclusion

We have demonstrated a robust method for measuring aberrations and correcting the aberrated images in a df-DHM. We presented measured data that shows that weak point scatterers are very suitable for calibrating large wavefront aberrations in Digital Holographic Microscopy. Although our setup still contained some imperfections like a longitudinal offset of the reference fiber, we have been able to show convincing data of the aberration correction capabilities of our technique. Uncorrected images of metrology targets on a test wafer looked severely distorted but this image quality dramatically improved after applying an aberration correction.

The measured data that we have shown has been measured at only 1 wavelength, but this calibration method is expected to perform well over a wide wavelength range. At longer wavelengths the amount of light that is scattered by a point-scatterer will be significantly reduced. However, since we use an AOTF as a wavelength tuning device the bandwidth of the measurement light will also go up which results in higher intensity levels of the illumination beam. Moreover, the noise in the measured wavefront is in the sub-milli-wave level and is still well below the few milli-wave level that we need.

The wavefront errors measured with a nanohole and a gold nanoparticle were very similar, but we did observe a small ($\approx \lambda/10$) but significant difference in astigmatism (Z_5). One possible cause might be the actual shape of the gold nanoparticle. It provides stronger signals but poor control of the particle shape. The nanohole sample made with the focused ion beam milling tool combined with scanning electron microscopy (FIB-SEM) on the other hand offers excellent control on the nanohole dimensions but the scattering is weaker. Given the already good reproducibility performance we believe that a FIB-SEM -created nanohole target is the better option for further experiment and we plan to explore this in more detail.

The measurement data in section 5.4.4 have shown that a longitudinal offset of the reference fiber tip creates a position dependent coma that varies linearly in the field. This will lead to non-isoplanatic imaging conditions that limits the aberration correction capabilities to a small field of view. However, we plan to fix this longitudinal offset and ZEMAX simulations show that this will significantly increase the field size over which we can computationally correct for aberrations.

The results presented here are a stepping-stone towards the next step in this investigation. Now that we can correct aberrations, we can start exploring the overlay metrology capability of our DHM concept in the case when the metrology targets are surrounded by other structures. The broad point-spread-function (PSF) in the presence of aberrations will lead to severe optical crosstalk from the surrounding structures to the metrology target and degrade metrology performance. The excellent aberration correction capabilities that we have demonstrated here are expected to significantly reduce this optical crosstalk error. Demonstrating and quantifying this improvement will be the next step in this investigation.

Appendix 5

5.A Zernike coefficients

Zernike polynomials are a mathematical description of a 3D wavefront deviation from a plane wave. Every surface deviation is described by a set of circular symmetrical orthogonal basis functions defined over a unit circle. By this scheme the Zernike Polynomials are defined as:

$$Z_n^{\pm m} = Z_j = R_n^m(\rho) \begin{cases} \cos m\phi & \text{for } +m \\ \sin m\phi & \text{for } -m \end{cases}, \tag{5.14}$$

where m is a positive or zero integer, and $R_n^m(\rho)$ is the radial factor given by

$$R_n^m(\rho) = \sum_{s=0}^{(n-m)/2} \frac{(-1)^s (n-s)!}{s!(\frac{n+m}{2}-s)!(\frac{n-m}{2}-s)!} \rho^{n-2s}. \tag{5.15}$$

The norm of a Zernike polynomial is then given by

$$N_{nm} = |Z_n^{\pm m}(\rho,\phi)|^2 = \int_0^{2\pi} \int_0^1 Z_n^{\pm m}(\rho,\phi) Z_n^{\pm m}(\rho,\phi) \rho d\rho d\phi = \frac{\pi(1+\delta_{0m})}{2(n+1)}. \tag{5.16}$$

This norm, however, is not used by programs like ZEMAX. The following Table provides a list of the first 16 Zernike polynomials to be used in the wavefront aberration function expansion in both standard and Fringe notation. These polynomials are commonly used for wavefront calibration since they are well adapted to accurately describe the phase aberrations in the pupil aberration function.

Fringe notation	Standard Notation	Zernike Polynomial	Description
$Z_1(\rho,\phi)$	$Z_0^0(\rho,\phi)$	1	piston
$Z_2(\rho,\phi)$	$Z_1^1(\rho,\phi)$	$\rho\cos\phi$	tilt
$Z_3(\rho,\phi)$	$Z_1^{-1}(\rho,\phi)$	$\rho\sin\phi$	tilt
$Z_4(\rho,\phi)$	$Z_2^0(\rho,\phi)$	$2\rho^2-1$	focus
$Z_5(\rho,\phi)$	$Z_2^2(\rho,\phi)$	$\rho^2\cos 2\phi$	astigmatism
$Z_6(\rho,\phi)$	$Z_2^{-2}(\rho,\phi)$	$\rho^2\sin 2\phi$	astigmatism
$Z_7(\rho,\phi)$	$Z_3^1(\rho,\phi)$	$(3\rho^3-2\rho)\cos\phi$	coma
$Z_8(\rho,\phi)$	$Z_3^{-1}(\rho,\phi)$	$(3\rho^3-2\rho)\sin\phi$	coma
$Z_9(\rho,\phi)$	$Z_4^0(\rho,\phi)$	$6\rho^4-6\rho^2+1$	spherical
$Z_{10}(\rho,\phi)$	$Z_3^3(\rho,\phi)$	$\rho^3\cos 3\phi$	trefoil
$Z_{11}(\rho,\phi)$	$Z_3^{-3}(\rho,\phi)$	$\rho^3\sin 3\phi$	trefoil
$Z_{12}(\rho,\phi)$	$Z_4^2(\rho,\phi)$	$(4\rho^4-3\rho^2)\cos 2\phi$	oblique spherical
$Z_{13}(\rho,\phi)$	$Z_4^{-2}(\rho,\phi)$	$(4\rho^4-3\rho^2)\sin 2\phi$	oblique spherical
$Z_{14}(\rho,\phi)$	$Z_5^1(\rho,\phi)$	$(10\rho^5-12\rho^3+3\rho)\cos\phi$	5^{th} order coma
$Z_{15}(\rho,\phi)$	$Z_5^{-1}(\rho,\phi)$	$(10\rho^5-12\rho^3+3\rho)\sin\phi$	5^{th} order coma
$Z_{16}(\rho,\phi)$	$Z_6^0(\rho,\phi)$	$20\rho^6-30\rho^4+12\rho^2-1$	spherical

Table 2: The first 16 Zernike polynomials as a function of (ρ,ϕ).

5.B Derivation of Eq.(5.1)

We derive Eq. (5.1) in a two-step process:

1. we first calculate the field E_f in the back focal plane of the lens
2. we then obtain the field E_i the image plane by propagating the field E_f to the image plane using the Fresnel approximation as outlined in chapter 5.4 of [23].

According to Eq. (5.6-5.25) in [23] the complex field E_f in the back focal plane of the lens is given by:

$$E_f(x_f, y_f) = P(x_f, y_f) \iint_{-\infty}^{\infty} E_o(x_o, y_o) e^{-j\frac{2\pi}{\lambda f}(x_o x_f + y_o y_f)} dx_o dy_o. \tag{5.17}$$

Where P is a quadratic phase term given by:

$$P(x_f, y_f) = \frac{A(x_f, y_f)}{j\lambda f} e^{-j\frac{\pi}{\lambda f}\left(\frac{d_o}{f}-1\right)(x_f^2+y_f^2)}. \tag{5.18}$$

Here A denotes the aperture stop in the back focal plane. Assuming Fresnel diffraction we can write for the the field E_i at a distance d_i from the lens is:

$$E_i(x_i, y_i) = e^{-j\frac{\pi}{\lambda(d_i-f)}(x_i^2+y_i^2)} \iint_{-\infty}^{\infty} E_f(x_f, y_f) G(x_f, y_f) e^{-j\frac{2\pi}{\lambda(d_i-f)}(x_f x_i + y_f y_i)} dx_f dy_f. \tag{5.19}$$

Where G is a quadratic phase term given by:

$$G(x_f, y_f) = e^{j\frac{\pi}{\lambda(d_i-f)}(x_f^2+y_f^2)}. \tag{5.20}$$

We now use the paraxial imaging condition $1/d_o + 1/d_i = 1/f$ and the magnification $M = d_i/d_o$ and substitute Eq. (5.17) in Eq. (5.19). This yields Eq. (5.1):

$$E_i(x_i, y_i) = e^{j\frac{\pi}{\lambda(d_i-f)}(x_i^2+y_i^2)} \left(H(x_i, y_i) \otimes E_o\left(-\frac{x_i}{M}, -\frac{y_i}{M}\right)\right). \tag{5.21}$$

Where H is the Fourier transform of the aperture stop A:

$$H_i(x_i, y_i) = \iint_{-\infty}^{\infty} A(x_f, y_f) e^{-j\frac{2\pi}{\lambda(d_i-f)}(x_f x_i + y_f y_i)} dx_f dy_f. \tag{5.22}$$

Chapter 6

Pupil Apodization in Digital Holographic Microscopy for Reduction of Coherent Imaging Effects

A dark-field Digital Holographic Microscope with a single lens for imaging is a potential candidate for future overlay metrology on semiconductor wafers. Aberrations caused by this single lens are computationally corrected allowing high-resolution imaging over a large wavelength range. However, the spatially-coherent imaging conditions in our microscope introduce coherent imaging artifacts that can limit the metrology performance. In this chapter we present computational apodization of the optical field in the exit pupil of the lens as a potentially effective solution to mitigate these coherent imaging effects. A comparison of experimental data and simulations is presented that demonstrates the importance of this apodization in metrology applications. Moreover, our data also shows that exploiting the full potential of DHM requires an imaging lens with low optical scattering levels.

The content of this chapter has been published in: Christos Messinis, Manashee Adhikary, Tamar Cromwijk, Theodorus T.M. van Schaijk, Stefan Witte, Johannes F. de Boer, and Arie den Boef, *Pupil Apodization in Digital Holographic Microscopy for Reduction of Coherent Imaging Effects,* Optics Continuum **1**, 1202-1217 (10 May 2022).

6.1 Introduction

Digital Holographic Microscopy (DHM) is a well-known and established technique for high resolution imaging in various application domains like bio-medical imaging and semiconductor defect inspection [26, 27, 122, 123]. DHM acquires the amplitude and phase of an image which offers various unique opportunities like (3D) imaging of low-contrast objects and digital aberration correction [56, 124]. Recently we have reported the use of dark-field DHM (df-DHM) as a potential solution for the growing challenges of overlay (OV) metrology in semiconductor industry [110, 125].

In semiconductor device manufacturing the relative placement between various patterned layers in a chip (called Overlay) must be robustly measured with sub-nanometer precision. This measurement can, for example, be done with a technique called Diffraction Based Overlay (DBO) [3]. In DBO a pair of small overlapping gratings is illuminated resulting in the generation of a $+1^{st}$ and a -1^{st} diffraction order. An overlay error between these overlapping gratings creates a small intensity difference between these orders, which scales linearly with overlay. Today, high-resolution dark-field microscopy is commonly used to image the $+1^{st}$ and -1^{st} diffraction order images of the metrology targets on a camera and these images are used to determine overlay. Robustness and sub-nm accuracy is possible by optimizing the grating etch and using carefully selected multiple wavelengths [112].

However, the relentless push to follow Moores law [2] drives existing optical overlay metrology to the extreme limits of its capabilities. Novel devices and process flows result in the use of new materials (like amorphous carbon) that are highly absorbing at visible wavelengths but sufficiently transparent at infrared wavelengths. This drives the need for metrology tools that can cover a larger wavelength range. In addition, there is a strong push to reduce the size of the metrology targets that requires improved imaging resolution. On top of this, the diffraction efficiency of metrology targets continues to decrease to unprecedented low levels due to thin resist that is used in (high-NA) EUV lithography and increased light losses in the stack of layers that cover the bottom grating. Last but not least, a solution for all these challenges needs to be realized at acceptable cost and in a small footprint since available space for metrology is limited.

A promising solution to all these challenges is dark-field Digital Holographic Microscopy (df-DHM). We have already presented the operation of df-DHM that uses a tunable quasi-monochromatic spatially coherent light source. The use of 2 off-axis reference beams with different azimuthal angles allows angular frequency multiplexing, enabling the separate imaging of the $+1^{st}$ and -1^{st} diffraction orders using the full NA of the imaging lens which improves imaging resolution. A schematic drawing of df-DHM is shown in Fig. 6.1. The off-axis df-DHM setup uses a fiber coupled Supercontinuum White light source (Leukos Rock 400 5) combined with an Acousto-Optical Tunable Filter (Gooch & Housego TF550-300-4-6-GH57A). This AOTF device has a bandwidth in the range of 47 nm and covers the whole visible wavelength range from 400 to 700 nm. A delay line is used to match the optical path of the reference and the illumination beam and

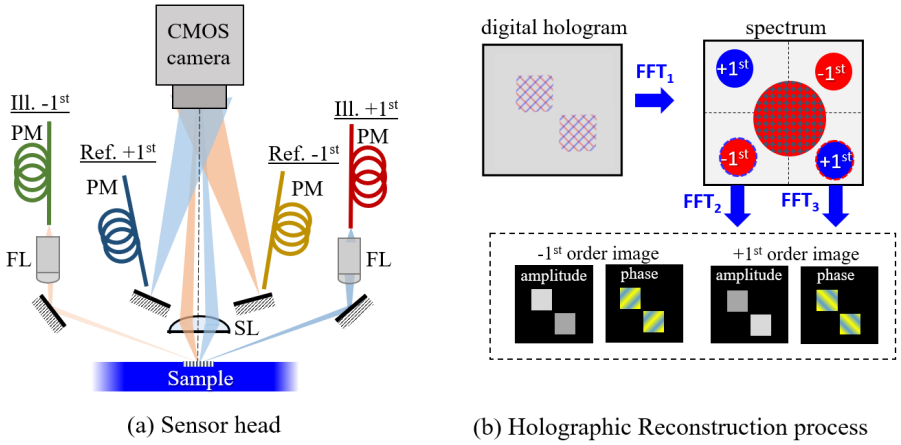

(a) Sensor head

(b) Holographic Reconstruction process

Figure 6.1: (a) the fiber-coupled df-DHM. The sample is illuminated with two oblique illumination beams (Ill.$+1^{st}$ and Ill.-1^{st}) of $\pm$ 70° respectively. The object beams are captured by the imaging lens (SL) and coherently mixed with their respective reference beams (Ref.$+1^{st}$ and Ref.-1^{st}) resulting in a hologram on image plane (CMOS camera). (b) the holographic reconstruction process. The camera image contains two interference patterns initially introduced by the two separate branches. By Fourier transforming the hologram we back-propagate to the pupil plane and the angular spectrum. The illumination branches have different azimuthal angles in the reference arms resulting in a 90° angle difference. For reconstruction of the complex field two Fast Fourier Transforms for the two interference terms are required.

polarization maintaining fibers (PM - Shafter-Kirchhoff PMC-400Si-2.3-NA014) are used to couple the light from the source path to the sensor head. The sensor head is comprised of two off-axis illumination arms which illuminate the target from opposite directions at an incident angle of approximately 70° with respect to the normal of the object plane.

For DBO measurements the two sides generate the -1^{st} (L. Arm) and $+1^{st}$ (R. Arm) diffraction orders. Each illumination arm generates a Gaussian-shaped spot on the object plane ($1/e^2$ diameter approximately 130 µm) with the use of two microscope objectives (FL- 50X Mitutoyo Plan Apo Infinity Corrected Long WD Objective) and two adjustable mirrors for fine-tuning the angle of incidence. In addition, two corresponding spherical reference beams are coherently added to the corresponding object beams. The two reference beams have different azimuthal angles resulting in a different orientation of the sidebands of the spectra of the resulting holograms. With this approach, two holograms are captured by the image sensor using only one image acquisition, and the two object fields can be retrieved with only three Fast Fourier Transforms (FFTs). Further details of this setup and the parallel acquisition of multiple holograms are given in Ch. 2 and Ch. 5. The microscope consists of a single plano-aspheric Thorlabs lens (SL) and a camera (Basler acA4112-8gm) with a 12 Mpixel CMOS image sensor with 3.45 µm pixel size. We chose a nominal magnification of 100x by placing our detector

800 mm away from the lens.

It is worth mentioning that the coherent mixing of the diffracted orders with their respective reference beams offers noiseless optical amplification which lifts the image above the noise floor of the image sensor and boosts the detection sensitivity of very weak metrology targets. This has already been demonstrated in Ch. 4 and [125], where a weak measured signal of a silicon wafer at 1030 nm wavelength is coherently mixed with a reference beam resulting in a "noise clean" amplified holographic image. Finally, the retrieved complex field in DHM allows us to computationally correct for aberrations in the imaging lens, as shown in Ch. 5 and [106]. A single imaging lens might seem undesired as it adds a quadratic wavefront to the complex image on the camera, but it is required as it enables imaging on a larger wavelength range. We eliminate this quadratic term by introducing a spherical reference beam that is propagated from the tip of a fiber placed in the pupil plane of the imaging lens.

However, our df-DHM concept operates in a spatially coherent imaging regime [23]. As a result, the Coherent Transfer Function of our df-DHM creates oscillatory edge transitions in the retrieved images (as shown in Fig. 6.2) that are undesired for metrology applications. In the next section (6.2) we will briefly explain the impact of coherent imaging conditions in metrology applications, present digital pupil apodization as an effective solution and compare various implementations. Section 6.3 presents simulations and measurements on actual metrology targets along with point-spread functions (PSFs) for a better evaluation of the use of this method. Section 6.4 discusses the effectiveness of pupil apodization for metrology applications and the potential limitations and section 6.5 concludes the paper with an outline of the following steps that we plan to take to improve overlay metrology.

6.2 Theory

6.2.1 Coherent Imaging Effects in DHM

We use DHM that requires a spatially coherent quasi-monochromatic illumination to enable interference between reference and object beam. This requirement also introduces inherent coherent imaging effects in the reconstructed images. In earlier work, the use of low spatial coherent sources [126–128], multiplexing holograms methods [129–131], image processing methods [132, 133], and hybrid methods [134, 135] have been studied to improve the imaging quality. In our investigation, we look into a hybrid method of the use of a super continuum source combined with image processing method for coherent imaging effects reduction. But by definition, a super continuum source, even with low temporal coherence, introduces coherent effects to the holographic imaging, causing reduction of the sharpness of the reconstructed image and further degrading the imaging quality.

The coherent imaging effects that we can expect in our df-DHM will show up as:

1. Ringing effects at edges due to the steep cut-off of the Coherent Transfer

Function

2. Increased optical crosstalk (X-talk) between neighboring patterns

3. Speckle (in case of rough surfaces)

In the numerical reconstruction of a hologram the commonly applied two-dimensional Discrete Fourier Transform (2D DFT) method on the pupil plane introduces Gibbs-ringing. This ringing effect is due to the presence of a sharp cut-off in the pupil plane that is forward-propagated to the image. Gibbs-ringing is a common artifact caused by the finite k-space sampling and is the effect of the truncation of higher frequencies at the sampling borders [136]. This shows up as spurious oscillations in the vicinity of high frequency region like the edges of a metrology target, as shown in Fig. 6.2. This phenomenom is more clearly present on the smallest metrology targets and remains even after aberration correction. As a result, these oscillations can degrade not only the quality of the images but also impact the metrology results obtained with df-DHM.

Gibbs-ringing is present mainly at the edges of a structure but it also expands in every direction. This means that the spurious oscillations can affect nearby structures also and result in additional coherent imaging effects with an overlap of high frequencies of different structure in k-space. This crosstalk should be minimized to allow precise metrology on targets that are surrounded by other patterns. This is an effect that becomes more visible for smaller metrology targets, and hence the higher frequencies are enlarged resulting in light leakage from one structure to a neighbouring structure.

Speckle is another undesired coherent imaging effect and it can generally be found in both reflection and transmission DHM. In reflection configuration, grain speckle occurs when the reflected light irradiates the sample surface. At the same time in both configurations non-diffusing objects can cause undesired diffraction, like dust particles, scratches, and defects on and in the optical components of the setup. Since our df-DHM concept is intended for high end semiconductor wafers we do not expect significant speckle noise originated from the wafer but we will show that in our df-DHM setup, weak scattering from the imaging lens can add a small amount of speckle to our measurements.

Fig. 6.2 shows the coherent imaging effects that are currently present in our measured df-images. We selected a micro-DBO (µDBO) metrology target with 8 x 8 μm^2 grating size that consists of four grating pairs with a grating pitch of 600 nm. Two of these grating pairs run in the vertical direction and are used to measure overlay in the horizontal direction, the other two grating pairs are used to measure overlay in the vertical direction but since we illuminate the sample from the horizontal direction they are not visible on a measured df-image. These grating pairs can potentially add coherent imaging effects in the measurements.

Figs. 6.2.(a) and 6.2.(b) shows the presence of coherent effects on an aberration corrected dark-field intensity image in both linear and logarithmic scale. The selected wavelength for this measurement was 576 nm with a bandwidth of 5 nm. In more details, in linear scale we can already detect the spurious oscillations within the metrology marks. And in logarithmic scale it is revealed that ringing

and cross talk from y grating marks are also affecting the metrology marks. Finally, some dust particles that are located around the targets increase the speckle noise on our measurements. This is mostly visible in the logarithmic scale of the df-images.

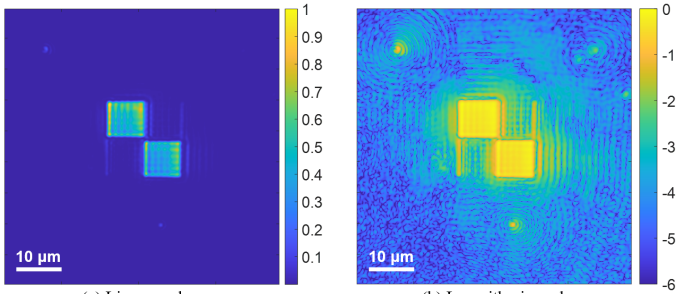

(a) Linear scale (b) Logarithmic scale

Figure 6.2: Coherent imaging effects on our df-DHM. A metrology target's normalized intensity is imaged in (a) linear scale and (b) logarithmic scale.

In previous publications we have described the numerical reconstruction process of df-DHM. In essence, we apply a 2D Fourier Transform (FT) to the detected image and assume an infinite plane wave reference beam. As shown in Fig. 6.1(b) we obtain the spatial frequency spectrum in k-space where we select the cross-correlation terms that describe the interference between the object and reference beam. Then we select the proper sideband with a computational aperture stop that is centered around the sideband and we shift this sideband to the origin of the k-space. Applying an inverse FFT finally yields the complex image field.

Using the plane wave propagation model for a single-lens imaging system as described by Goodman in [23] we can show that the complex field E_i in image plane is given by Eq. (5.1) [106]:

$$E_i(x_i, y_i) = e^{j\frac{\pi}{\lambda(d_i - f)}(x_i^2 + y_i^2)} \left(E_o\left(-\frac{x_i}{M}, -\frac{y_i}{M}\right) \otimes H(x_i, y_i) \right), \tag{6.1}$$

where $E_o(-\frac{x_i}{M}, -\frac{y_i}{M})$ is the complex field in the object plane and M is the magnification. The quadratic phase term in Eq. (6.1) has a radius of curvature $d_i - f$ where d_i is the image distance and f is the focal length of the lens. $\otimes$ denotes a convolution and $H(x_i, y_i)$ is the Fourier transform of the aperture stop in the back focal plane of the lens. H is the coherent transfer function (CTF) of this single-lens imaging system and is the Fourier transform of the aperture stop A, given by:

$$H_i(x_i, y_i) = \iint_{-\infty}^{\infty} A(x_f, y_f) e^{-j\frac{2\pi}{\lambda(d_i - f)}(x_f x_i + y_f y_i)} dx_f dy_f. \tag{6.2}$$

This filtering procedure implicitly assumes that the Fourier transform is zero everywhere outside the sampled region. This is not the case for finite objects. Setting this null space to zero is a simple and convenient solution, however, the

procedure corresponds to a multiplication of the true objects Fourier transform with a hard-stop in image space, which in our case is a circle. This results in a convolution of the true object with the Airy function which adds coherent artifacts in our retrieved images that we plan to solve with digital pupil apodization.

6.2.2 Digital Pupil Apodization

To correct for these coherent imaging effects a manipulation of the pupil image is required. Earlier we mentioned the multiplexing holograms methods and the image processing methods. With df-DHM we can explore all known methods for noise suppression, but we will focus on the use of window functions during the reconstruction process.

With apodization we can either apodize the hologram in the image plane [137] or in the pupil plane [138] to mainly reduce the diffraction during the numerical reconstruction. Apodization functions can suppress the side lobes of the Airy disk which effectively suppresses ringing effects at object edges at the expense of some loss in resolution. For our investigation we will use cosine-sum window functions that will moderate the effect of the CTF and reduce crosstalk noise by smoothing the higher frequencies of the measured holograms.

The selection of these windows came after the justification made already back in the 70s by Fredric J. Harris [139]. In his work, Harris categorized the numerous window functions based on their significant use and distinct parameters. Starting from the classical rectangle (or Dirichlet) and triangle (or Bartlet) windows, he concluded that windows that are constructed with 3 or 4 nonzero terms (or Dirichlet kernels) can be used for side-lobe suppression.

In this work, we will focus on these window functions as the coefficients are easy to generate and of being able to be applied as a spectral convolution after the 2D DFT. Blackman and the Blackman-Harris windows that are constructed as the summation of 3 and 4 shifted Dirichlet kernels respectively. These window functions are zero-valued outside of a chosen interval, normally symmetric around the middle of the interval, usually near a maximum in the middle, and tapering away from the middle. For our investigation we assume an amplitude apodization that varies in the radial direction in the pupil plane according to the following cosine-series:

$$\mathrm{win}(\rho) = \sum_{n=0}^{N} \alpha_n cos\left(\pi n \rho\right), \tag{6.3}$$

where n are integers of the 2D sum of cosine windows and α_n are the window coefficients which are constrained to a sum of unity. In the simplest case of a rectangular window ($\mathrm{win}(\rho) = 1$) only the first coefficient $\alpha_0 = 1$ is needed, thus a cosine function. To apply this equation to our measured holograms, ρ is the normalized radial position in the pupil plane and is equal to:

$$\rho = \frac{1}{\left|\vec{k}\right|}\sqrt{k_x^2 + k_y^2}, \tag{6.4}$$

k_x, k_y are the k space coordinates that can take values up to the edge of the pupil where we have the maximum spatial frequency of $\mathrm{NA_{obj}}/\lambda$. Here λ is the wavelength and $\mathrm{NA_{obj}}$ is the Numerical Aperture of the imaging lens ($\mathrm{NA_{obj}} = 0.5$). We set the size of the apodization window less or equal to $\mathrm{NA_{obj}}$ or the boundaries of the cross-correlation term in which we apply the apodization window.

Instead of digital apodization it is also possible to use moving sub-apertures for reducing coherent imaging effects. Similar to the classical physical manipulation of the pupil [140], we can digitally select a smaller window size and apply it on different parts of the pupil image [141]. At the end we take the summation of the intensities of the different reconstructed windows and obtain a noise suppressed df-image. This approach requires multiple holographic reconstructions and thus more time even if it is single shot, and since we need to have a fast numerical reconstruction we will limit our investigation to the use of a single apodized window function in the pupil.

Figure 6.3 shows the suppression of the side lobes of the PSF for various pupil apodization windows. A first comparison of the different window functions shows that there is a trade-off between width of the side lobe, which determines the resolution, and the suppresion of the side lobes, which determines optical crosstalk between neighbouring structures in an image.

The simulated window functions show that in practice if resolution is not a critical requirement and the application is focused on the coherent effect suppression, the best window functions are the hybrid Blackman windows, and especially the Blackman - Harris, the Blackman - Nuttal and the Nuttal window. On the contrary, if the resolution is important Hamming and Hann windows offer sufficient resolution with less noise suppression. In literature different hybrid window functions have been reported [142] in search for the optimum window that offers almost diffraction limited resolution with maximum noise suppression. In this work we will focus on the Blackman window as it offers sufficient resolution and suppresses the noise to the required noise levels for metrology.

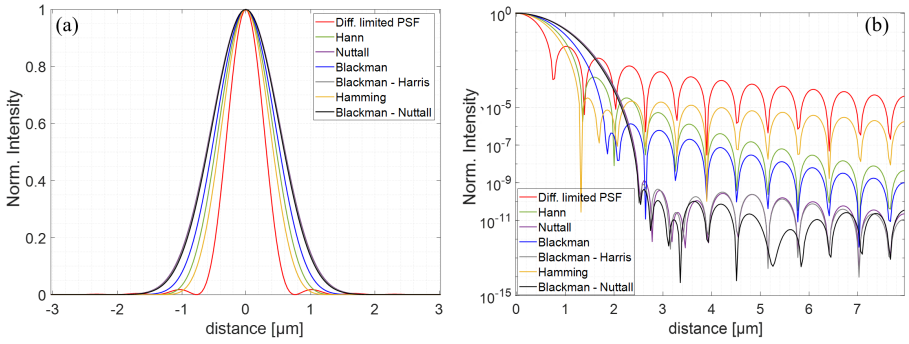

Figure 6.3: Theoretical influence of apodization window functions on an ideal PSF. A cross section of normalized intensity image, (a) linear scale, (b) logarithmic scale.

In Ch. 5 we presented an aberration calibration procedure in which we retrieve

the wavefront error of our imaging system by measuring the PSF using a point scatterer. Then we only needed to include an aberration correction step on our filtering procedure and obtain an aberration-corrected hologram. We corrected for lens aberrations by multiplying the complex field in the pupil plane with the phase conjugate of the retrieved wavefront error. With the same reasoning we will also perform apodization digitally in the pupil image. This removes the sharp cut-off of the spatial frequency spectrum in the pupil plane resulting in a strong suppression of the side lobes of the PSF. This will suppress optical crosstalk from neighbouring structures that surround a metrology target. The lens aberration correction and the implementation of the window function are then given by:

$$E_{f_{\text{apo}}}(x_f, y_f) = E_f(x_f, y_f)e^{-jW(x_f,y_f)}\text{win}(x_f, y_f). \tag{6.5}$$

Where $E_{f_{\text{apo}}}(x_f, y_f)$ is the corrected field in the exit pupil. In the following section, we apply this concept to both simulations and measurements of PSFs obtained with our df-DHM.

6.3 Experimental results on coherent imaging effects suppression

6.3.1 Measurements and simulations on PSF

To investigate the effect of digital apodization on the coherent image quality of metrology targets we start with the characterization of the diffraction-limited point-spread function (PSF). The PSF is the usual way to characterize an optical imaging system, and the proper way to demonstrate the effect of apodization through the side-lobes suppression and the loss of resolution. A point source illuminates the lens aperture with a spherical wave that is insensitive to non-uniformity in the illumination beam. For the measurement we used a bare silicon sample with drilled nano-holes in different parts of the sample. These nano-hole were milled with a 30 keV focused gallium ion beam (FEI Helios Nanolab 600). The ion beam current was set to 100 pA with a focal spot diameter of 80 nm. The nano-holes were milled in 500 cycles and with a dwell time of 1 ms. The diameter of the nano-holes is approximately 80 nm.

The point scatterer was placed in the center of the image field of our DHM setup. Aberration correction was applied to the PSF by applying a wavefront correction to the field in the exit pupil of the lens. The wavefront correction was derived from a Zernike fit of the measured wavefront using the lowest 83 Zernike polynomials. In this way the PSF is only affected by the small residual wavefront errors that could not be captured by the Zernike fit.

For the simulations of the PSF we used the same wavelength, bandwidth and Field of view as the ones that we used for the measurements so that we will have a good comparison between the measurements and the simulations. For the comparison of Fig. 6.4 we selected a 576 nm wavelength with a bandwidth of 5 nm. At the same time we have included additional shot noise and read-out noise

for a better representation of actual measurement conditions. The comparison of simulated and measured PSFs is presented in Fig. 6.4

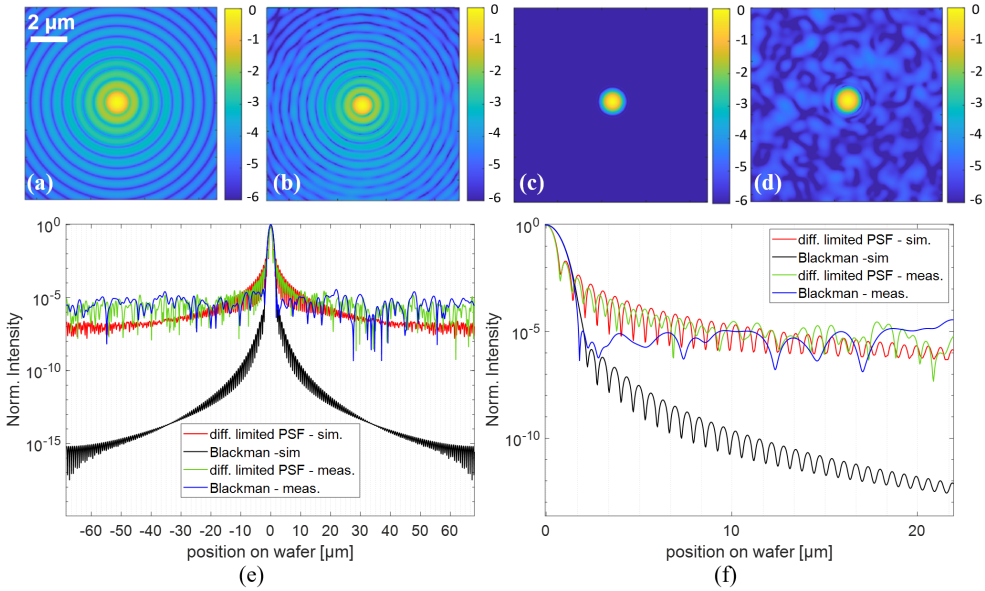

Figure 6.4: Comparison of simulated and measured PSFs. (a) simulated Airy disk, (b) measured Airy disk, (c) simulated apodization with Blackman window, (d) measured apodization with Blackman window. (e) presents the cross-section of the above images in logarithmic scale, and (f) provides a closer look on the response in the 4 different cases.

From this comparison we observe that the measured unapodized PSF and the PSF after apodization with a Blackman window could not surpass a noise flour of the order of 10^{-6} (or -60 dB), as shown in Fig. 6.4(e). On the other hand, we observe that the simulated PSFs show excellent sidelobe suppression after apodization. At a closer look to the center of the Airy disk and the apodized PSF, we see that there is a good correlation between the simulations and the measurements, Fig 6.4(f). At this point and for noise levels above 10^{-5} we see that the simulated and the measured diffraction-limited PSFs are overlapping while in the contrary the apodization windows reach this noise level immediately after the 1^{st} Airy ring.

The flattening of the noise shows that the use of apodization windows does not offer sufficient coherent imaging effects suppression in our DHM setup. In that sense while apodization can assist with the crosstalk reduction and reduction of the ringing effects in the region-of-interest in the metrology target area, it will still lead to a noise suppression at 10^{-5} noise levels. In the next section, we will present the experimental data from which we were able to locate the cause of the observed noise floor.

6.3.2 Effectiveness of apodization and potential limitations

In order to investigate the cause of the noise flattening on the experimental data we look into three potential noise sources that could contribute to this effect:

1. Roughness of the silicon wafer
2. Detection noise
3. Scattering from lens imperfections

1. Roughness of the silicon wafer

Starting with the roughness of the silicon wafer, an Atomic Force Microscopy scan of the roughness showed a root-mean-square (RMS) error of 142 pm and maximum peak-to-valley of 2.3 nm during the scan. These values suggest that the sample was very smooth and is probably not introducing speckle to our measurements. A simple method to check the presence of speckle coming from the wafer is to compare the high-frequency residual wavefront variations in the exit pupil of our imaging lens for different nano-holes. If the roughness of the silicon dominates the noise floor that is shown in Fig. 6.4 then this should show up as noise in the wavefront residual in the exit pupil. The fingerprint of this noise in the wavefront residual should then vary between different nano-hole measurements. In other words, the wavefront residuals measured for two nanoholes should show little or no correlation.

To experimentally test this hypothesis we have selected two nano-holes with approximately the same size (measured with AFM). For these 2 nano-holes we measured the WFE (Fig. 6.5(a) and 6.5(d)) in the pupil and we subtracted a fitted wavefront (using the lowest 83 Zernike polynomials). The resulting residual WFEs of the 2 nano-holes show high-frequency variations that are shown in Fig. 6.5(c) and 6.5(f). The two locations have a clear speckle correlation which suggests that surface roughness of the silicon substrate does not contribute significantly to the high-frequency speckle-like wavefront variations. The measured correlation was 0.8130 with a deviation that can be contributed to additional noise on the second PSF. As shown in Fig. 6.5(d), there is a phase gradient present in the measured WFE, which is attributed to a nearby nano-hole that introduced additional scattering to the measured wavefront.

2. Impact of detection noise

The detected digital hologram contains shot noise that is inherent to the detection of photons. Moreover, the image sensor also adds some read noise to this shot noise. In order to test the impact of these noise sources we performed a frame averaging on the same PSF.

Fig. 6.6 presents a comparison of the measured PSF in a single holographic reconstruction and after 150x reconstructions. It is clear that after frame averaging there is no improvement with respect to the noise levels, meaning that our measurements are not limited by shot noise and image sensor read noise. In

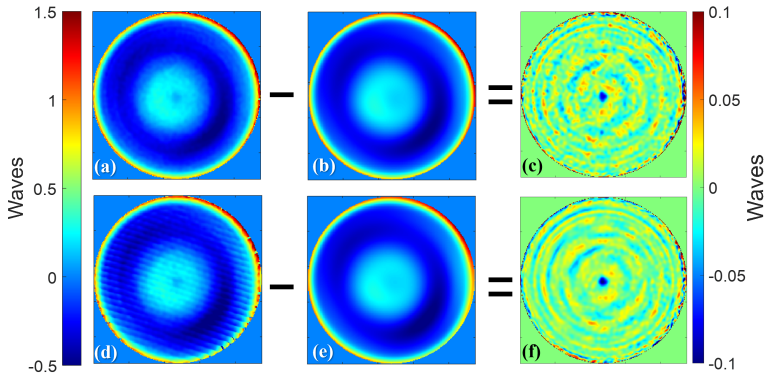

Figure 6.5: Residual wavefront errors for two PSFs. (a), (d) are the measured WFEs and (b),(e) are the fitted aberration terms. (c) and (f) presents the residual wavefront errors for the two PSFs simple by removing the fitted wavefronts from the measured ones.

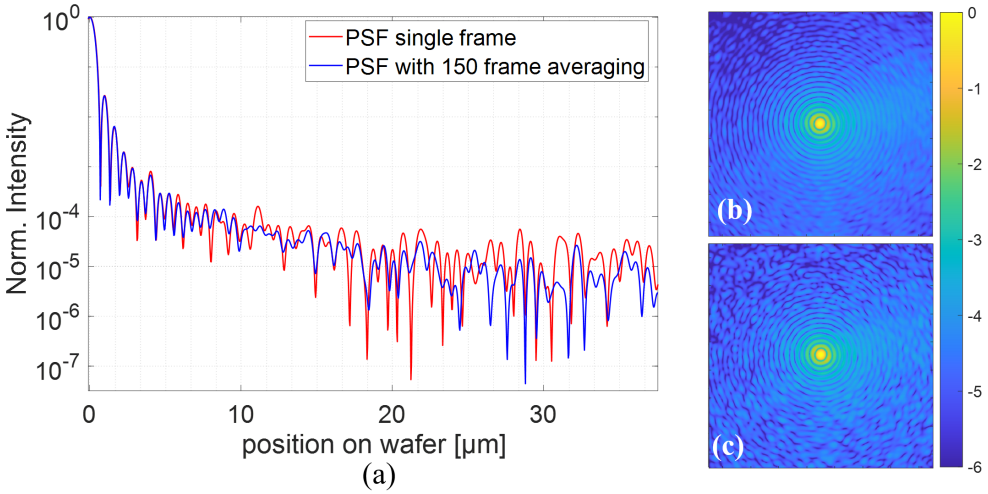

Figure 6.6: (a) Cross-section of the normalized intensity of a PSF measured with and without frame averaging. (b) and (c) The single-frame measured PSF and the same PSF after 150 frames averaging. Both figures presented in logarithmic scale.

principle, in holography this is expected due to coherent amplification. Even if the object beam is weak, in our case the PSF, it is coherently amplified by the reference beam.

3. Scattering from lens imperfections

Our df-DHM uses an off-the-shelf plano-aspheric lens (Thorlabs A240TM) with an effective focal length of 8 mm and an NA of 0.5. Because of the extreme level of aberrations on the edges of the used lens, we have selected a digital aperture stop of 0.48. According to the data supplied by Thorlabs, we should expect a root-mean-square (RMS) wavefront error (WFE) of 0.058 waves. As a result of this residual wavefront error, some weak scattering will occur at the lens surfaces which results in a weak speckle background in the retrieved images.

A simple method to check the presence of lens-induced light scattering is to look at high-frequency residual wavefront variations in the exit pupil of our Thorlabs A240TM imaging lens. Similarly to what we presented in Fig. 6.5, in the case of scattering from the lens, we will measure the same PSF for three different wavelengths. As a result of the close proximity of the exit pupil to the lens this residual WFE will be more or less invariant for small wavelength changes.

To measure this correlation we retrieved the complex WFE for three closely spaced wavelengths (532, 550 and 576 nm) and then removed a fitted wavefront that we obtained by fitting the lowest 83 Zernike polynomials to the measured wavefront. We can then measure the residual phase variation in the pupil. If the residual phase variation or the residual WFE of the PSF show significant correlation for different wavelengths then this is another indication that light scattering from the lens is the main cause of the observed speckle.

Figure 6.7, presents the residual wavefront errors that we obtained by measuring the PSF at three different wavelengths. For every wavelength (532, 550 and 576 nm) we remove the fitted aberrations terms from the retrieved WFE and we plot the residual WFE. As shown all graphs show a clear correlation of the residual WFE which is a very strong indication that our measurements are impacted by the roughness of the lens surface. To measure the correlation coefficient for different wavelengths we had to resize the measured WFE as the size of the sideband in the angular spectrum is wavelength dependent (eq. 6.5). We resize the WFE with respect to the middle wavelength and we measured correlations above 0.75. In details, the correlation between 6.7.(a) and 6.7.(b) was 0.7678, between 6.7.(a) and 6.7.(c) was 0.8018 and between 6.7.(b) and 6.7.(c) 0.7805.

Moreover, we computed the RMS error for the three wavelengths and it was 0.0510, 0.0560 and 0.0516 waves respectively which is close to the expected wavefront error that has been specified by the supplier of this lens. This is another clear indication that scattering caused by the lens is the main cause for the speckle background that we observe in our images.

For the three wavelengths there is some additional noise present in the edges of the pupil which is more visible on the shorter wavelengths and on the right side. This additional WFE could be related to the size of the aperture stop in the pupil which we considered fixed for an NA of 0.48 or it can be an error during the filtering of the holographic process that we neglected for the time being.

In order to further substantiate our observation we performed a second experiment where we replaced the sample with the tip of a single-mode fiber. We used a polarization maintaining PANDA fiber (Schafter Kirchhof - PMC-E-400Si-3.5-

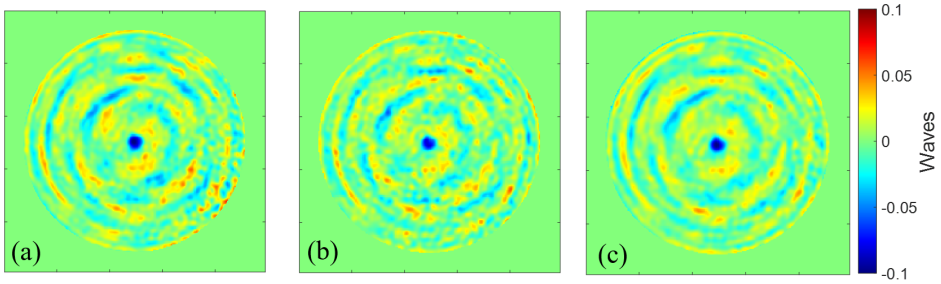

Figure 6.7: Lens surface roughness. Residual Wavefront Error experiment. (a),(b),(c) the RWE for the measured PSF for 532, 550 and 576 nm wavelength respectively.

NA013-3-APC.EC-150-P) with Nominal NA of 0.13 and a mode field diameter (MFD) of 3.5 µm . The use of a fiber tip to measure the PSF has already been reported by [114] and it allows us to exclude the impact of any scattering from the silicon substrate that we used for the previous experiments. However in our experiment due to the small NA of the fiber, which at a 520 - 580 nm wavelength range is ≈ 0.08, instead of an Airy disk, df-DHM will image a Gaussian spot.

For the measurements with the fiber tip we selected three different wavelengths (532, 550 and 576 nm) and we look into the speckle correlation on the reconstructed images. Fig. 8 summarize the measurements with the fiber tip. Fig. 6.8(a),(b) and (c) show the normalized intensity images of the holographically reconstructed Gaussian spot of the fiber tip for the three selected wavelengths in logarithmic scale. For these measurements we have averaged 100x reconstructed images.

A cross-section plot of the measured normalized intensity in Fig. 6.8(d) shows that for all the wavelengths the noise levels are of the same order. Looking at the speckle correlation between different wavelengths, it is clear that there is no correlation between the three measurements. To confirm that we have also measured the correlation coefficients between (a),(b) and (c) within the drawn squares and the correlation was below 10%. The absence of correlation between the three measured signals again points to lens scattering as the main suspect for the observed speckle in our images.

At this point, it is good to highlight that the speckle that we measured with DHM was impossible to detect with regular imaging of the fiber-tip. We have performed the same measurements without additional reference beams and look into the measured normalized intensities of the 3 different wavelengths after averaging 100 images. Fig. 6.9(a),(b) and (c) show the normalized intensity images of the Gaussian spot of the fiber tip for the three selected wavelengths in logarithmic scale. A cross-section plot of the measured normalized intensity in Fig. 6.9(d) confirms that in regular imaging the measurements are buried in the read out noise and corresponds to a lower noise suppression, making it impossible to detect speckle. This clearly shows the superior dynamic range capabilities of DHM compared to regular imaging techniques.

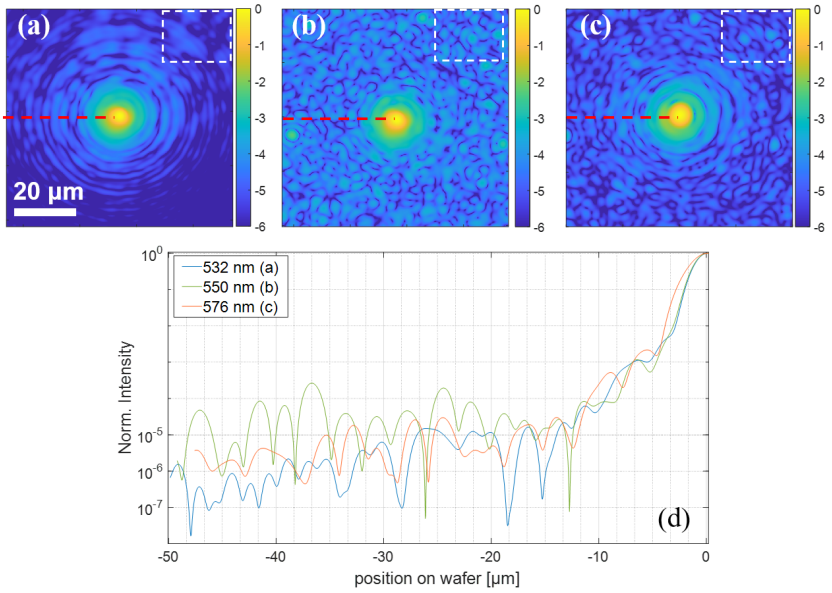

Figure 6.8: Fiber-tip experiment. (a),(b) and (c) are the holographically reconstructed intensity images of the fiber tip for 532, 550 and 576 nm wavelength respectively. (d) Logarithmic plot of the cross-section (as indicated with the red dotted line) of the normalized intensities of the measured Gaussian spots.

In the next subsection, we apply digital apodization on actual metrology targets. We will show that even with the presence of micro-speckle from the lens roughness apodization can still contribute to df-DHM by suppressing a large part of coherent imaging artifacts.

6.3.3 Measurements and simulations on metrology targets

Since we quantify the digital apodization response to a PSF, now we will apply apodization windows to metrology targets to see the response on coherent imaging effects suppression on measured holograms. We selected a micro-DBO (µDBO) metrology target with 8 x 8 µm^2 feature size that consists of four grating pairs with a grating pitch of 600 nm, like the one shown in Fig. 6.2.

We will first simulate the effect of apodization neglecting the effect of micro-speckle of the lens surface. With these simulations we can estimate the effectiveness of digital apodization on metrology targets on ideal conditions. Then we will present actual measurements where we will apply the same apodization window to see the coherent imaging effect suppression on the current setup. For both simulations and measurements we will use same setup parameters, with an NA of 0.48 and a selected wavelength of 576 nm.

For the simulations the same targets were simulated and the Blackman apodization window was applied. The results of the simulations are shown in

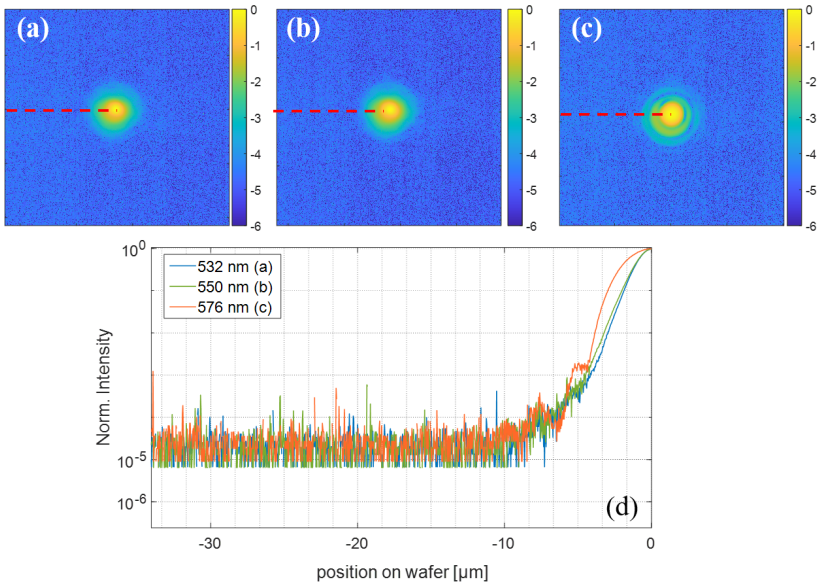

Figure 6.9: Fiber-tip experiment. (a),(b) and (c) are the normalized intensity images of the fiber tip for 532, 550 and 576 nm wavelength respectively. (d) Logarithmic plot of the cross-section (as indicated with the red dotted line) of the normalized intensities of the measured Gaussian spots.

Fig. 6.10. Fig. 6.10(a) and 6.10(b) show the simulated target on a regular image and an image where the Blackman window was applied on the pupil plane. Fig. 6.10(c) presents the cross section in logarithmic scale where the effectiveness of apodization is impressive. We can see at least a 10^{-5} coherent noise suppression and a smooth surface for the metrology mark, with no coherent artifacts present.

For the measurements of this metrology target we first correct for lens aberrations, in order to obtain an aberration free "regular" image and then we applied the Blackman window in the pupil plane. Figure 6.11 shows the effect of apodization on the metrology target on the current df-DHM setup. In the measurements we see that the intensity smoothens on the surface of the metrology target and completely suppresses Gibbs artifacts. At the same time multiple spurious oscillations on the surrounding area are also suppressed by an order of magnitude. This is still far from the ideal result that was presented on the simulations but it already convincingly shows a fast way to remove coherent imaging effects by applying a digital apodization in the pupil plane.

6.4 Conclusion

In this chapter we have investigated the potential of digital pupil apodization in DHM for coherent imaging effect suppression. We presented both simulations and measurements that demonstrate the simplicity of this method where a 2D

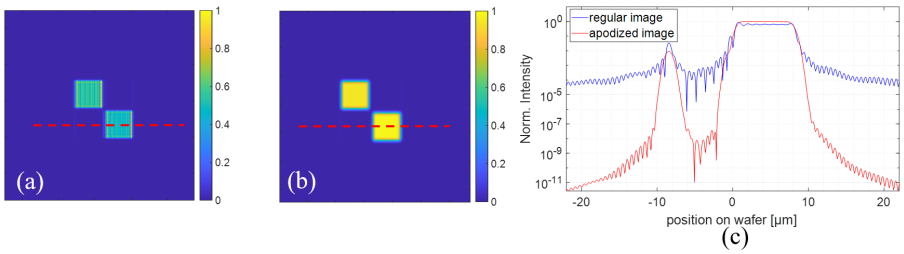

Figure 6.10: Simulated results of digital apodization on metrology targets. (a) a regular image obtained after holographic reconstruction, (b) apodized image with Blackman apodization window. (c) is the cross-section along the red-dashed lines, where blue and red lines show the normalized intensity of the regular and apodized image respectively.

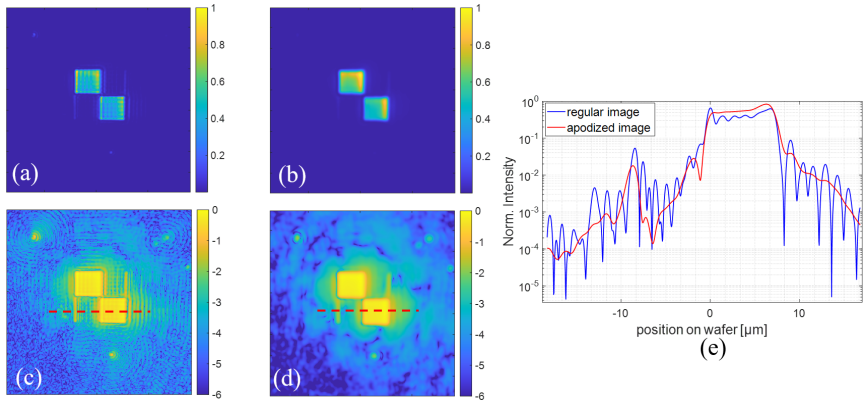

Figure 6.11: Experimental results of digital apodization on metrology targets. (a) a regular image obtained after holographic reconstruction, (b) apodized image with Blackman apodization window. (c), (d) regular and apodized image in logarithmic scale. (e) is the cross-section along the red-dashed lines, where blue and red lines show the normalized intensity of the regular and apodized image respectively.

window function needs to be included in the holographic reconstruction.

We have first applied apodization to diffraction limited PSF's ("Airy disks") to demonstrate the effectiveness on side lobe suppression. The results showed that apodization clearly suppresses side lobes of the Airy disc. This side lobe suppression helps to reduce optical crosstalk between images of neighbouring structures at the expense of some resolution loss. This is especially relevant in optical wafer metrology applications like overlay metrology where a small metrology target is often surrounded by other patterns. Light from these surrounding patterns that "leaks" into the metrology target resulting in a reduced metrology performance.

During our investigation we observed the presence of a weak background speckle in our PSF images that limited the effectiveness of apodization. By conducting a number of experiments we identified that the quality of the lens surface is the main factor of this deviation. The lens surface roughness adds

micro-speckle on the measurements which in extend create a noise barrier that prevents apodization to reach its full potential. The lens that we currently use is an off-the-shelf low-cost glass-moulded lens. We expect that more advanced lens manufacturing techniques will allow us to significantly reduce the noise floor that we now observe in our results.

However, the size of the window function can proven to be beneficial on higher diffraction order suppression. For example, in an overlay measurement where we look on the intensity imbalance between the $+1^{st}$ and -1^{st} diffraction order images there might be an overlap with a higher diffraction order in the image plane. This can be easily removed by carefully placing the window function in a smaller aperture size centered around the 1^{st} diffraction order in the pupil. This leaves the main frequency contributions of the higher order out of the reconstructed image.

This work has shown that df-DHM has the potential to be a powerful tool in optical wafer metrology provided that we can suppress the lens-induced light scattering to sufficiently low levels. Current measurements still show relatively large background noise levels, we plan to continue this investigation with a better lens quality which we are confident that will lead to robust coherent imaging effect suppression. This work also highlighted the excellent dynamic range of DHM compared to typical microscopy measurements. DHM was sensitive to the effect of lens roughness while a typical intensity image was buried in camera noise, unable to demonstrate this effect.

Chapter 7
Summary And Outlook

7.1 Summary

This thesis explores the potential use of dark-field Digital Holographic Microscopy (df-DHM) for advanced semiconductor overlay metrology. Theoretical analysis and experimental investigations have been performed to validate this potential and quantify to which extent it can be considered a promising technique for future overlay metrology tools. Semiconductor metrology is a very demanding field that constantly needs to innovate in order to cope with the challenging requirements from the semiconductor industry. Below is a summary of each chapter:

Ch. 2 This chapter presents details of our df-DHM concept. We show that angular frequency multiplexing allows us to acquire two off-axis holograms of the so-called $+1^{st}$ order and -1^{st} order images in parallel. This approach allows us to use the full NA of the imaging lens and the parallel acquisition also ensures immunity to intensity noise of the light source. In our df-DHM concept we have made specific design choices that result in significant application benefits, but that also creates specific challenges that we have investigated in more detail. For example, in our concept the light source is fiber-coupled to the microscope optics via single-mode fibers. This results in a very compact sensor head that enables high-speed metrology by putting multiple df-DHM sensor heads in parallel. However, during the first proof-of-concept overlay measurements we have discovered that the reproducibility of our overlay measurements were significantly degraded by instabilities in the single-mode fiber coupling efficiency. This is something that can be solved with a more stable opto-mechanical design.

Ch. 3 This chapter presents a theoretical model of the impact of coherence length on the Field-of-View in a dark-field digital holographic microscope. This model shows that the FoV is inversely proportional to the bandwidth of the light source. The presented model can be used to define requirements

of design parameters that ensure that the setup offers sufficient FoV for metrology. A test setup was presented to demonstrate the holographic reconstruction capabilities for both phase-shifting and off-axis measurements, with off-axis able to reach single shot acquisition.

Ch. 4 This chapter demonstrates the successful utilization of our df-DHM concept for measuring overlay over an extended wavelength range. Thus far, overlay measurements have been limited to visible wavelengths, but the use of materials that are opaque to visible wavelengths necessitates measurements using infrared light. We have constructed a breadboard test setup that is capable of measuring overlay at wavelengths ranging from 400 to 1600 nm. Using the setup, we demonstrated good correlation between programmed amount of overlay and measured overlay. These measurements constitute the first ever report of semiconductor metrology for this extended wavelength range with a single sensor. In addition, we demonstrated coherence gating offered a very effective suppression of undesired light that reached the sensor. This nicely demonstrate the viability of an overlay sensor that is sensitive to visible and infrared light, allowing more freedom in choice of materials for integrated circuits.

Ch. 5 In this chapter, an aberration calibration and correction method using nano-sized point scatterers on a silicon substrate is presented. Computational imaging techniques are used to recover the full wavefront error and we use this to correct for the lens aberrations, assuming isoplanatic imaging conditions. Measured data shows that point scatterers are very suitable for calibrating even large wavefront aberrations in Digital Holographic Microscopy. Although our setup still contained imperfections like a longitudinal offset of the reference fiber, we have been able to show convincing data of the aberration correction capabilities of our technique. Uncorrected images of metrology targets on a test wafer looked severely distorted but this image quality dramatically improved after applying an aberration correction. This calibration method is expected to perform well over a wide wavelength range, thus offering a lens calibration tool for the entire wavelength range. Finally, potential calibration error sources are presented to evaluate the performance of the presented method and offer an insight on the diffraction limited capabilities that can be reached with a simple lens.

Ch. 6 The final chapter of this thesis presents computational algorithms to mitigate effects that are inherent to the use of coherent illumination. The ultimate goal is to explore the overlay metrology capability of the df-DHM when the metrology targets are surrounded by other structures. In this case, the broad point-spread-function (PSF) in the presence of aberrations will lead to severe optical crosstalk from the surrounding structures to the metrology target and degrade metrology performance. The excellent aberration correction capabilities that we have demonstrated are expected to significantly reduce this optical crosstalk error but not yet on the required level. Optical crosstalk can be further reduced by additional digital

apodization that can suppress the sidelobes. With the addition of apodization on the measured PSFs we can significantly reduce coherent noise and reach better metrology performance. During this investigation, a deviation between simulations and experiments revealed that light scattering from lens imperfections (e.g. surface roughness) limited the effectiveness of apodization.

7.2 Outlook

The results that we have presented in this thesis are relevant for the semiconductor industry. Some of the main accomplishments are:

1. Feasibility and potential of dark-field digital holographic microscopy for semiconductor metrology.
2. The theoretical model and experimental demonstration verified the possible use of our df-DHM and lead to a US patent entitled Method of Determining a Characteristic of a Structure, and Metrology Apparatus with patent No. 11,119,415 B2 publication date: September 14, 2021.
3. Angular frequency multiplexed dark-field DHM with the ability of single shot measurement of two diffraction orders simultaneously. This project signifies the first OV measurements with df-DHM with sun-nm precision. This novel approach for measuring overlay with parallel acquisition of two diffraction orders lead to a WO patent application Dark Field Digital Holographic Microscope and Associated Metrology Method with patent No. 2021/121733 publication date: June 24, 2021.
4. The extended wavelength range from visible to infrared (400 - 1600 nm). This addition to df-DHM constitute the first ever report on an optical metrology tool that is capable to perform OVerlay metrology for this extended wavelength range with a single sensor.
5. The in-situ lens aberration calibration and correction. This project worked in parallel with the extension of the wavelength range since it allows df-DHM to collect highly aberrated images on wavelength far from the designed wavelength of the optical surface and then correct for the introduced aberration. This is a very important application that can be already applied to the next wafer fabrication loop. A section with some calibrating targets (like nano-hole arrays) can be used to offer field dependent aberration calibration for a large wavelength range.
6. The addition of digital filtering to optimize image quality. Since resolution is reaching diffraction-limited performance with the lens aberration calibration we needed to deal with the next challenge of coherent noise. With the nature of df-DHM this is a straightforward approach where every kind of digital filtering in the pupil image is possible and can correct for coherent artifact, and or suppress higher diffraction orders that in image plane overlaps with the desired measured intensities.

The progress and results that have been reported in this thesis is of interest for the semiconductor industry. However, despite the good progress several significant challenges still need to be solved before df-DHM can be used in an industrial environment. Solving these challenges are scientifically interesting problems with direct relevance for industry.

1. Illumination beam spot calibration and optimization. The illumination spot profile, for example, is a critical parameter in overlay metrology. An inhomogeneity of the illumination spot in combination with small positioning errors of the metrology target will change the diffracted optical power. This can give rise to significant errors in the measured overlay that exceed the required sub-nm precision levels. A next step in this investigation is therefore an accurate calibration of the complex illumination spot profile. This may appear simple but the accuracy needs to be in the sub-percent regime which makes this a daunting but not impossible task. Various techniques can be explored and compared like DHM, ptychography and Shack-Hartmann sensing. A related and equally interesting research challenge is how to correct for an inhomogeneous illumination spot. An overlay target is essentially a 3D-diffraction structure consisting of a top and a bottom grating and the total amount of diffracted 1^{st} order light is determined by a complex combination of the spot profile on the top target and the bottom target. Extensive research is still needed to tackle this challenge.

2. Field dependent aberration calibration. Aberrations of the imaging lens depend on the position in the field. So far we have only considered lens aberration in the center of the FoV, where for isoplanatic imaging conditions the PSF is invariant to a shift of the object and in that case a measurement of the complex PSF at 1 point in the field is sufficient to calibrate the aberrations in the imaging system. The df-DHM will introduce a high-end lens that was designed for this application with a higher NA of 0.8. To calibrate this lens it is a necessity to calibrate the field dependency of the aberrations of this lens. This will require additional computational algorithms that generate a shift-variant wavefront error that we could include on the calibration of the imaging lens.

3. Micro-speckle correction for noise suppression. In the course of our experiments with df-DHM we observed that due to the high dynamic range capabilities of the sensor, it was possible to detect residual noise on our measurements. This noise was due to micro-roughness of the lens. With access to the complex field we can apply computational algorithms to calibrate and correct for this micro-speckle.

4. Spectral shaping for crosstalk reduction. Our setup uses a super-continuum source that is combined with an acousto-optical tunable filter (AOTF). The AOTF is usually driven using a sinusoidal RF wave ($\leq$ 100 MHz). Such an AOTF allows a continuous tuning bandwidth of more than 2 um, with tuning speeds as low as 1 ms, thus allowing overlay measurements

over a wide bandwidth and with fast wavelength switching. In Chapter 3, we presented that the fringe contrast on the camera, and therefore the measured signal strength, is dependent on the optical path length difference between the illumination and reference beams, as well as the spectrum of the light. The fringe contrast around perfectly matched line delays of the object and the reference beam is typically the coherence function, This coherent function is expected to be a Gaussian-like function for an AOTF driven with a single RF tone. With spectral shaping we can potentially use multiple RF frequencies combined in order to re-shape the coherence functions and thus the fringe contrast in the image plane. In the ideal case, we could obtain a sinc-like spectrum, which will result in a coherence function with a sharp cut-off. Since df-DHM has this diagonal configuration for the two multiplex holograms, potential crosstalk from any off-diagonal structures is eliminated. In a more realistic approach we could apply spectra shaping to enhance the contrast on the desired FoV and suppress it on areas that nearby structures are located.

5. Control of polarization. In the course of our experiments we considered orthogonaly polarized light. This was mainly due to two factors. The AOTF required a polarized input and a better control of the fringe contrast between reference and object beam is obtained when they share the same polarization state. For metrology applications we need to investigate the effect of polarization on the accuracy and precision of df-DHM.

6. Mitigation of the vibration sensitivity. In Chapter 2, we have presented the benefit of the parallel acquisition regarding the noise fluctuations of the light source. However, during we have discovered that the reproducibility of our overlay measurements were significantly degraded by instabilities in the single-mode fiber coupling efficiency. This was mainly due to pointing fluctuation on the coupling to the fibers can be solved with a more stable opto-mechanical design. This is something that can be easily solved in a more industrial environment dedicated to high standards of performance.

7. Exploitation of the UV range for metrology. A new direction of df-DHM would be the extension to the UV wavelength range. This can open up a new range of metrology applications that df-DHM can thrive.

8. 3D imaging with dark-field DHM. The df-DHM so far demonstrated excellent performance in overlay metrology of thin 3D structures ($\approx$ 700 nm) that consisted of a few layers. A next step is to demonstrate the ability to reconstruct complex 3D structures, such as 3D MEMS with thicknesses that can reach 1 mm. And then use such measurements for even more advanced metrology application.

As it is perceived, with this thesis we have only hit the tip of the iceberg. There are still many improvements that can be made to improve the performance and enhance the capabilities of digital holographic microscopy for metrology applications. DHM therefore provides a promising route toward the next generation

of overlay sensors. In a few years df-DHM might become a metrology tool for demanding application in the semiconductor industry.

Bibliography

[1] J. Hesse, M. Stoecklin, M. F. Bulut, B. L. Sabath, and Mariusz, *Changing the way the world works: IBM Research's "5 in 5"* (2021). 13

[2] G. E. Moore, *Cramming more components onto integrated circuits, Reprinted from Electronics, volume 38, number 8, April 19, 1965, pp. 114 ff.*, IEEE solid-state circuits society newsletter **11**(3):33–35 (2006). 13, 34, 53, 87, 112

[3] A. J. den Boef, *Optical wafer metrology sensors for process-robust CD and overlay control in semiconductor device manufacturing*, Surface Topography: Metrology and Properties **4**(2):023001 (2016). 14, 35, 54, 76, 88, 112

[4] A. Aboagye, *Chip shortage: How the semiconductor industry is dealing with this worldwide problem* (2022). 14

[5] G. May, *Fundamentals of Semiconductor Manufacturing and Process Control* (2006). 14, 34

[6] J. Mulkens, B. Slachter, M. Kubis, W. Tel, P. Hinnen, M. Maslow, H. Dillen, E. Ma, K. Chou, X. Liu, W. Ren, X. Hu, F. Wang, and K. Liu, *Holistic approach for overlay and edge placement error to meet the 5nm technology node requirements*, in V. A. Ukraintsev (editor), *Metrology, Inspection, and Process Control for Microlithography XXXII*, vol. 10585, pp. 375 – 388, International Society for Optics and Photonics, SPIE (2018). 15, 34

[7] Y. Blancquaert and C. Dezauzier, *Diffraction based overlay and image based overlay on production flow for advanced technology node*, in A. Starikov and J. P. Cain (editors), *Metrology, Inspection, and Process Control for Microlithography XXVII*, vol. 8681, pp. 712 – 721, International Society for Optics and Photonics, SPIE (2013). 16

[8] J. Xu, L. Qin, Q. Chen, H. Zhi, Y. Wang, Z. Yang, and Z. Mao, *Diffraction-based and image-based overlay evaluation for advanced technology node*, in *2017 China Semiconductor Technology International Conference (CSTIC)*, pp. 1–4 (2017). 16

[9] M. Adel, D. Kandel, V. Levinski, J. Seligson, and A. Kuniavsky, *Diffraction order control in overlay metrology: a review of the roadmap options*, in J. A. Allgair and C. J. Raymond (editors), *Metrology, Inspection, and Process Control for Microlithography XXII*, vol. 6922, pp. 23 – 41, International Society for Optics and Photonics, SPIE (2008). 16, 18, 34, 76, 88

[10] M. Adel, M. Ghinovker, B. Golovanevsky, P. Izikson, E. Kassel, D. Yaffe,

A. M. Bruckstein, R. Goldenberg, Y. Rubner, and M. Rudzsky, *Optimized overlay metrology marks: theory and experiment*, IEEE Transactions on Semiconductor Manufacturing **17**(2):166–179 (2004). 16, 34, 76, 88

[11] C. W. Yeh, C.-T. H. Huang, K. Lin, C. H. Huang, E. Yang, T. H. Yang, K. C. Chen, and C.-Y. Lu, *Overlay target design and evaluation for SADP process*, in A. Starikov (editor), *Metrology, Inspection, and Process Control for Microlithography XXVI*, vol. 8324, pp. 955 – 963, International Society for Optics and Photonics, SPIE (2012). 17

[12] D. M. Gale, M. I. Pether, and J. C. Dainty, *Linnik microscope imaging of integrated circuitstructures*, Appl. Opt. **35**(1):131–148 (1996). 17

[13] M. Adel, J. A. Allgair, D. C. Benoit, M. Ghinovker, E. Kassel, C. Nelson, J. C. Robinson, and G. S. Seligman, *Performance study of new segmented overlay marks for advanced wafer processing*, in D. J. Herr (editor), *Metrology, Inspection, and Process Control for Microlithography XVII*, vol. 5038, pp. 453 – 463, International Society for Optics and Photonics, SPIE (2003). 17

[14] W. Yang, R. Lowe-Webb, S. Rabello, J. Hu, J.-Y. Lin, J. D. Heaton, M. V. Dusa, A. J. den Boef, M. van der Schaar, and A. Hunter, *Novel diffraction-based spectroscopic method for overlay metrology*, in *Metrology, Inspection, and Process Control for Microlithography XVII*, vol. 5038, pp. 200–207, International Society for Optics and Photonics (2003). 18, 34, 54, 88

[15] P. Leray, S. Cheng, D. Kandel, M. Adel, A. Marchelli, I. Vakshtein, M. Vasconi, and B. Salski, *Diffraction based overlay metrology: accuracy and performance on front end stack*, in J. A. Allgair and C. J. Raymond (editors), *Metrology, Inspection, and Process Control for Microlithography XXII*, vol. 6922, pp. 252 – 263, International Society for Optics and Photonics, SPIE (2008). 18, 34, 76

[16] K. Bhattacharyya, A. den Boef, G. Storms, J. van Heijst, M. Noot, K. An, N.-K. Park, S.-R. Jeon, N.-L. Oh, E. McNamara, *et al.*, *A study of swing-curve physics in diffraction-based overlay*, in *Metrology, Inspection, and Process Control for Microlithography XXX*, vol. 9778, p. 97781I, International Society for Optics and Photonics (2016). 20, 36, 54, 76

[17] G. Ben-Dov, I. Tarshish-Shapir, D. Gready, M. Ghinovker, M. Adel, E. Herzel, S. Oh, D. Choi, S. H. Han, M. E. Kodadi, C. Hwang, J. Lee, S. Y. Lee, and K. Lee, *Metrology target design simulations for accurate and robust scatterometry overlay measurements*, in M. I. Sanchez (editor), *Metrology, Inspection, and Process Control for Microlithography XXX*, vol. 9778, pp. 1015 – 1026, International Society for Optics and Photonics, SPIE (2016). 20, 36

[18] S. Mathijssen, M. Noot, M. Bozkurt, N. Javaheri, R. Hajiahmadi, A. Zagaris, K. Chang, B. Gosali, E. Su, C. Wang, A. den Boef, K. Bhattacharyya, G.-T. Huang, K.-H. Chen, and J. Lin, *Color mixing in overlay metrology for greater accuracy and robustness*, in V. A. Ukraintsev and O. Adan (editors), *Metrology, Inspection, and Process Control for Microlithography XXXIII*, vol. 10959, pp. 290 – 297, International Society for Optics and Photonics, SPIE (2019). 21, 36

[19] V. Calado, J. Dépré, C. Massacrier, S. Tarabrin, R. van Haren, F. Dettoni, R. Bouyssou, and C. Dezauzier, *Study of μDBO overlay target size reduction for application broadening*, in V. A. Ukraintsev (editor), *Metrology, Inspection, and Process Control for Microlithography XXXII*, vol. 10585, pp. 1 – 8, International Society for Optics and Photonics, SPIE (2018). 21, 22

[20] H.-J. H. Smilde, M. Jak, A. den Boef, M. van Schijndel, M. Bozkurt, A. Fuchs, M. van der Schaar, S. Meyer, S. Morgan, K. Bhattacharyya, G.-T. Huang, C.-M. Ke, and K.-H. Chen, *Sub-nanometer in-die overlay metrology: measurement and simulation at the edge of finiteness*, in P. H. Lehmann, W. Osten, and A. Albertazzi (editors), *Optical Measurement Systems for Industrial Inspection VIII*, vol. 8788, pp. 468 – 473, International Society for Optics and Photonics, SPIE (2013). 21

[21] W. T. Tel, B. Segers, R. Anunciado, Y. Zhang, P. Wong, T. Hasan, and C. Prentice, *Efficient hybrid metrology for focus, CD, and overlay*, in M. I. Sanchez (editor), *Metrology, Inspection, and Process Control for Microlithography XXXI*, vol. 10145, pp. 707 – 718, International Society for Optics and Photonics, SPIE (2017). 22, 23

[22] J. Du, F. Dai, Y. Bu, and X. Wang, *Calibration method of overlay measurement error caused by asymmetric mark*, Appl. Opt. **57**(33):9814–9821 (2018). 23

[23] J. W. Goodman, *Introduction to Fourier optics, 4th ed.*, chap. 4-6, pp. 75–166, W.H. Freeman and Co., 2017. 23, 29, 30, 43, 91, 110, 114, 116

[24] P. Hariharan, *Optical Holography: Principles, Techniques and Applications*, Cambridge Studies in Modern Optics, Cambridge University Press, 2 edn. (1996). 23

[25] U. Schnars, W. Jüptner, W. Jüptner, and W. Ptner, *Digital Holography: Digital Hologram Recording, Numerical Reconstruction, and Related Techniques*, Springer (2005). 23

[26] M. K. Kim, *Principles and techniques of digital holographic microscopy*, SPIE reviews **1**(1):018005 (2010). 23, 28, 38, 55, 90, 112

[27] W. Osten, A. Faridian, P. Gao, K. Körner, D. Naik, G. Pedrini, A. K. Singh, M. Takeda, and M. Wilke, *Recent advances in digital holography*, Applied optics **53**(27):G44–G63 (2014). 23, 38, 55, 112

[28] B. Javidi, A. Carnicer, A. Anand, G. Barbastathis, W. Chen, P. Ferraro, J. W. Goodman, R. Horisaki, K. Khare, M. Kujawinska, R. A. Leitgeb, P. Marquet, T. Nomura, A. Ozcan, Y. Park, *et al.*, *Roadmap on digital holography (Invited)*, Opt. Express **29**(22):35078–35118 (2021). 23, 27

[29] P. J. de Groot, L. L. Deck, R. Su, and W. Osten, *Contributions of holography to the advancement of interferometric measurements of surface topography*, Light: Advanced Manufacturing **3**(LAM2021090041):1 (2022). 23

[30] D. Gabor, *A New Microscopic Principle*, Nature **161**(4098):777–778 (1948). 23, 26

[31] M. M. Kirkland and Alessia, *Holography's unexpected origins* (2020). 23

[32] W. L. Bragg and G. L. Rogers, *Elimination of the Unwanted Image in*

Diffraction Microscopy, Nature **167**(4240):190–191 (1951). 24

[33] B. M. Hennelly, D. P. Kelly, N. Pandey, and D. S. Monaghan, *Review of Twin Reduction and Twin Removal Techniques in Holography* (2009). 24

[34] E. N. Leith and J. Upatnieks, *Reconstructed Wavefronts and Communication Theory*, J. Opt. Soc. Am. **52**(10):1123–1130 (1962). 24, 95

[35] A. Lohmann, *Optische Einseitenbandbertragung Angewandt auf das Gabor-Mikroskop*, Optica Acta: International Journal of Optics **3**(2):97–99 (1956). 24

[36] E. N. Leith and J. Upatnieks, *Wavefront Reconstruction with Diffused Illumination and Three-Dimensional Objects∗*, J. Opt. Soc. Am. **54**(11):1295–1301 (1964). 24

[37] L. Mandel, *Color Imagery by Wavefront Reconstruction*, J. Opt. Soc. Am. **55**(12):1697–1698 (1965). 24

[38] K. S. Pennington and L. H. Lin, *MULTICOLOR WAVEFRONT RECONSTRUCTION*, Applied Physics Letters **7**(3):56–57 (1965). 24

[39] J. W. Goodman and R. W. Lawrence, *DIGITAL IMAGE FORMATION FROM ELECTRONICALLY DETECTED HOLOGRAMS*, Applied Physics Letters **11**(3):77–79 (1967). 24

[40] M. N. S. Yaroslavsky, Leonid, *Methods of digital holography*, Consultants Bureau, New York; London (1980). 24

[41] U. Schnars and W. Jüptner, *Direct recording of holograms by a CCD target and numerical reconstruction*, Appl. Opt. **33**(2):179–181 (1994). 24, 55

[42] J. Ashley, M. p. Bernal, G. W. Burr, H. Coufal, H. Guenther, J. A. Hoffnagle, C. M. Jefferson, B. Marcus, R. M. Macfarlane, R. M. Shelby, and G. T. Sincerbox, *Holographic data storage*, IBM Journal of Research and Development (2000). 24

[43] J. Joseph and D. A. Waldman, *Homogenized Fourier transform holographic data storage using phase spatial light modulators and methods for recovery of data from the phase image*, Appl. Opt. **45**(25):6374–6380 (2006). 24

[44] H. J. Tiziani and G. Pedrini, *Digital Double-Pulse Holographic Interferometry for Vibration Analysis*, Shock and Vibration **3**:231793 (1900). 24

[45] G. Pedrini, P. Fröning, H. Fessler, and H. J. Tiziani, *In-line digital holographic interferometry*, Appl. Opt. **37**(26):6262–6269 (1998). 24

[46] T. Baumbach, W. Osten, C. von Kopylow, and W. Jüptner, *Remote metrology by comparative digital holography*, Appl. Opt. **45**(5):925–934 (2006). 24

[47] D. P. Kelly, D. S. Monaghan, N. Pandey, T. Kozacki, A. Michałkiewicz, G. Finke, B. M. Hennelly, and M. Kujawinska, *Digital Holographic Capture and Optoelectronic Reconstruction for 3D Displays*, International Journal of Digital Multimedia Broadcasting **2010**:759323 (2010). 24

[48] A. Ku, M. Dudek, B. Kemper, M. Kujawiska, and A. Vollmer, *Tomographic phase microscopy of living three-dimensional cell cultures*, Journal of Biomedical Optics **19**(4):1 – 8 (2014). 24

[49] T. Colomb, J. Kühn, F. Charrière, C. Depeursinge, P. Marquet, and N. Aspert, *Total aberrations compensation in digital holographic microscopy with a reference conjugated hologram*, Opt. Express **14**(10):4300–4306 (2006). 24, 37, 91

[50] E. Cuche, P. Marquet, and C. Depeursinge, *Simultaneous amplitude-contrast and quantitative phase-contrast microscopy by numerical reconstruction of Fresnel off-axis holograms*, Appl. Opt. **38**(34):6994–7001 (1999). 24, 89

[51] G. Pedrini, F. Zhang, and W. Osten, *Digital holographic microscopy in the deep (193 nm) ultraviolet*, Appl. Opt. **46**(32):7829–7835 (2007). 24

[52] G. Faigel and M. Tegze, *X-ray holography*, Reports on Progress in Physics **62**(3):355–393 (1999). 24

[53] H. Lichte, *Electron holography approaching atomic resolution*, Ultramicroscopy **20**:293–304 (1986). 24

[54] P. Korecki, J. Korecki, and T. Ślęzak, *Atomic Resolution γ-ray Holography Using the Mössbauer Effect*, Phys. Rev. Lett. **79**:3518–3521 (1997). 24

[55] G. Pedrini, S. Schedin, and H. J. Tiziani, *Aberration compensation in digital holographic reconstruction of microscopic objects*, Journal of Modern Optics **48**(6):1035–1041 (2001). `https://www.tandfonline.com/doi/pdf/10.1080/09500340108230973`. 24, 89

[56] A. Stadelmaier and J. H. Massig, *Compensation of lens aberrations in digital holography*, Opt. Lett. **25**(22):1630–1632 (2000). 24, 89, 112

[57] S. D. Nicola, A. Finizio, G. Pierattini, D. Alfieri, S. Grilli, L. Sansone, and P. Ferraro, *Recovering correct phase information in multiwavelength digital holographic microscopy by compensation for chromatic aberrations*, Opt. Lett. **30**(20):2706–2708 (2005). 24, 89

[58] S. D. Nicola, P. Ferraro, A. Finizio, and G. Pierattini, *Wave front reconstruction of Fresnel off-axis holograms with compensation of aberrations by means of phase-shifting digital holography*, Optics and Lasers in Engineering **37**(4):331–340 (2002). Optics in Italy Part I. 24, 89

[59] S. Grilli, P. Ferraro, S. D. Nicola, A. Finizio, G. Pierattini, and R. Meucci, *Whole optical wavefields reconstruction by Digital Holography*, Opt. Express **9**(6):294–302 (2001). 24, 89

[60] S. D. Nicola, P. Ferraro, A. Finizio, and G. Pierattini, *Correct-image reconstruction in the presence of severe anamorphism by means of digital holography*, Opt. Lett. **26**(13):974–976 (2001). 24, 89

[61] S. D. Nicola, A. Finizio, G. Pierattini, P. Ferraro, and D. Alfieri, *Angular spectrum method with correction of anamorphism for numerical reconstruction of digital holograms on tilted planes*, Opt. Express **13**(24):9935–9940 (2005). 24, 89

[62] K. Radigan and M. Slama, *Holographic Inspection of Wafers for Sub-Micron Defect Detection*, Conference Proceedings and Presentations (1991). 24

[63] U. Schnars and W. P. O. Jüptner, *Digital recording and numerical reconstruction of holograms*, Measurement Science and Technology **13**(9):R85–R101 (2002). 24

[64] M. A. Schulze, M. A. Hunt, E. Voelkl, J. D. Hickson, W. R. Usry, R. G. Smith, R. Bryant, and C. E. T. Jr., *Semiconductor wafer defect detection using digital holography*, in K. W. T. Jr. and I. Emami (editors), *Process and Materials Characterization and Diagnostics in IC Manufacturing*, vol.

5041, pp. 183 – 193, International Society for Optics and Photonics, SPIE (2003). 24

[65] C. E. T. Jr., T. M. Bahm, L. R. Baylor, P. R. Bingham, S. W. Burns, M. Chidley, L. Dai, R. J. Delahanty, C. J. Doti, A. El-Khashab, R. L. Fisher, J. M. Gilbert, J. S. G. Jr., G. R. Hanson, J. D. Hickson, *et al.*, *Direct to digital holography for semiconductor wafer defect detection and review*, in A. Starikov, K. W. T. Jr., and A. Starikov (editors), *Design, Process Integration, and Characterization for Microelectronics*, vol. 4692, pp. 180 – 194, International Society for Optics and Photonics, SPIE (2002). 24

[66] N. Pandey, *Digital hologram recording systems: some performance improvements*, PhD thesis (2011). 24

[67] G. Pedrini, *Handbook of Optical Metrology: Principles and Applications - Chapter 7* (2009). 29

[68] M. Born and E. Wolf, *Principles of Optics: Electromagnetic Theory of Propagation, Interference and Diffraction of Light (7th Edition)*, Cambridge University Press, 7th edn. (1999). 32

[69] N. G. Orji, M. Badaroglu, B. M. Barnes, C. Beitia, B. D. Bunday, U. Celano, R. J. Kline, M. Neisser, Y. Obeng, and A. Vladar, *Metrology for the next generation of semiconductor devices*, Nature electronics **1**(10):532–547 (2018). 34, 54

[70] H.-J. H. Smilde, A. den Boef, M. Kubis, M. Jak, M. van Schijndel, A. Fuchs, M. van der Schaar, S. Meyer, S. Morgan, J. Wu, *et al.*, *Evaluation of a novel ultra small target technology supporting on-product overlay measurements*, in *Metrology, Inspection, and Process Control for Microlithography XXVI*, vol. 8324, p. 83241A, International Society for Optics and Photonics (2012). 36, 54, 76

[71] K. Bhattacharyya, A. den Boef, M. Jak, G. Zhang, M. Maassen, R. Tijssen, O. Adam, A. Fuchs, Y. Zhang, J. Huang, *et al.*, *Holistic approach using accuracy of diffraction-based integrated metrology to improve on-product performance, reduce cycle time, and cost at litho*, in *Metrology, Inspection, and Process Control for Microlithography XXIX*, vol. 9424, p. 94241E, International Society for Optics and Photonics (2015). 36, 54, 76

[72] A. Kudlinski, B. Barviau, A. Leray, C. Spriet, L. Héliot, and A. Mussot, *Control of pulse-to-pulse fluctuations in visible supercontinuum*, Opt. Express **18**(26):27445–27454 (2010). 36

[73] T. Godin, B. Wetzel, T. Sylvestre, L. Larger, A. Kudlinski, A. Mussot, A. B. Salem, M. Zghal, G. Genty, F. Dias, and J. M. Dudley, *Real time noise and wavelength correlations in octave-spanning supercontinuum generation*, Opt. Express **21**(15):18452–18460 (2013). 36

[74] F. Dubois and P. Grosfils, *Dark-field digital holographic microscopy to investigate objects that are nanosized or smaller than the optical resolution*, Optics letters **33**(22):2605–2607 (2008). 37, 55

[75] F. Verpillat, F. Joud, P. Desbiolles, and M. Gross, *Dark-field digital holographic microscopy for 3D-tracking of gold nanoparticles*, Opt. Express **19**(27):26044–26055 (2011). 37, 55

[76] C. Messinis, V. Tenner, J. de Boer, S. Witte, and A. den Boef, *Theoretical and Experimental Demonstration of a State-of- the-Art Dark-Field Holographic Microscope for Advanced Semiconductor Metrology*, in *Imaging and Applied Optics 2019 (COSI, IS, MATH, pcAOP)*, p. CTu4C.4, Optical Society of America (2019). 37

[77] E. N. Leith, J. Upatnieks, and K. A. Haines, *Microscopy by wavefront reconstruction*, JOSA **55**(8):981–986 (1965). 38, 55

[78] C. Messinis, V. T. Tenner, J. F. D. Boer, S. Witte, and A. den Boef, *Impact of coherence length on the field of view in dark-field holographic microscopy for semiconductor metrology: theoretical and experimental comparisons*, Appl. Opt. **59**(11):3498–3507 (2020). 38, 41

[79] R. Dändliker, E. Marom, and F. M. Mottier, *Two-reference-beam holographic interferometry*, J. Opt. Soc. Am. **66**(1):23–30 (1976). 38

[80] G. Pedrini, Y.-L. Zou, and H. J. Tiziani, *Simultaneous quantitative evaluation of in-plane and out-of-planedeformations by use of a multidirectional spatial carrier*, Appl. Opt. **36**(4):786–792 (1997). 38

[81] D. Cohoe, I. Hanczarek, J. K. Wallace, and J. Nadeau, *Multiwavelength digital holographic imaging and phase unwrapping of protozoa using custom Fiji plug-ins*, Frontiers in Physics **7**:94 (2019). 38

[82] T. Tahara and Y. Arai, *Multiwavelength off-axis digital holography with an angle of more than 40 degrees and no beam combiner to generate interference light*, Applied optics **56**(13):F200–F204 (2017). 38

[83] N. Pavillon, C. S. Seelamantula, J. Kühn, M. Unser, and C. Depeursinge, *Suppression of the zero-order term in off-axis digital holography through nonlinear filtering*, Appl. Opt. **48**(34):H186–H195 (2009). 40

[84] D. P. Kelly, B. M. Hennelly, N. Pandey, T. J. Naughton, and W. T. Rhodes, *Resolution limits in practical digital holographic systems*, Optical Engineering **48**(9):095801 (2009). 40

[85] B. Karamata, P. Lambelet, M. Laubscher, R. Salathé, and T. Lasser, *Spatially incoherent illumination as a mechanism for cross-talk suppression in wide-field optical coherence tomography*, Optics letters **29**(7):736–738 (2004). 40

[86] R. N. Graf and A. Wax, *Temporal coherence and time-frequency distributions in spectroscopic optical coherence tomography*, J. Opt. Soc. Am. A **24**(8):2186–2195 (2007). 40

[87] R. W. Chang, *Synthesis of band-limited orthogonal signals for multichannel data transmission*, Bell System Technical Journal **45**(10):1775–1796 (1966). 41

[88] C. Ruilier, *A study of degraded light coupling into single-mode fibers*, in R. D. Reasenberg (editor), *Astronomical Interferometry*, vol. 3350, pp. 319 – 329, International Society for Optics and Photonics, SPIE (1998). 43

[89] J. Ma, F. Zhao, L. Tan, S. Yu, and Q. Han, *Plane wave coupling into single-mode fiber in the presence of random angular jitter*, Appl. Opt. **48**(27):5184–5189 (2009). 43

[90] S. Mathijssen, H. Heijmerikx, F. Farhadzadeh, M. Noot, L. van der Sneppen, L. Shen, F. Jia, J. Xu, H. Qin, A. den Boef, E. M. Namara, K. Bhat-

tacharyya, C. Fang, and Y. Feng, *Enhancing the applications space of diffraction based overlay metrology by increasing throughput and target pitch flexibility*, in O. Adan and J. C. Robinson (editors), *Metrology, Inspection, and Process Control for Microlithography XXXIV*, vol. 11325, pp. 473 – 479, International Society for Optics and Photonics, SPIE (2020). 47

[91] G. Ben-Dov, I. Tarshish-Shapir, D. Gready, M. Ghinovker, M. Adel, E. Herzel, S. Oh, D. Choi, S. H. Han, M. E. Kodadi, C. Hwang, J. Lee, S. Y. Lee, and K. Lee, *Metrology target design simulations for accurate and robust scatterometry overlay measurements*, in M. I. Sanchez (editor), *Metrology, Inspection, and Process Control for Microlithography XXX*, vol. 9778, pp. 1015 – 1026, International Society for Optics and Photonics, SPIE (2016). 54

[92] F. Heide, M. Rouf, M. B. Hullin, B. Labitzke, W. Heidrich, and A. Kolb, *High-quality computational imaging through simple lenses*, ACM Transactions on Graphics (TOG) **32**(5):1–14 (2013). 55

[93] R. M. Willett, M. E. Gehm, and D. J. Brady, *Multiscale reconstruction for computational spectral imaging*, in *Computational Imaging V*, vol. 6498, p. 64980L, International Society for Optics and Photonics (2007). 55

[94] K.-J. Oh, H.-G. Choo, and J. Kim, *Analysis on digital holographic data representation and compression*, in *2016 Asia-Pacific Signal and Information Processing Association Annual Summit and Conference (APSIPA)*, pp. 1–4 (2016). 55

[95] D. Hillmann, G. Franke, C. Lührs, P. Koch, and G. Hüttmann, *Efficient holoscopy image reconstruction*, Opt. Express **20**(19):21247–21263 (2012). 55

[96] P. J. de Groot, *Vibration in phase-shifting interferometry*, J. Opt. Soc. Am. A **12**(2):354–365 (1995). 55

[97] P. de Groot, *Derivation of algorithms for phase-shifting interferometry using the concept of a data-sampling window*, Appl. Opt. **34**(22):4723–4730 (1995). 55

[98] P. de Groot and X. C. de Lega, *Signal modeling for low-coherence height-scanning interference microscopy*, Applied optics **43**(25):4821–4830 (2004). 55

[99] N. Verrier, D. Donnarumma, D. Alexandre, G. Tessier, and M. Gross, *Digital holographic microscopy with high numerical aperture: wide z range reconstruction*, in *Imaging and Applied Optics 2016*, p. DTh1I.3, Optical Society of America (2016). 55

[100] E. Cuche, P. Marquet, and C. Depeursinge, *Spatial filtering for zero-order and twin-image elimination in digital off-axis holography*, Applied optics **39**(23):4070–4075 (2000). 55

[101] L. L. Deck, *Model-based phase shifting interferometry*, Appl. Opt. **53**(21):4628–4636 (2014). 55

[102] S. Merlo, V. Annovazzi-Lodi, M. Benedetti, F. Carli, and M. Norgia, *Testing of "Venetian-Blind" silicon microstructures with optical methods* (2006). 58, 68

[103] J. Goodman, *Statistical Optics 2nd Ed.*, Wiley (2015). 63

[104] W. Yang, R. Lowe-Webb, S. Rabello, J. Hu, J.-Y. Lin, J. D. Heaton, M. V. Dusa, A. J. den Boef, M. van der Schaar, and A. Hunter, *Novel diffraction-based spectroscopic method for overlay metrology*, in D. J. Herr (editor), *Metrology, Inspection, and Process Control for Microlithography XVII*, vol. 5038, pp. 200 – 207, International Society for Optics and Photonics, SPIE (2003). 76

[105] M. Matsunobu, T. Nishiyama, M. Inoue, R. Housley, C. Bozdog, J. Lim, B. Watson, J. Reece, S. McCandless, O. Zwier, M. van der Schaar, M. Bozkurt, M. al Arif, E. McNamara, P. Kapel, *et al.*, *Novel diffraction-based overlay metrology utilizing phase-based overlay for improved robustness*, in O. Adan and J. C. Robinson (editors), *Metrology, Inspection, and Process Control for Semiconductor Manufacturing XXXV*, vol. 11611, pp. 512 – 521, International Society for Optics and Photonics, SPIE (2021). 76

[106] C. Messinis, T. T. M. van Schaijk, N. Pandey, A. Koolen, I. Shlesinger, X. Liu, S. Witte, J. F. de Boer, and A. den Boef, *Aberration calibration and correction with nano-scatterers in digital holographic microscopy for semiconductor metrology*, Opt. Express **29**(23):38237–38256 (2021). 77, 78, 114, 116

[107] S. Manda, R. Matsumoto, S. Saito, S. Maruyama, H. Minari, T. Hirano, T. Takachi, N. Fujii, Y. Yamamoto, Y. Zaizen, T. Hirano, and H. Iwamoto, *High-definition Visible-SWIR InGaAs Image Sensor using Cu-Cu Bonding of III-V to Silicon Wafer*, in *2019 IEEE International Electron Devices Meeting (IEDM)*, pp. 16.7.1–16.7.4 (2019). 77

[108] T. Colomb, E. Cuche, F. Charrière, J. Kühn, N. Aspert, F. Montfort, P. Marquet, and C. Depeursinge, *Automatic procedure for aberration compensation in digital holographic microscopy and applications to specimen shape compensation*, Appl. Opt. **45**(5):851–863 (2006). 77

[109] D. T. Pierce and W. E. Spicer, *Electronic Structure of Amorphous Si from Photoemission and Optical Studies*, Phys. Rev. B **5**:3017–3029 (1972). 77

[110] C. Messinis, T. T. M. van Schaijk, N. Pandey, V. T. Tenner, S. Witte, J. F. de Boer, and A. den Boef, *Diffraction-based overlay metrology using angular-multiplexed acquisition of dark-field digital holograms*, Opt. Express **28**(25):37419–37435 (2020). 77, 88, 112

[111] K. Bhattacharyya, M. Noot, H. Chang, S. Liao, K. Chang, B. Gosali, E. Su, C. Wang, A. den Boef, C. Fouquet, G.-T. Huang, K.-H. Chen, K. Cheng, and J. Lin, *Multi-wavelength approach towards on-product overlay accuracy and robustness*, in V. A. Ukraintsev (editor), *Metrology, Inspection, and Process Control for Microlithography XXXII*, vol. 10585, pp. 326 – 333, International Society for Optics and Photonics, SPIE (2018). 88

[112] J. Kim, J. Lee, C. Hwang, S. Y. Lee, W. Jung, J. Park, K. Bhattacharyya, A. den Boef, S. Mathijssen, M. Noot, F. Farhadzadeh, D. Park, K. Padhye, S.-R. Jeon, S.-B. Yang, *et al.*, *Taking the multi-wavelength DBO to the next level of accuracy and robustness*, in O. Adan and J. C. Robinson (editors), *Metrology, Inspection, and Process Control for Microlithography XXXIV*, vol. 11325, pp. 222 – 227, International Society for Optics and Photonics,

SPIE (2020). 88, 112

[113] D. S. Grey, *A New Series of Microscope Objectives: II. Preliminary Investigation of Catadioptric Schwarzschild Systems∗*, J. Opt. Soc. Am. **39**(9):723–728 (1949). 88

[114] F. Charrière, A. Marian, T. stan Colomb, P. Marquet, and C. Depeursinge, *Amplitude point-spread function measurement of high-NA microscope objectives by digital holographic microscopy*, Opt. Lett. **32**(16):2456–2458 (2007). 90, 124

[115] T. Colomb, *Numerical aberrations compensation and polarization imaging in digital holographic microscopy*, chap. 3, pp. 59–72, EPFL, Lausanne (2006). 90

[116] A. Doblas, C. Buitrago-Duque, A. Robinson, and J. Garcia-Sucerquia, *Phase-shifting digital holographic microscopy with an iterative blind reconstruction algorithm*, Appl. Opt. **58**(34):G311–G317 (2019). 91

[117] R. W. Gray, C. Dunn, K. P. Thompson, and J. P. Rolland, *An analytic expression for the field dependence of Zernike polynomials in rotationally symmetric optical systems*, Opt. Express **20**(15):16436–16449 (2012). 93, 96

[118] J. Ruoff and M. Totzeck, *Orientation Zernike polynomials: a useful way to describe the polarization effects of optical imaging systems*, Journal of Micro/Nanolithography, MEMS, and MOEMS **8**(3):1 – 22 (2009). 96

[119] J. Sasin, *Introduction to Aberrations in Optical Imaging Systems*, Cambridge University (2012). 96, 104

[120] V. N. Mahajan, *Aberration Theory Made Simple, Second Edition*, SPIE Press (2011). 96

[121] *Optics and optical instruments Preparation of drawings for optical elements and systems Part 5: Surface form tolerances.*, ISO 101105:1996(E), ICS (1996). 96

[122] T. Tahara, X. Quan, R. Otani, Y. Takaki, and O. Matoba, *Digital holography and its multidimensional imaging applications: a review*, Microscopy **67**(2):55–67 (2018). `https://academic.oup.com/jmicro/article-pdf/67/2/55/25108436/dfy007.pdf`. 112

[123] M. A. Schulze, M. A. Hunt, E. Voelkl, J. D. Hickson, W. R. Usry, R. G. Smith, R. Bryant, and C. E. Thomas, *Semiconductor wafer defect detection using digital holography*, in *SPIE Advanced Lithography* (2003). 112

[124] Y. Liu, Z. Wang, and J. Huang, *Recent Progress on Aberration Compensation and Coherent Noise Suppression in Digital Holography*, Applied Sciences **8**(3) (2018). 112

[125] T. T. M. van Schaijk, C. Messinis, N. Pandey, A. Koolen, S. Witte, J. F. de Boer, and A. den Boef, *Diffraction-based overlay metrology from visible to infrared wavelengths using a single sensor*, Journal of Micro/Nanopatterning, Materials, and Metrology **21**(1):1 – 10 (2022). 112, 114

[126] J. Garcia-Sucerquia, *Noise reduction in digital lensless holographic microscopy by engineering the light from a light-emitting diode*, Appl. Opt. **52**(1):A232–A239 (2013). 114

[127] F. Dubois, L. Joannes, and J.-C. Legros, *Improved three-dimensional imaging with a digital holography microscope with a source of partial spatial coherence*, Appl. Opt. **38**(34):7085–7094 (1999). 114

[128] J. Dohet-Eraly, C. Yourassowsky, A. E. Mallahi, and F. Dubois, *Quantitative assessment of noise reduction with partial spatial coherence illumination in digital holographic microscopy*, Opt. Lett. **41**(1):111–114 (2016). 114

[129] F. Pan, W. Xiao, S. Liu, F. Wang, L. Rong, and R. Li, *Coherent noise reduction in digital holographic phase contrast microscopy by slightly shifting object*, Opt. Express **19**(5):3862–3869 (2011). 114

[130] Y. Wang, P. Meng, D. Wang, L. Rong, and S. Panezai, *Speckle noise suppression in digital holography by angular diversity with phase-only spatial light modulator*, Opt. Express **21**(17):19568–19578 (2013). 114

[131] S. Shin, K. Kim, K. Lee, S. Lee, and Y. Park, *Effects of spatiotemporal coherence on interferometric microscopy*, Opt. Express **25**(7):8085–8097 (2017). 114

[132] A. Sharma, G. Sheoran, Z. Jaffery, and Moinuddin, *Improvement of signal-to-noise ratio in digital holography using wavelet transform*, Optics and Lasers in Engineering **46**(1):42–47 (2008). 114

[133] V. Bianco, M. Paturzo, P. Memmolo, A. Finizio, P. Ferraro, and B. Javidi, *Random resampling masks: a non-Bayesian one-shot strategy for noise reduction in digital holography*, Opt. Lett. **38**(5):619–621 (2013). 114

[134] M. Haouat, J. Garcia-Sucerquia, A. Kellou, and P. Picart, *Reduction of speckle noise in holographic images using spatial jittering in numerical reconstructions*, Opt. Lett. **42**(6):1047–1050 (2017). 114

[135] F. Pan, L. Yang, and W. Xiao, *Coherent noise reduction in digital holographic microscopy by averaging multiple holograms recorded with a multimode laser*, Opt. Express **25**(18):21815–21825 (2017). 114

[136] X. Zhao, H. Zhang, Y. Zhou, W. Bian, T. Zhang, and X. Zou, *Gibbs-Ringing Artifact Suppression with Knowledge Transfer from Natural Images to MR Images*, Multimedia Tools Appl. **79**(4546):3371133733 (2020). 115

[137] E. Cuche, P. Marquet, and C. Depeursinge, *Aperture apodization using cubic spline interpolation: application in digital holographic microscopy*, Optics Communications **182**(1-3):59–69 (2000). 117

[138] J. T. Y. C. H. Seo, *Sidelobe suppression in ultrasound imaging using dual apodization with cross-correlation.*, IEEE transactions on ultrasonics, ferroelectrics, and frequency control **55**(10):2198–2210 (2008). 117

[139] F. Harris, *On the use of windows for harmonic analysis with the discrete Fourier transform*, Proceedings of the IEEE **66**(1):51–83 (1978). 117

[140] C. Buitrago-Duque and J. Garcia-Sucerquia, *Physical pupil manipulation for speckle reduction in digital holographic microscopy*, Heliyon **7**(1):e06098 (2021). 118

[141] D. Hincapie, J. Herrera-Ramírez, and J. Garcia-Sucerquia, *Single-shot speckle reduction in numerical reconstruction of digitally recorded holograms*, Opt. Lett. **40**(8):1623–1626 (2015). 118

[142] N. A. Mohammed, T. A. Ali, and M. H. Aly, *Performance optimization*

of apodized FBG-based temperature sensors in single and quasi-distributed DWDM systems with new and different apodization profiles, AIP Advances **3**(12):122125 (2013). 118

Nederlandse samenvatting

Dit proefschrift onderzoekt de toepassing van donkerveld (dark-field) digitale holografische microscopie (df-DHM) voor geavanceerde halfgeleider overlay metrologie. Theoretische analyse en experimenteel onderzoek werden uitgevoerd om dit potentieel te valideren en te kwantificeren in welke mate df-DHM kan worden beschouwd als een veelbelovende techniek voor toekomstige overlay metrologie. Halfgeleidermetrologie is zeer uitdagend en moet voortdurend innoveren om tegemoet te komen aan de uitdagende eisen van de halfgeleiderindustrie. Hieronder volgt een samenvatting van elk hoofdstuk:

Ch. 2 In dit hoofdstuk worden de details van ons df-DHM concept beschreven. We laten zien dat angulaire frequentiemultiplexing ons in staat stelt om twee off-axis hologrammen van de zogenaamde $+1^{st}$ orde en -1^{st} orde beelden in parallel te verwerven. Deze aanpak stelt ons in staat om de volledige NA van de imaging lens te gebruiken en de parallelle acquisitie zorgt ook voor ongevoeligheid voor intensiteit ruis van de lichtbron. In ons df-DHM concept hebben we specifieke ontwerpkeuzes gemaakt die resulteren in aanzienlijke toepassingsvoordelen, maar die ook specifieke uitdagingen creëren die we nader hebben onderzocht. In ons concept is de lichtbron bijvoorbeeld via een single-mode glasvezel gekoppeld aan de optiek van de microscoop. Dit resulteert in een zeer compacte sensorkop die hogesnelheidsmetrologie mogelijk maakt door meerdere df-DHM sensorkoppen parallel te zetten. Tijdens de eerste proof-of-concept overlay-metingen hebben we echter ontdekt dat de reproduceerbaarheid van onze overlay-metingen aanzienlijk werd aangetast door instabiliteiten in de effeciency van de inkoppeling in de single-mode glasvezel. Dit is iets dat kan worden opgelost met een stabieler opto-mechanisch ontwerp.

Ch. 3 Dit hoofdstuk presenteert een theoretisch model van de invloed van de coherentielengte op de afmetingen van het objectveld (FoV) in een donkerveld (dark-field) digitale holografische microscoop. Dit model toont aan dat de FoV omgekeerd evenredig is met de bandbreedte van de lichtbron. Het gepresenteerde model kan worden gebruikt om eisen te stellen aan de ontwerpparameters die ervoor zorgen dat de opstelling voldoende FoV biedt voor metrologie. Er werd een testopstelling gepresenteerd om de holografische reconstructiemogelijkheden te demonstreren voor zowel faseverschuivende

als off-axis metingen, waarbij off-axis het voordeel biedt van een holografische reconstructie op basis van een acquisitie.

Ch. 4 Dit hoofdstuk demonstreert het succesvolle gebruik van ons df-DHM concept voor het meten van overlay over een uitgebreid golflengtebereik. Tot nu toe waren overlay-metingen beperkt tot zichtbare golflengten, maar het gebruik van materialen die ondoorzichtig zijn voor zichtbare golflengten maakt metingen met infrarood licht noodzakelijk. Wij hebben een breadboard-testopstelling gebouwd die in staat is overlay-metingen uit te voeren bij golflengten van 400 tot 1600 nm. Met deze opstelling hebben wij een goede correlatie aangetoond tussen de geprogrammeerde hoeveelheid overlay en de gemeten hoeveelheid overlay. Deze metingen tonen de haalbaarheid aan van ons df-DHM concept voor overlay metrologie over een groot golflengte gebied met een enkele sensor van halfgeleidermetrologie voor dit uitgebreide golflengtegebied met een enkele sensor. Bovendien toonden we aan dat coherentie-gating een zeer effectieve onderdrukking bood van ongewenst licht dat de sensor bereikte. Dit toont mooi de levensvatbaarheid aan van een overlaysensor die gevoelig is voor zichtbaar en infrarood licht, waardoor meer vrijheid ontstaat in de keuze van materialen voor gentegreerde schakelingen.

Ch. 5 In dit hoofdstuk wordt een methode gepresenteerd voor de kalibratie en correctie van lens aberraties met behulp van puntverstrooiers op een siliciumsubstraat. Deze puntverstrooiers hebben een diameter van ongeveer 80 nanometer. Computationele beeldvormingstechnieken worden gebruikt om de fout in het golffront te bepalen en we gebruiken deze om te corrigeren voor de lensafwijkingen, uitgaande van isoplanatische beeldvormingscondities. Uit de metingen blijkt dat puntverstrooiers zeer geschikt zijn voor het kalibreren van zelfs grote golffrontaberraties in Digitale Holografische Microscopie. Hoewel onze opstelling nog onvolkomen heden bevatte zoals een longitudinale positionerings fout van de referentie glasvezel, zijn we in staat geweest om overtuigende gegevens van de aberratie correctie mogelijkheden van onze techniek te tonen. Ongecorrigeerde beelden van metrologiedoelen op een testwafer zagen er ernstig vervormd uit, maar de beeldkwaliteit verbeterde drastisch na toepassing van een aberratiecorrectie. Verwacht wordt dat deze kalibratiemethode goed zal presteren over een breed golflengtebereik, zodat een lenskalibratie methode voor het gehele golflengtebereik beschikbaar is. Tenslotte worden een aantal potentiele kalibratiefoutbronnen gepresenteerd om de prestaties van de gepresenteerde methode te evalueren en inzicht te geven in de diffractie-begrensde afbeeldingen die met een eenvoudige lens kunnen worden bereikt.

Ch. 6 Het laatste hoofdstuk van dit proefschrift presenteert computationele algoritmen om effecten te verzachten die inherent zijn aan het gebruik van coherente verlichting. Het uiteindelijke doel is om de overlay metrologie mogelijkheden van de df-DHM te onderzoeken wanneer de meetobjecten omgeven zijn door andere structuren. In dit geval zal de brede point-

spread-functie (PSF) in aanwezigheid van aberraties leiden tot ernstige optische overspraak van de omringende structuren naar het meetobject en de metrologieprestaties verminderen. De uitstekende aberratiecorrectiemogelijkheden die wij hebben aangetoond, zullen naar verwachting deze optische overspraakfout aanzienlijk verminderen, maar nog niet op het vereiste niveau. Optische overspraak kan verder worden verminderd door extra digitale apodisatie die de zijlobben van de impulse response onderdrukken. Met de toevoeging van apodisatie op de gemeten PSF's kunnen we de coherente ruis aanzienlijk verminderen en betere metrologieprestaties bereiken. Tijdens dit onderzoek bleek uit een afwijking tussen simulaties en experimenten dat lichtverstrooiing door lensimperfecties (b.v. oppervlakteruwheid) de effectiviteit van apodisatie beperkte.

Acknowledgments

The adventurous and occasionally arduous journey to obtain my PhD has come to an end. It has been an interesting experience that combined a lot of effort and hard work with fulfilling and rewarding emotions. This journey helped me grow not only professionally as a scientist but as a person too. Looking back to the past 4 years i obtained many skills which were needed to overcome numerous challenges that a PhD research project holds. I am indebted to many people who knowingly or unknowingly helped and contributed to the completion of this thesis and i feel the need to dedicate a few words as an attempt to show my appreciation and respect. The rich and deep emotions that i feel cannot be addressed in a few lines but as always i will do my best to describe them in my way.

First of all, I would like to thank my life partner, my wife Zoi, for standing by me all this time and giving me strength to continue and pursue my goals. Without whom i wouldn't have made it till the end of the line. Zoi made me a better man and the best version of my self and i will always be inspired of her wisdom and kindness.

Of course i would like to thank and offer my gratitude to my supervisor, Arie den Boef, for his excellent guidance in carrying out this demanding research project. You gave me the chance to work with you and learn from you, and i consider my self one of the luckiest PhD researcher that had the honor to have you as a mentor. Your experience in the field and your ability to deliver the information in a clear and simplistic way was priceless. Your guidance and the way you work were inspiring in so many levels.

Starting on the personal level, you have always treated me as a colleague and equally important member of the team. From a senior Fellow of ASML, with your career, i was expecting a different more impersonal supervision when i started. In the contrary, you were always finding time to discuss with me about physics, writing, experiments and even about my feeling and my well-being. You have been a very supportive supervisor and i really appreciate your efforts in making me more confident and believing in myself and my work. I am also very thankful to you for showing me how to present my work in a clear way so that everyone can understand, by guiding the audience through the presentation. Regarding research i can spend hours highlighting a few of the hundreds of ideas that you had every time we were brainstorming. I will consider it a win if at the end of my working life i will have a quarter of your knowledge and ideas.

I also take this opportunity to thank the two colleagues, with whom i worked

the most the last 4 years. Vasco (Vasco Tenner) & Perry (T.T.M. van Schaijk) former postdoc researchers in the Computational Imaging group and currently ASML's employees, for the guidance and knowledge that you so gratefully shared with me. But most importantly for the bonding and friendship that you offered and your patience on my ignorance or my stubbornness.

Vasco, thank you for setting up the foundations of this project and for being the best supervisor i could ask for. The "answering a question with a question" approach was really a valuable lesson for me that i will hold for all my career. Perry, we worked together for almost 2 years of my PhD and i learned a lot by your side. I will always hold and reminisce our shared times in the lab and our way of meet during COVID times. Our discussions and our great foosball matches were really a good distraction from the heavy load of work during society's lockdown.

The last months of my PhD, i had the pleasure to meet the new members of the Computational Imaging group, Manashee (dr. M. Adhikary) and Tamar (T. Cromwijk). Manashee, thank you for the fun "nerd" talks that we had, or to set it accurately, for your patience on listening to my passionate monologues. Your contribution to this thesis is undoubtful and i learned a lot from you even in a short period of time. I consider you as a friend that gave me strength and reassurance during the writing process of my PhD. Tamar, it brings me joy to know that i passed the torch to someone that shares the same passion and i am sure that you will carry on the DHM work and set the highest standards. I have high expectations and i am sure that you will deliver. Thank you for your contribution to this thesis and the good times we shared. I am sure that i will meet again with both of you in the near future, perhaps as colleagues once more.

For their major contributions, i would be ignorant if i didn't thank Nitesh (Nitesh Pandey) and Armand (Armand Koolen) from ASML for teaching me all i know about phase retrieval and lens aberrations, respectively. All the inspiring discussions and data analyses that we had together helped me understand the concepts and the challenges in the best possible way.

A similar inspiration and "knowledge transfer"was offered to me generously by my co-promotors, Johannes (J. F. de Boer) and Stefan (S. Witte), who were always there for me, monitoring my progress and helping me all this period.

Special thanks to Ilan (dr. I. Shlesinger) and Kevin (K. Liu) for their contribution in the preparation of the PSF samples, which resulted in two research papers that were presented in Chapter 5 and 6.

The second half of my PhD, i had also the chance to interact with everyone from the Nanoscale Imaging and Metrology Group of dr. Lyuba Amitonova. I need to acknowledge and mention that i gained a lot from my discussions with each and everyone from the group.

At this point, i would like to thank a few people for the technical support that they provided all these years. Marco (M. Konijnenburg), you are one of the main reasons that this project was and still is a success story. Not only the high-level software support but your support in general with your positive attitude and your willingness to help me whenever i needed you. The same willingness and efficiency i saw on another valuable member of the Computational Imaging group, Bartjan (B. Spaanderman). Bartjan, thanks for making the lab the way

it is, i will miss your faster than “shazam”song identification.

Of course the technical support was never missed for this project. By order of appearance, special thanks to all the technicians: Rob (R. Kortekaas), Laurens (L. van Buurens), Nik (N. Noest), Arend-Jan (van Calcar), Reinout (R. Jaarsma), Mark (M. Mol), Thomas (T. Meijvogel). As well as AMOLF staff: Bob Drent, Dimitry Lamers, Igor Hoogsteder, Jan van der Linden, Remco Kempe, Dylan Loozen.

Same goes to the support that i had from the management team, Joost (prof. dr. J. Frenken) and Marjan (dr. M. Fretz) and the ARCNL/AMOLF support staff. Thank you, Marjan, Rosa, Cathelijne, Romy, Oana.

There are so many people that i want to express my gratitude for their support and interest. Special thanks to Wim (prof. dr. W.M.G. Ubachs), Kjeld (prof. dr. K.S.E. Eikema) and Hugo (dr. H. Cramer). The list will be extremely long if i include all the ARCNLers and also VU people for giving me the courage to go on. To name a few, thank you Kevin, Lucas, Thomas, Zeudi, Wei, Ben, Zhouping, John, Jan, Alessandro T. and A., Lars L. and S., Yahia, Ksenia, Stephen, Neha, Maisie, Anne, Ruben, Sylviane, Alexandra and Antonis.

For last but definitely not least, for their support and for all the good and bad times we shared, i would like to express my gratitude to my family and to my closest friends. My father and role model, Giorgos, mother, Catherina, sister, Maria and grandfather, Christos. My parents in law, Dimitra and Konstantinos, my beloved niece and nephew, Dimitra and Giannis and my wife’s sisters Popi and Sia. My dearest friends, Nikolas and Alexandros, but also Robin, Thanasis, John, Lena, Giorgos, Reinier and Emy. And some final additions for all the hours-days that we spent together, Jack, Kyle, Chris, Vasilis and more.

I will hold the bittersweet memories of my PhD life forever, and I thank all my colleagues, friends, and family, whether mentioned or not, for their support, contributions, and the times we shared. At the end of this thesis, I take this opportunity to offer my sincere gratitude to all the people who have helped me make this journey possible, and i would like to close this chapter of my life with a hindsight...

-Christos